2011

solid-state NMR studies of the structure and dynamics of the influenza AM2 transmembrane domain in lipid bilayers

Fanghao Hu
Iowa State University

Solid-state NMR studies of the structure and dynamics of the influenza AM2 transmembrane domain in lipid bilayers

by

Fanghao Hu

A thesis submitted to the graduate faculty

in partial fulfillment of the requirements for the degree of

MASTER OF SCIENCE

Major: Chemistry

Program of Study Committee:
Mei Hong, Major Professor
Klaus Schmidt-Rohr
Edward Yu

Iowa State University

Ames, Iowa

2011

Table of Contents

Acknowledgements

I am truly grateful to all people who have helped and guided me in the last three years. It is them who make my life here so memorable. I would like to especially thank my major advisor Dr. Mei Hong for her support during my study here. She is an excellent researcher who teaches me the knowledge of NMR and encourages the exciting scientific discussion between us. The experience I have here will always be valuable in my life.

I would also like to thank Dr. Klaus Schmidt-Rohr for his inspiring lectures and stimulating discussion during our group meetings. Thank you to Dr. Edward Yu for being my committee member and offering many suggestions. And I would like to thank my colleagues, who create such a nice working environment: Dr. Timothy Doherty, Yuan Zhang, Marilu Perez, Theint Theint, Dr. Evgenii Levin, Dr. Xueqian Kong, Dr. Yanyan Hu, Dr. Aditya Rawal, Dr. Bosiljka Njegic, Tuo Wang, Aaron Liao, Lina Xie, Jinfang Cui and Robert Johnson. Especially, I thank Dr. Wenbin Luo who helped me with NMR at the beginning of my study, Dr. Sarah Cady for her selflessness in sharing her experiment experience, Dr. Shenhui Li and Yongchao Su for so many interesting conversations we have. I am also thankful to many people in the Department of Chemistry of Iowa State University, Dr. Theresa Windus and Dr. Shu Xu for their advice and kindness, Lynette, Mary, Carlene and Renee for their assistance. Their help are greatly appreciated.

I would like to express thanks to my friends here in USA too: Jiawei Chen, Yiqi Huang, Fan Ye, Peng Xu, Xin Liu, Songchen Xu, Dr. Dapeng Jing, Tianfu Wang, Kapil Kandel, Yan Gu, Dahai Shao, Weiwei Xie, and Chen Liu. Without them, my life wouldn't have so much fun.

Last but not least, I thank my beloved parents for their unconditional care and support, who always encourage me to follow my dream. To them I sincerely dedicate this thesis.

Abstract

For heterogeneous and insoluble systems that are difficult for X-ray diffraction and solution NMR to characterize, solid-state NMR presents a powerful technique for native-state studies. Membrane protein, associated with the membrane environment, represents a system with special advantages for solid-state NMR. In this thesis, we have applied various solid-state NMR techniques to study the structure and dynamics of the transmembrane domain (TM) of M2 protein of influenza A Udorn strain in lipid bilayers.

The M2 protein of influenza A virus (AM2) forms a tetrameric proton channel on the virus membrane and plays an important role in the influenza virus life cycle. The elucidation of its functional mechanism may have a great impact on the public health. By applying $^{13}C\{^{15}N\}$ REDOR and DIPSHIFT experiments, we have determined the conformations and dynamics of a key His37 residue of the AM2 TM channel in both closed and conducting states and a proton gating and conduction mechanism has been proposed. Furthermore, the conformational plasticity of the AM2 TM backbone in lipid bilayers has been studied under various external conditions with 2D homonuclear (DARR) and heteronuclear (HETCOR) correlation experiments. Three sets of chemicals-shift-derived backbone conformations were identified that may be important for the channel function. Finally, to investigate the His37-activation process of the AM2 channel, we extracted four pKa values of the His37 tetrad by quantifying the side chain ^{15}N intensity changes with pH in the ^{1}H-^{15}N CP experiments and gained information on the pH-dependent distribution and the relative conductivity of each charged state by correlating with electrophysiological results.

Chapter 1
Introduction

1.1 Influenza AM2 Protein Structure and Function

1.1.1 Proton Conductivity, and Ion Selectivity of the AM2 Channel

The M2 protein of influenza A virus has received much attention in recent years due to the drastically increased drug resistance. It has been found that influenza AM2 protein plays key roles in both the early and late stages of the virus life cycle. The AM2 protein with 96 residues comprises three domains: a short N-terminal extracellular domain (residue 1-21), a single transmembrane (TM) domain (22-46) and a long C-terminal intracellular tail (47-96). It forms a tetrameric pH-activated proton-selective channel in the virus envelope. Activated around pH 6.0, the AM2 channel transports protons inward to acidify the virus interior, which leads to the uncoating of the viral matrix protein, the membrane fusion of the virus and endosome and the release of the viral RNA into the host cell for replication (*1*). Further study has shown that the AM2 TM domain alone can retain at least 50% of the channel activity of the whole protein, which represents the functional core of the AM2 channel (*2*).

Extensive electrophysiological studies both in vivo and in vitro have reported the proton conductivity of the AM2 protein. In *Xenepus laevis* oocyte and liposome measurements, the single-channel conductance of AM2 at mildly acidic pH 6.5-5.5 has been estimated to be in the range of aS to fS (*3-5*), corresponding to low transport rates of 10-10,000 protons per second. The ion selectivity of the AM2 channel has also been studied. The affinity of the AM2 channel for proton is higher than that for Na^+ and K^+ by a factor of 1.5-3.0 x 10^6 (*5-7*).

1.1.2 Drug Inhibition of the AM2 Channel

The AM2 channel can be nearly irreversibly inhibited by the antiviral drug amantadine. 100 μM amantadine can reduce over 90% of the proton conductivity for the Udorn strain of AM2 protein (*8*). The Hill coefficient for amantadine inhibition is measured to be ~1, suggesting a 1:1 drug to channel binding ratio (*8*). Many naturally-occurring drug-

resistant mutants have been isolated to have mutations N-terminal to Gly34, including the most commonly-found S31N mutation (*9*), which results in an over 10-fold reduction in the amantadine sensitivity, while mutations C-terminal to Gly34 have little effect on the amantadine resistance (*10*). These observations all suggest that the amantadine-binding region is located at the N-terminal half of the channel (*10*).

To directly resolve the drug-binding site, several high-resolution structures of the AM2 channel in complex with amantadine or rimantandine have been solved in the last three years. A crystal structure of the AM2 TM domain (22-46) at pH 5.3 found electron density in the N-terminal half of the channel between Val27 and Gly34, indicating the amantadine-binding region (*11*). However, a solution NMR structure of a longer construct of AM2 (18-60) at pH 7.5 observed weak nuclear Overhauser enhancements (NOEs) between drug and protein at the lipid-facing pocket, proposing four rimantadine binding to the interfacial region of the AM2 protein (*12*), which is incompatible with the finding from X-ray diffraction. This controversy has been successfully reconciled by a solid-state NMR study of the AM2 channel (22-46) in DMPC bilayers at pH 7.5 by our group (*13*). Quantitative amantadine-peptide backbone distances were measured to provide definite constraints for the drug location (*13*). A high-affinity site was found at the N-terminal of channel lumen near Ser31, while at high drug concentration, a secondary low-affinity site appeared at the C-terminal lipid-facing region similar to what was proposed from the solution NMR study (*13*). ^{2}H NMR of deuterated amantadine in the channel further revealed the different drug orientations and dynamics at the two distinct binding sites (*13*). A later surface plasmon resonance (SPR) study conducted under similar sample condition supported the dual-binding results and quantified a three order of magnitude affinity difference between the two binding sites (*14*).

1.1.3. AM2 Channel Proton Conduction Mechanisms

His37 is the only ionizable residue and one of the most conserved residues in the AM2 TM domain. Many His37 mutations have been shown to be toxic to viruses and remove the pH-dependent activity, ion selectivity and amantadine sensitivity (*15, 16*). Furthermore, H37A and H37F mutants were found to be less stable than wild type M2 protein by 2-3 kcal/mol from analytical ultracentrifugation experiments (*17*). Thus, it was suggested that a

single His37 residue was responsible for the pH-sensing and proton selectivity of the AM2 channel (*15*), and contributed to the association stability of the AM2 tetramer (*17*).

Two models of how protons pass through the His37 tetrad have been proposed. In the first "gating" model, the successive protonations of His37 residues at low pH open the pore at this site due to electrostatic repulsions, and a continuous water wire is formed (*18*), on which protons can hop by the Grotthuss mechanism. From MD calculations, a 60˚ χ_2 change of His37 was suggested to be sufficient to open the channel for continuous water wire formation (*19*) and an excess proton was captured in the simulation to form a Zundel complex with two water molecules from two sides of the His37 tetrad (*20*). In the second "shuttle" model, His37 directly participates in the proton transfer. The exterior-facing imidazole nitrogen of His37 first accepts a proton to become biprotonated, and then the interior-facing nitrogen releases its proton and becomes deprotonated (*21*). It was proposed that the original state may be recovered by tautomerization or the imidazole ring flips (*21*). The low proton conductance and low-pH saturation of the AM2 channel can be explained with this model, where the His37 sidechain motion, tautomerization or (de)protonation would be the limiting step.

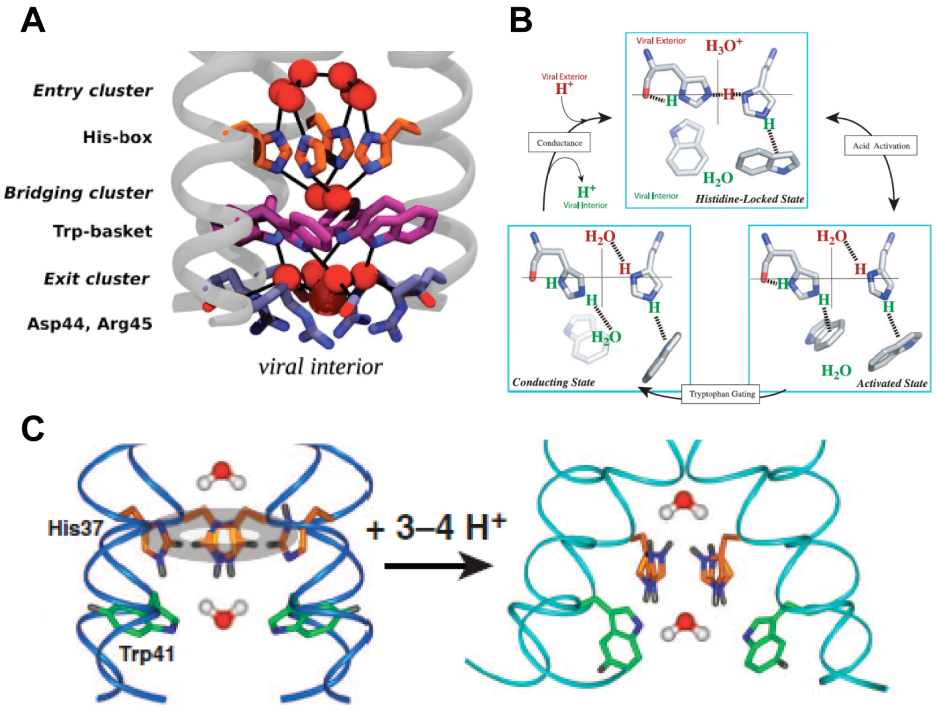

Figure 1.1. Three proton conduction models.

Three recent studies of the AM2 channel from X-ray crystallography, solid-state NMR, and MD simulations have proposed mechanisms with direct His37 participation in the proton conduction, which agrees with the shuttle model. However, how His37 mediates proton transport in detail is different. A 1.65 Å-resolution crystal structure of AM2 TM (22-46) at pH 6.5 observed a His-box conformation surrounded by layers of water clusters. Based on this structure, it was suggested that the proton diffusing through the channel may be delocalized between four His37 and associated water molecules (*22*) (Figure 1.1A). A second study of His37 structure and interaction with Trp41 by MD simulations proposed a low-barrier hydrogen bond between adjacent His37 imidazole and imidazolium, which locked the channel in the doubly charged state (*23*). The third protonation broke the hydrogen-bonded dimer and established a cation-π interaction between His37 and Trp41. Subsequent Trp41 conformational rearrangement may expose His37 to C-terminal water for proton transfer into the virion (Figure 1.1B) (*23*). In the third study by our group, the protonation states, tautomeric structures, rotameric conformations and dynamics of His37 have been extensively studied at pH 8.5 and pH 4.5 in a virus-envelope-mimetic membrane using solid-state NMR (*24*). The results indicated that at pH 8.5 CH-π interactions between His37 restricted the channel and at pH 4.5 His37 rings experienced microsecond reorientations, facilitating imidazole protonation and deprotonation for continuous proton conduction (*24*) (Figure 1.1C).

1.1.4 His37 Protonation and Trp41 Gate

In addition to the conduction mechanism of the open channel, how the AM2 channel is activated from the closed state upon His37 protonation is crucial. Four acid dissociation constants (pKa) of His37 tetrad were first estimated to be 8.2, 8.2, 6.3 and <5, based on His37 sidechain ^{15}N intensity analysis of AM2 TM (22-46) in DMPC/DMPG bilayers using solid-state NMR (*25*). Based on these values, the protonation process of the His37 tetrad was suggested that the AM2 channel easily accepted two protons around pH 8.2 to be doubly charged and at pH 6.3 the +3 charged state became populated, which may correlate with channel activation (*25*). The effect of amantadine binding was also studied, which was found

to significantly inhibit His37 protonation, resulting in a lowered pKa value by approximately three orders of magnitude (*26*).

Moreover, the AM2 channel can be activated only under external low pH, regardless of the internal pH. Mutagenesis data showed that the AM2 channel with W41A/C/F mutations could conduct outward currents under internal low pH (*27*). And W41A mutant could be inhibited by intracellular Cu^{2+} but not in the wild type M2 channel (*28*). Both results suggested that Trp41 may act as a C-terminal gate to shield His37 from protonation and coordination at the intracellular side (*27, 28*). Therefore, with channel activated at external low pH, Trp41 conformational change may be required for His37 to access C-terminal water for proton transfer. Until now, Trp41 conformations at high pH have been studied with solid-state NMR, solution NMR and MD simulations. Two rotameric structures were suggested, t90 (χ_1=180°, χ_2=90°) (*19, 29*) and t-105 (χ_1=180°, χ_2=-105°) (*12, 30*). In order to obtain the whole picture of the proton conduction in the AM2 channel, it is necessary to understand how the conformation of Trp41 changes in concert with His37 protonation.

1.1.5. The Amphipathic Region of the AM2 Protein

In addition to its proton channel activity, recent studies have found that the AM2 protein may play important roles in virus assembly and budding through its cytoplasmic tail (*31, 32*). A conserved amphipathic region (47-62) within the cytoplasmic tail was found to bind cholesterol (*33*) and to mediate membrane scission and virion budding under specific cholesterol concentration (*34*). The atomic structures of the amphipathic helix have been studied using EPR, solution NMR and solid-state NMR (*12, 23, 35*). Although the helix orientations in all studies were found to be nearly parallel to the membrane surface, their locations and environments were different. Structures solved with EPR in POPC/POPG bilayers (*35*) and solid-state NMR in DOPC/DOPE bilayers (*23*) both showed that the helices lay at the membrane interfacial region, accessible to both lipid and water, while the micelle-solubilized solution NMR structure had the amphipathic helices in the bulk solution forming an inward-facing base without contact with the membrane (*12*). Moreover, EPR results showed that the helices moved away from the center of the channel and became more embedded in the bilayers at pH 5.6, possibly keeping the channel open through stronger

interactions with the membrane (*35*). In contrast, solution NMR data suggested that the C-terminal base remained intact at pH 6.0, so as to maintain the association of the tetramer (*12*). Further research is required to fully understand the structure-function relations of the AM2 amphipathic region.

1.2 NMR Methodology

NMR is a very powerful technique to measure physical properties at the atomic level. Solid-state NMR, combined with magic angle spinning (MAS), allows for high-resolution study of many solids that are inaccessible by other approaches. Retained in the solid state, dipolar interaction is one of the key properties used by solid-state NMR. Two dipolar coupling based experiments, REDOR and DIPSHIFT, are extensively applied to the structure and dynamics studies in this thesis, which will be briefly introduced here.

1.2.1 Dipolar Interaction

Dipolar coupling between nuclear spins can give direct internuclear distance information, which is important in molecular structural determination. For an isolated pair of spin-½ nuclei, the dipolar coupling Hamiltonian in Cartesian coordinates is (*36*):

$$\hat{H}^{D}_{IS} = \hat{\vec{I}} \cdot \hat{\vec{\vec{D}}} \cdot \hat{\vec{S}} \tag{1.1}$$

where $\hat{\vec{I}}$ and $\hat{\vec{S}}$ are the spin operators, and $\hat{\vec{\vec{D}}}$ is the dipolar interaction tensor.

In a high magnetic field B_0, the dipolar Hamiltonian is truncated:

For homonuclear dipolar interaction:

$$\hat{H}^{tr}_{\mathrm{hom}o} = \frac{1}{2} D_{zz}[3\hat{I}_z\hat{S}_z - \hat{\vec{I}} \cdot \hat{\vec{S}}] \tag{1.2}$$

For heteronuclear dipolar interaction:

$$\hat{H}^{tr}_{hetero} = D_{zz}\hat{I}_z\hat{S}_z \tag{1.3}$$

$$D_{zz} = -2\hbar\frac{\mu_0}{4\pi}\frac{\gamma_I\gamma_S}{r_{IS}^3}\cdot\frac{1}{2}(3\cos^2\theta_{IS} - 1) = 2d_{IS}\cdot\frac{1}{2}(3\cos^2\theta_{IS} - 1) = 2\omega^D_{IS} \tag{1.4}$$

where d_{IS} is the dipolar coupling constant (in unit of rad·s^{-1}), which is inversely proportional to the cube of the internuclear distance. θ_{IS} is the relative angle between the internuclear vector and the magnetic field B_0, and ω_{IS}^D is the dipolar coupling frequency.

Under magic angle spinning, θ_{IS} is time dependent and ω_{IS}^D can be written:

$$\omega_{IS}^D(\alpha,\beta,t) = d_{IS} \cdot \frac{1}{2}[\sin^2\beta\cos 2(\alpha+\omega_r t) - \sqrt{2}\sin 2\beta\cos(\alpha+\omega_r t)] \qquad (1.5)$$

where α and β are the azimuthal and polar angle respectively, between the internuclear vector and the rotor axis. ω_r is the MAS frequency.

At the end of each rotor period (T_r), the dipolar coupling frequency ω_{IS}^D is averaged:

$$\overline{\omega_{IS}^D(\alpha,\beta,t)} = \int_0^{T_r} \omega_{IS}^D(\alpha,\beta,t)dt = 0 \qquad (1.6)$$

So there is no dipolar evolution of magnetization after each rotor period under MAS.

1.2.2 Rotational Echo DOuble Resonance (REDOR)

To retrieve the distance information from the dipolar coupling averaged out by MAS, REDOR experiment was developed by Gullion and Schaefer (*37*) to be a very robust technique for recoupling heteronuclear dipolar coupling using rotor synchronized π pulses (Figure 1.2A).

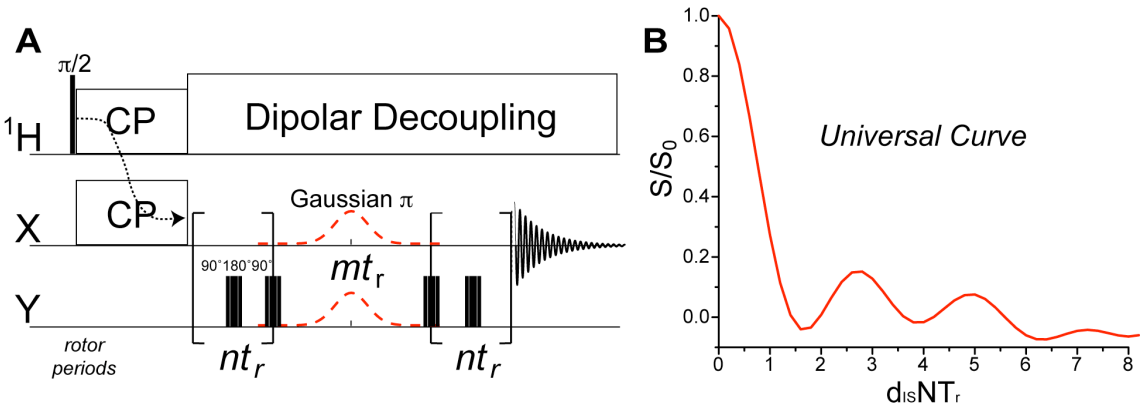

Figure 1.2. The pulse sequence and the universal curve of REDOR experiment.

Multiple π pulses are applied every half rotor period to maximize the averaged dipolar coupling in each rotor period by modulating the sign of the dipolar interaction, so that:

$$\overline{\omega_{IS}^{D}(\alpha,\beta,t)} = \int_{0}^{T_r/2} \omega_{IS}^{D}(\alpha,\beta,t)dt - \int_{T_r/2}^{T_r} \omega_{IS}^{D}(\alpha,\beta,t)dt = d_{IS} \cdot \frac{\sqrt{2}\sin 2\beta \sin\alpha}{\pi} \neq 0 \qquad (1.7)$$

Thus, the dipolar evolution is accumulated after each rotor period, which can be described using the density operator.

$$\hat{\rho}(t) = \hat{U}(t) \cdot \hat{\rho}(0) \cdot \hat{U}^{-1}(t) \qquad (1.8)$$

$$\hat{U}(t) = e^{-i\overline{\hat{H}_{IS}^{tr}} \cdot t} = e^{-i\overline{\omega_{IS}^{D}} \cdot t \cdot 2\hat{I}_z\hat{S}_z} \qquad (1.9)$$

where $\hat{\rho}(t)$ is the density operator and $\hat{U}(t)$ is the dipolar interaction propagator at time t. Suppose right after cross polarization (CP) on the X channel (Figure 1.2A), $\hat{\rho}(0) = \hat{I}_x$. After N rotor periods,

$$\hat{\rho}(NT_r) = e^{-i\overline{\omega_{IS}^{D}} \cdot NT_r \cdot 2\hat{I}_z\hat{S}_z} \cdot \hat{I}_x \cdot e^{i\overline{\omega_{IS}^{D}} \cdot NT_r \cdot 2\hat{I}_z\hat{S}_z} \qquad (1.10)$$

With $[\overline{\hat{H}_{IS}^{tr}}, [\overline{\hat{H}_{IS}^{tr}}, \hat{I}_x]] = (\hbar\overline{\omega_{IS}^{D}})^2 \cdot \hat{I}_x$,

$$\hat{\rho}(NT_r) = \hat{I}_x \cos(\overline{\omega_{IS}^{D}} \cdot NT_r) + 2\hat{I}_y\hat{S}_z \sin(\overline{\omega_{IS}^{D}} \cdot NT_r) \qquad (1.11)$$

The dephased NMR signal is then:

$$S = tr(\hat{\rho}(NT_r) \cdot I_x) = tr(I_x^2) \cdot \cos(\overline{\omega_{IS}^{D}} \cdot NT_r) = S_0 \cdot \cos(\overline{\omega_{IS}^{D}} \cdot NT_r) \qquad (1.12)$$

Two spectra are collected to obtain the ratio of the dephased (S) and control (S_0) signals by turning the π pulses on and off (Figure 1.2A). For a powder sample, all internuclear vector orientations must be averaged (see equation 1.7):

$$\frac{S}{S_0} = <\cos(\overline{\omega_{IS}^{D}} \cdot NT_r)> = \frac{1}{2\pi}\int_0^{2\pi}\int_0^{\frac{\pi}{2}} \cos(\frac{\sqrt{2}\sin 2\beta \sin\alpha}{\pi} \cdot d_{IS}NT_r)\sin\beta d\beta d\alpha \qquad (1.13)$$

A universal curve can be plotted with $<\cos(\overline{\omega_{IS}^{D}} \cdot NT_r)>$ against $d_{IS}NT_r$ (Figure 1.2B). When $d_{IS}NT_r = 1.73$, the curve reaches its first minimum, corresponding to full dipolar dephasing. By fitting the experimental dephasings measured at different time points, the dipolar

coupling constant can be obtained, which, with $d_{IS} = -\hbar \frac{\mu_0}{4\pi} \frac{\gamma_I \gamma_S}{r_{IS}^3}$, gives the internuclear distance.

In practice, a central π pulse is applied on the detection channel X to refocus the isotropic chemical shift evolution, while other π pulses are applied on the indirect channel Y. To enhance the distance measurement accuracy, composite 90°180°90° π pulses are used on the Y channel to reduce the flip angle imperfections mainly caused by radio-frequency field inhomogeneity (*38*) (Figure 1.2A).

For selective dipolar coupling measurements, Gaussian soft π pulses (Figure 1.2A) are applied on both channels at the frequency of interest of both spins to recouple the desired internuclear dipolar coupling (*39*). Homonuclear J-coupling can be removed at the same time through selective excitation (*40*).

1.2.3 Dipolar-Chemical Shift Correlation (DIPSHIFT)

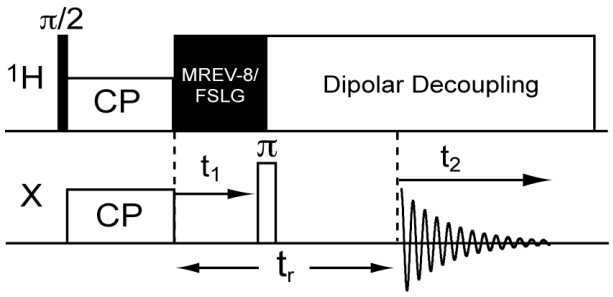

Figure 1.3. The pulse sequence of DIPSHIFT experiment.

The two-dimensional DIPSHIFT experiment (*41*) has been used to measure site-specific ^{1}H-X dipolar coupling, which gives information about molecular dynamics and hydrogen bonding. X represents heavy atoms such as ^{13}C and ^{15}N. When the molecule is rigid at low temperature, one-bond ^{1}H-X dipolar coupling directly translates to the bond length and hydrogen bonding information (*42, 43*). While the molecule becomes mobile at high temperature, motionally averaged ^{1}H-X dipolar coupling can provide information on the motional rate and geometry. Compared with other methods like static ^{2}H NMR (*44*) and 2D Lee-Goldburg CP (LG-CP) (*45, 46*), DIPSHIFT experiment has better intensity, is more

robust in measuring small couplings under low MAS speed, and avoids the broad ^{2}H quadrupolar spectrum, which provides special advantages in dynamics studies.

Due to the strong ^{1}H-^{1}H dipolar coupling, two main homonuclear decoupling schemes MREV-8 (*47*) and FSLG (*48*) are applied in the DIPSHIFT experiment during the ^{1}H-X dipolar evolution period with the scaling factors of 0.47 and 0.577. Moving the π pulse on the X channel partially recouples the ^{1}H-X dipolar coupling at each t_1 time within a rotor period (Figure 1.3). The ^{1}H-X dipolar coupling can be similarly obtained by fitting signal dephasings at different time points of one rotor period. For weak dipolar couplings, the coupling-doubled DIPSHIFT experiment (*49*) has been developed to increase the accuracy of the measurement.

1.3 Thesis Organization

This thesis presents the solid-state NMR studies on the structure and dynamics of His37 residue and the transmembrane backbone (22-46) of influenza AM2 proton channel in lipid bilayers. The thesis is mainly composed of published journal articles.

Chapter 1 summarizes the recent structural and functional studies of the influenza AM2 protein using physiological, biophysical and computational methods. A brief introduction of related NMR concepts and techniques is also given.

Chapter 2 studies the structural role of His37 in the proton conduction mechanism of the influenza AM2 channel. The protonation, tautomeric states, rotameric conformations and dynamics of His37 at both high and low pH have been investigated with 2D correlation experiments and dipolar coupling measurements. A His37 gating and proton conduction mechanism is proposed: in the high-pH closed state, edge-face interactions between His37 restrict the pore and prevent the formation of a continuous water wire. In the low-pH conducting state, extensively hydrogen-bonded His37 shuttles protons through the channel, facilitated by microsecond ring reorientations.

Chapter 3 discusses the conformational plasticity of the AM2 transmembrane domain under varying membrane thickness, pH and drug-binding environments. Coupled chemical shift perturbations are observed for multiple pore-lining residues. Three sets of backbone conformations are built with the chemical-shift-derived torsion angles, whose equilibrium

under different pH, membrane thickness and drug-binding conditions can correlate with the function of the AM2 proton channel.

Chapter 4 investigates the protonation process of His37 residue of the influenza AM2 TM peptide in the virus-envelope-mimetic membrane. pH-dependent proton exchange between His37 sidechain nitrogen and water is indicated from the ^{15}N line shape analysis. By quantifying the sidechain ^{15}N intensity at multiple pHs, four pKa values of the His37 tetrad in the AM2 channel are obtained to provide information on the distribution and the relative conductivity of each charged state of the AM2 channel. Adding amantadine significantly inhibits the His37 protonation, chemical exchange, and stops the sidechain motion, which supports the notion that proton conduction of the AM2 channel is achieved by ring-motion-assisted His37-water proton exchange.

At the end of the thesis, an appendix summarizes the synthesis of Fmoc-protected amino acids and the procedure for preparing membrane-incorporated peptide sample using dialysis reconstitution.

1.4 Copyright Permission

Chapter 2 and 3 are reprints of published papers. Copyright permissions have been obtained from the following publishing groups:

Chapter 2	American Association for the Advancement of Science
Chapter 3	Elsevier, license number 2633820887884

References

(1) Cady, S. D., Luo, W. B., Hu, F., and Hong, M. (2009) Structure and function of the influenza M2 proton channel. *Biochemistry 48*, 7356-7364.

(2) Ma, C., Polishchuk, A. L., Ohigashi, Y., Stouffer, A. L., Schön, A., Magavern, E., Jing, X., Lear, J. D., Freire, E., Lamb, R. A., DeGrado, W. F., and Pinto, L. H. (2009) Identification of the functional core of the influenza A virus A/M2 proton-selective ion channel. *Proc. Natl. Acad. Sci. USA 106*, 12283-12288.

(3) Holsinger, L. J., Nichani, D., Pinto, L. H., and Lamb, R. A. (1994) Influenza A virus M2 ion channel protein: a structure-function analysis. *J. Virol. 68*, 1551-1563.

(4) Mould, J. A., Li, H. C., Dudlak, C. S., Lear, J. D., Pekosz, A., Lamb, R. A., and Pinto, L. H. (2000) Mechanism for proton conduction of the M(2) ion channel of influenza A virus. *J. Biol. Chem. 275*, 8592-8599.

(5) Lin, T. I., and Schroeder, C. (2001) Definitive assignment of proton selectivity and attoampere unitary current to the M2 ion channel protein of influenza A virus. *J. Virol. 75*, 3647-3656.

(6) Chizhmakov, I. V., Geraghty, F. M., Ogden, D. C., Hayhurst, A., Antoniou, M., and Hay, A. J. (1996) Selective proton permeability and pH regulation of the influenza virus M2 channel expressed in mouse erythroleukaemia cells. *J. Physiol. 494*, 329-336.

(7) Mould, J. A., Drury, J. E., Frings, S. M., Kaupp, U. B., Pekosz, A., Lamb, R. A., and Pinto, L. H. (2000) Permeation and activation of the M2 ion channel of influenza A virus. *J. Biol. Chem. 275*, 31038-31050.

(8) Wang, C., Takeuchi, K., Pinto, L. H., and Lamb, R. A. (1993) Ion channel activity of influenza A virus M2 protein: characterization of the amantadine block. *J. Virol. 67*, 5585-5594.

(9) Bright, R. A., Medina, M. J., Xu, X., Perez-Oronoz, G., Wallis, T. R., Davis, X. M., Povinelli, L., Cox, N. J., and Klimov, A. I. (2005) Incidence of adamantane resistance among influenza A (H3N2) viruses isolated worldwide from 1994 to 2005: a cause for concern. *Lancet 366*, 1175-1181.

(10) Jing, X., Ma, C., Ohigashi, Y., Oliveira, F. A., Jardetzky, T. S., Pinto, L. H., and Lamb, R. A. (2008) Functional studies indicate amantadine binds to the pore of the influenza A virus M2 proton-selective ion channel. *Proc. Natl. Acad. Sci. USA 105*, 10967-10972.

(11) Stouffer, A. L., Acharya, R., Salom, D., Levine, A. S., Di Costanzo, L., Soto, C. S., Tereshko, V., Nanda, V., Stayrook, S., and DeGrado, W. F. (2008) Structural basis for the function and inhibition of an influenza virus proton channel. *Nature 451*, 596-599.

(12) Schnell, J. R., and Chou, J. J. (2008) Structure and mechanism of the M2 proton channel of influenza A virus. *Nature 451*, 591-595.

(13) Cady, S. D., Schmidt-Rohr, K., Wang, J., Soto, C. S., DeGrado, W. F., and Hong, M. (2010) Structure of the amantadine binding site of influenza M2 proton channels in lipid bilayers. *Nature 463*, 689-692.

(14) Rosenberg, M. R., and Casarotto, M. G. (2010) Coexistence of two adamantane binding sites in the influenza A M2 ion channel. *Proc. Natl. Acad. Sci. USA 107*, 13866-13871.

(15) Wang, C., Lamb, R. A., and Pinto, L. H. (1995) Activation of the M2 ion channel of influenza virus: a role for the transmembrane domain histidine residue. *Biophys. J. 69*, 1363-1371.

(16) Venkataraman, P., Lamb, R. A., and Pinto, L. H. (2005) Chemical rescue of histidine selectivity filter mutants of the M2 ion channel of influenza A virus. *J. Biol. Chem. 280*, 21463-21472.

(17) Howard, K. P., Lear, J. D., and Degrado, W. F. (2002) Sequence determinants of the energetics of folding of a transmembrane four-helix-bundle protein. *Proc. Natl. Acad. Sci. USA 99*, 8568-8572.

(18) Sansom, M. S., Kerr, I. D., Smith, G. R., and Son, H. S. (1997) The influenza A virus M2 channel: a molecular modeling and simulation study. *Virology 233*, 163-173.

(19) Wu, Y., and Voth, G. A. (2005) A computational study of the closed and open states of the influenza a M2 proton channel. *Biophys. J. 89*, 2402-2411.

(20) Smondyrev, A. M., and Voth, G. A. (2002) Molecular dynamics simulation of proton transport through the influenza A virus M2 channel. *Biophys. J. 83*, 1987-1996.

(21) Pinto, L. H., Dieckmann, G. R., Gandhi, C. S., Papworth, C. G., Braman, J., Shaughnessy, M. A., Lear, J. D., Lamb, R. A., and DeGrado, W. F. (1997) A functionally defined model for the M2 proton channel of influenza A virus suggests a mechanism for its ion selectivity. *Proc. Natl. Acad. Sci. USA 94*, 11301-11306.

(22) Acharya, R., Carnevale, V., Fiorin, G., Levine, B. G., Polishchuk, A. L., Balannik, V., Samish, I., Lamb, R. A., Pinto, L. H., Degrado, W. F., and Klein, M. L. (2010) Structure and mechanism of proton transport through the transmembrane tetrameric

M2 protein bundle of the influenza A virus. *Proc. Natl. Acad. Sci. USA 107*, 15075-15080.

(23) Sharma, M., Yi, M., Dong, H., Qin, H., Peterson, E., Busath, D. D., Zhou, H. X., and Cross, T. A. (2010) Insight into the mechanism of the influenza A proton channel from a structure in a lipid bilayer. *Science 330*, 509-512.

(24) Hu, F., Luo, W., and Hong, M. (2010) Mechanisms of proton conduction and gating in influenza M2 proton channels from solid-state NMR. *Science 330*, 505-508.

(25) Hu, J., Fu, R., Nishimura, K., Zhang, L., Zhou, H. X., Busath, D. D., Vijayvergiya, V., and Cross, T. A. (2006) Histidines, heart of the hydrogen ion channel from influenza A virus: toward an understanding of conductance and proton selectivity. *Proc. Natl. Acad. Sci. USA 103*, 6865-6870.

(26) Hu, J., Riqiang, F., and Cross, T. A. (2007) The chemical and dynamical influence of the anti-viral drug amantadine on the M2 proton channel transmembrane domain. *Biophys. J. 93*, 276-283.

(27) Tang, Y., Zaitseva, F., Lamb, R. A., and Pinto, L. H. (2002) The gate of the influenza virus M2 proton channel is formed by a single tryptophan residue. *J. Biol. Chem. 277*, 39880-39886.

(28) Gandhi, C. S., Shuck, K., Lear, J. D., Dieckmann, G. R., DeGrado, W. F., Lamb, R. A., and Pinto, L. H. (1999) Cu(II) inhibition of the proton translocation machinery of the influenza A virus M2 protein. *J. Biol. Chem. 274*, 5474-5482.

(29) Luo, W., Mani, R., and Hong, M. (2007) Sidechain conformation of the M2 transmembrane peptide proton channel of influenza a virus from 19F solid-state NMR. *J. Phys. Chem. 111*, 10825-10832.

(30) Nishimura, K., Kim, S., Zhang, L., and Cross, T. A. (2002) The closed state of a H+ channel helical bundle combining precise orientational and distance restraints from solid state NMR. *Biochemistry 41*, 13170-13177.

(31) Chen, B. J., Leser, G. P., Jackson, D., and Lamb, R. A. (2008) The influenza virus M2 protein cytoplasmic tail interacts with the M1 protein and influences virus assembly at the site of virus budding. *J. Virol. 82*, 10059-10070.

(32) McCown, M. F., and Pekosz, A. (2006) Distinct domains of the influenza a virus M2 protein cytoplasmic tail mediate binding to the M1 protein and facilitate infectious virus production. *J. Virol. 80*, 8178-8189.

(33) Schroeder, C., Heider, H., Möncke-Buchner, E., and Lin, T. I. (2005) The influenza virus ion channel and maturation cofactor M2 is a cholesterol-binding protein. *Eur. Biophys. J. 34*, 52-66.

(34) Rossman, J. S., Jing, X., Leser, G. P., and Lamb, R. A. (2010) Influenza virus M2 protein mediates ESCRT-independent membrane scission. *Cell 142*, 902-913.

(35) Nguyen, P. A., Soto, C. S., Polishchuk, A. L., Caputo, G. A., Tatko, C. D., Ma, C., Ohigashi, Y., Pinto, L. H., Degrado, W. F., and Howard, K. P. (2008) pH-induced conformational change of the influenza M2 protein C-terminal domain. *Biochemistry 47*, 9934-9936.

(36) Schmidt-Rohr, K., and Spiess, H. W. (1994) *Multidimensional Solid-State NMR and Polymers*, Academic Press, San Diego.

(37) Gullion, T., and Schaefer, J. (1989) Rotational echo double resonance NMR. *J. Magn. Reson. 81*, 196-200.

(38) Sinha, N., Schmidt-Rohr, K., and Hong, M. (2004) Compensation for pulse imperfections in rotational-echo double-resonance NMR by composite pulses and EXORCYCLE. *J. Magn. Reson. 168*, 358-365.

(39) Jaroniec, C. P., Tounge, B. A., Herzfeld, J., and Griffin, R. G. (2001) Frequency selective heteronuclear dipolar recoupling in rotating solids: accurate 13C-15N distance measurements in uniformly 13C, 15N-labeled peptides. *J. Am. Chem. Soc. 123*, 3507-3519.

(40) Jaroniec, C. P., Tounge, B. A., Rienstra, C. M., Herzfeld, J., and Griffin, R. G. (1999) Measurement of 13C-15N distances in uniformly 13C labeled biomolecules: J-decoupled REDOR. *J. Am. Chem. Soc. 121*, 10237-10238.

(41) Munowitz, M. G., Griffin, R. G., Bodenhausen, G., and Huang, T. H. (1981) Two-dimensional rotational spin-echo NMR in solids: correlation of chemical shift and dipolar interactions. *J. Am. Chem. Soc. 103*, 2529-2533.

(42) Roberts, J. E., Harbison, G. S., Munowitz, M. G., Herzfeld, J., and Griffin, R. G. (1987) Measurement of heteronuclear bond distances in polycrystalline solids by solid-state NMR techniques. *J. Am. Chem. Soc 109*, 4163-4169.

(43) Song, X. J., Rienstra, C. M., and McDermott, A. E. (2001) N-H bond stretching in histidine complexes: a solid-state NMR study. *Magn. Reson. Chem. 39*, S30-S36.

(44) Davis, J. H., Jeffrey, K. R., Bloom, M., Valic, M. I., and Higgs, T. P. (1976) Quadrupolar echo deuteron magnetic resonance spectroscopy in ordered hydrocarbon chains. *Chem. Phys. Lett. 42*, 390-394.

(45) van Rossum, B. J., de Groot, C. P., Ladizhansky, V., Vega, S., and de Groot, H. J. M. (2000) A method for measuring heteronuclear (1H-13C) distances in high speed MAS NMR. *J. Am. Chem. Soc 122*, 3465-3472.

(46) Hong, M., Yao, X. L., Jakes, K., and Huster, D. (2002) Investigation of molecular motions by Lee-Goldburg cross-polarization NMR spectroscopy. *J. Phys. Chem. B 106*, 7355-7364.

(47) Rhim, W.-K., Elleman, D. D., and Vaughan, R. W. (1973) Analysis of multiple-pulse NMR in solids. *J. Chem. Phys. 59*, 3740-3749.

(48) Bielecki, A., Kolbert, A. C., and Levitt, M. H. (1989) Frequency-switched pulse sequences: homonuclear decoupling and dilute spin NMR in solids. *Chem. Phys. Lett. 155*, 341-346.

(49) Hong, M., Gross, J. D., Rienstra, C. M., Griffin, R. G., Kumashiro, K. K., and Schmidt-Rohr, K. (1997) Coupling amplification in 2D MAS NMR and its application to torsion angle determination in peptides. *J. Magn. Reson. 129*, 85-92.

Chapter 2

Mechanisms of Proton Conduction and Gating in Influenza M2 Proton Channels from Solid-State NMR

A paper published in Science

2010, vol. 330 pp. 505-508

Fanghao Hu, Wenbin Luo, and Mei Hong

Abstract

The M2 protein of influenza viruses forms an acid-activated tetrameric proton channel. We used solid-state nuclear magnetic resonance spectroscopy to determine the structure and functional dynamics of the pH-sensing and proton-selective histidine-37 in M2 bound to a cholesterol-containing virus-envelope-mimetic membrane so as to better understand the proton conduction mechanism. In the high-pH closed state, the four histidines form an edge-face π-stacked structure, preventing the formation of a hydrogen-bonded water chain to conduct protons. In the low-pH conducting state, the imidazoliums hydrogen-bond extensively with water, and undergo microsecond ring reorientations with an energy barrier greater than 59 kilojoules per mole. This barrier is consistent with the temperature dependence of proton conductivity, suggesting that histidine-37 dynamically shuttles protons into the virion. We propose a proton conduction mechanism in which ring-flip-assisted imidazole deprotonation is the rate-limiting steps.

Results and Discussion

Proton transport by synthetic materials is mediated either solely by hydrogen-bonded water, as in hydrated ionic polymers (*1*), or solely by titratable heterocycles such as imidazoles tethered to the backbone of anhydrous polymers (*2*). In comparison, the conduction mechanism of biological proton channels in cell membranes is more complex because both water and titratable protein sidechains are usually present (*3*). The influenza M2 protein forms a tetrameric proton channel important for the virus lifecycle (*4*). Activated below pH 6, the M2 channel conducts 10 – 10,000 protons per second (*5, 6*). The pH-sensing and proton-selective residue is a single histidine, His37, in the transmembrane (TM) domain

(*7*). ^{15}N chemical shifts of His37 in DMPC/DMPG bilayers indicated that the four histidines titrate with pKa's of 8.2, 8.2, 6.3 and <5.0, thus the third protonation event is responsible for channel activation (*8*). However, the precise role of His37 in proton conduction is still contested. Two models have been proposed. In the "shutter" model, the pore at His37 is enlarged by electrostatic repulsion among the imidazoliums, permitting a continuous hydrogen-bonded water chain over which protons hop by the Grotthuss mechanism (*9, 10*). The rate-limiting step is proton hopping across three or four charged imidazoliums, with a calculated energy barrier of 29-42 kJ/mol (*9*). In the "shuttle" model, His37 actively participates in proton relay by protonation and deprotonation. Tautomerization or ring flips reestablish the original conformation required for the next proton relay (*11*). The rate-limiting step in this model is the His37 conformational change.

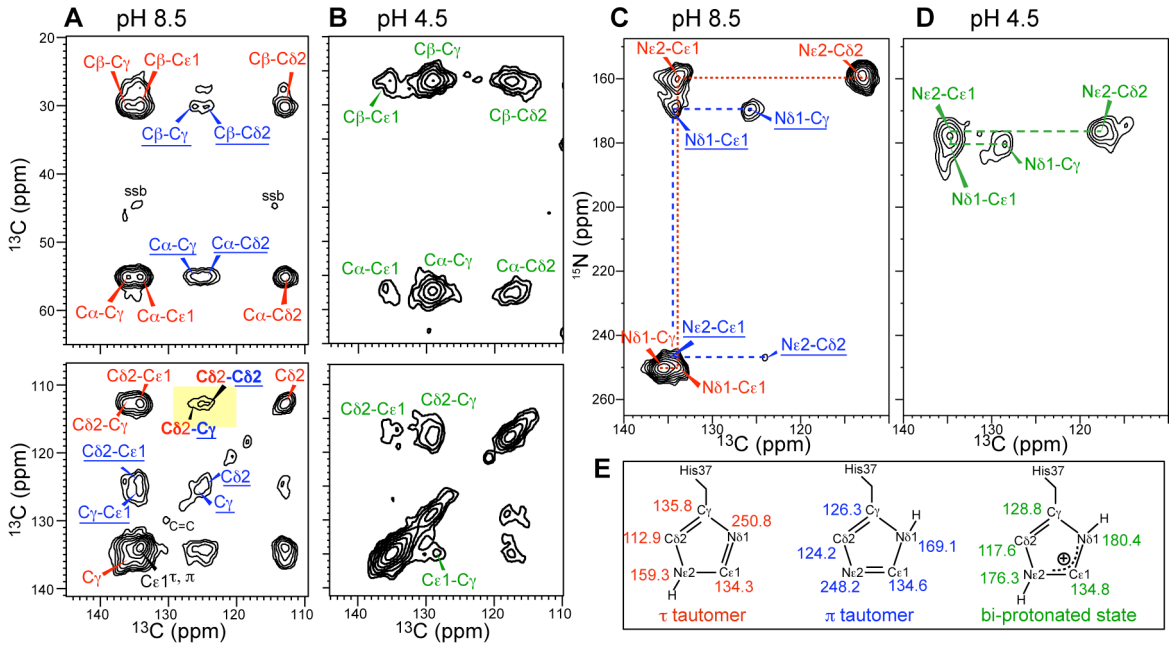

Figure 2.1. ^{15}N and ^{13}C chemical shifts of His37-labeled M2TM in viral membranes reveal pH-dependent imidazole protonation and tautomeric structures. (A-B) 2D ^{13}C-^{13}C correlation spectra. (A) pH 8.5. (B) pH 4.5. The τ- and π-tautomer peaks are assigned in red and blue, and the charged His37 peaks in green. (C-D) 2D ^{15}N-^{13}C correlation spectra. (C) pH 8.5. (D) pH 4.5. (E) Summary of the imidazole chemical shifts.

Although high-resolution structures of the M2 TM domain (M2TM) in detergents at high and low pH have been reported (*12, 13*), the His37 sidechain conformations differed in these structures, and sidechain dynamics and water interactions were not probed. Further, detergent molecules can perturb the packing of weakly bound membrane protein complexes, thus the structures may not accurately reflect the chemistry of the imidazoles in the lipid membrane.

To elucidate the proton conduction mechanism of M2, we used solid-state NMR to determine the structure and dynamics of His37 in M2TM reconstituted into a cholesterol-rich virus-envelope-mimetic lipid membrane (*14*). Extensive data yielded the His37 protonation, tautomerization, rotameric conformation, sidechain dynamics and hydrogen bonding from pH 8.5 to 4.5. Here we focus on pH 8.5 for the closed channel and pH 4.5 for the conducting channel. M2TM exhibits acid-activated and amantadine-sensitive proton currents similar to the intact protein (*15*), and fully assembles into four-helix bundles (*16*) in the viral membrane with immobilized backbones (*14*), which allowed His37 sidechain motion to be elucidated.

Histidine ^{15}N and ^{13}C chemical shifts are exquisitely sensitive to the protonation and tautomeric structure of imidazoles. Deprotonation increases the ^{15}N chemical shift by ~80 ppm (*17*), and Cγ/Cδ2 chemical shifts also depend systematically on the imidazole structure (*18*). Two-dimensional ^{13}C-^{13}C and ^{15}N-^{13}C correlation spectra of His37-labeled M2TM revealed only neutral imidazoles at pH 8.5. The Nε2-protonated τ-tautomer and Nδ1-protonated π-tautomer exist at a ~3 : 1 ratio (Figure 2.1) with slow or no exchange at ambient temperature (Figure 2.S1). Inter-tautomer Cδ2(τ)-Cγ(π) and Cδ2(τ)-Cδ2(π) cross peaks (Figure 2.1A) indicate that both tautomers exist in each channel. The ~25% fraction of the π-tautomer is much higher than in small imidazole-containing compounds (*17*), suggesting stabilization of the protonated Nδ1(π) by hydrogen bonding (*19*).

At pH 4.5, both Nδ1 and Nε2 exhibit protonated chemical shifts (170-180 ppm); no unprotonated signal was observed at 250 ppm (Figure 2.S1), indicating that the neutral species is below the detection limit (≤5%). The charged imidazoliums showed much larger linewidths than the neutral species (Table 2.S1), indicating broader conformational distribution of the protein at low pH.

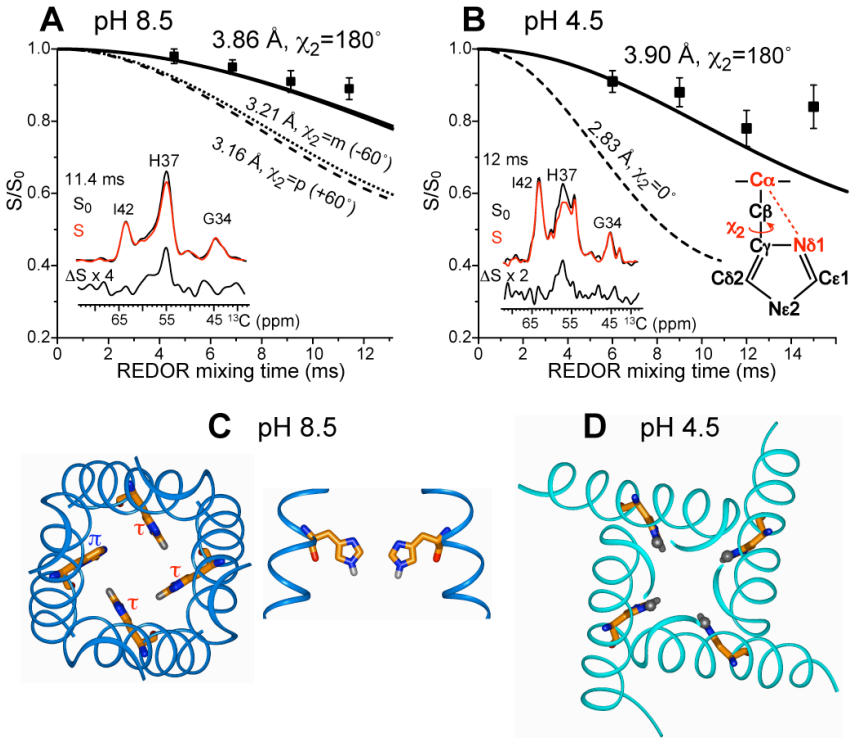

Figure. 2.2. His37 rotameric conformation from Cα-Nδ1 distances. (A) pH 8.5 data, with representative REDOR control (S_0), dephased (S), and difference (ΔS) spectra. The 3.9-Å distance indicates χ_2=180°. (B) pH 4.5 data, showing a similar distance and χ_2 angle. (C) Top and side views of the His37 tetrad in the *tt* rotamer in the high-pH structure (PDB: 2KQT) (*21*). (D) Top view of the His37 tetrad in the *tt* rotamer in the low-pH structure (PDB: 3C9J) (*13*).

We probed interhelical packing of the His37 tetrad through χ_1 and χ_2-dependent backbone-sidechain distances. The Cα-Nδ1 distance constrains the χ_2 torsion angle, whereas the Cδ2-Nα distance constrains both χ_1 and χ_2 angles. At both pH, the Cα-Nδ1 distance was 3.9 Å (Figure 2.2, Figure 2.S2), which ruled out the +60° and -60° χ_2 rotamers and was only consistent with the 180° rotamer. Similar experiments yielded a Cδ2-Nα distance of 4.4–4.9 Å (Figure 2.S3), which ruled out the χ_1=-60° rotamer. Thus, the high-pH τ-tautomer adopts the *tt* rotamer, consistent with interhelical His37-Trp41 (*20*) and Trp41-Trp41 distances (*16*). At pH 4.5, the Cα-Nδ1 (3.9 Å), Cα-Nε2 (4.4 Å), and Cδ2-Nα (>4.5 Å) distances similarly indicated the *tt* conformation (Figure 2.2B, 2.S3).

Placing the His37 rotamer into the different backbone structures at low pH and high pH revealed strikingly different packing of the imidazole tetrad (Figure 2.2C, D). In the closed channel (*21*), the major τ-tautomers pack in an edge-face fashion where each Cε1-Hε1 bond points to the center of the neighboring ring. The packing is tight, with a nearest-neighbor Cε1-Nε2 distance of ~4.9 Å, consistent with inter-tautomer cross peaks and suggesting aromatic CH-π interaction (*22*). The high density of π-electrons should repel water oxygens and orient them in opposite directions across the tetrad, thus disabling proton conduction. The tetrad dimension is still possible for metal-ion coordination (*23*), which may explain Cu^{2+} inhibition of M2 (*24*). The minor π-tautomer can readily maintain the four-fold symmetry by adopting *tt* or *t0* rotamer. In comparison, in the low-pH structure (*13*), the imidazoliums show no edge-face stacking and leave a much wider pore.

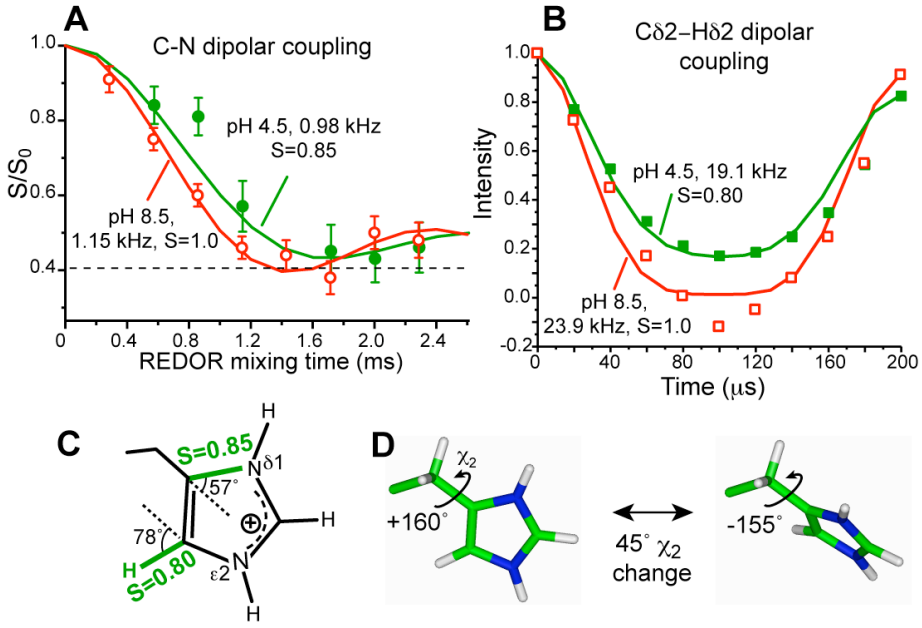

Figure 2.3. His37 sidechains reorient at low pH but remain static at high pH at physiological temperature. (A) 303 K ^{13}C-^{15}N dipolar couplings. At pH 8.5, a 1:1 combination of Cγ-Nδ1 and Cε1-Nδ1 couplings reaches the rigid limit. At pH 4.5, the dominant Cγ-Nδ1 coupling is motionally averaged. (B) Cδ2-Hδ2 coupling at 308 K is motionally averaged at pH 4.5 but in the rigid limit at pH 8.5. (C) Measured order parameters at pH 4.5. (D) Two-site jump of imidazolium at low pH. A 45° reorientation around the Cβ-Cγ bond uniquely fits the observed order parameters.

The significant packing difference suggests that His37 sidechains may be immobilized at high pH but dynamic at low pH. To test this hypothesis, we measured one-bond Cγ-Nδ1 and Cδ2-Hδ2 dipolar couplings at physiological temperature. The viral membrane immobilized the protein backbone, giving Nα-H and Cα-Hα order parameters of 1.0 (*14*) (Figure 2.S4, 2.S5), thus isolating potential sidechain motion. Fast motions scale the couplings by an order parameter (*S*) that reflects the motional amplitude. At pH 8.5, we obtained rigid-limit Cγ-Nδ1 and Cε1-Nδ1 couplings (1.15 kHz, 1.39 Å) and a rigid-limit Cδ2-Hδ2 coupling (23.9 kHz, 1.08 Å) (Figure 2.3A, B), confirming immobilization of the neutral imidazoles by edge-face stacking. However, at pH 4.5, the Cγ-Nδ1 and Cδ2-Hδ2 couplings are scaled by a factor of 0.85 and 0.80, respectively (Figure 2.3C), indicating sidechain motion. The availability of two order parameters uniquely constrained the geometry of the imidazolium motion. The most likely motional axis is the Cβ-Cγ bond (*25*). Uniaxial rotation is ruled out because it predicts a very small $S_{C\gamma-N\delta1}$ of 0.06 due to the 57° angle of the Cγ-Nδ1 bond to the Cβ-Cγ axis. The well-known 180° ring flip motion is also ruled out, because it has little effect on the Cδ2-Hδ2 coupling ($S_{C\delta2-H\delta2}$ = 0.94) (Table 2.S2). The near-invariance of the Cδ2-Hδ2 coupling to 180° ring flips also rules out a scenario where some imidazoliums undergo ring flips while others remain static (Figure 2.S6). Instead, analysis of the *S* dependence on χ_2 angles shows that only two-site jumps with a χ_2 change of 45° satisfies both the Cγ-Nδ1 and Cδ2-H order parameters (Figure 2.S7). Given the average χ_2 of 180° at low temperature, the most likely instantaneous χ_2 angles are about 160° and -155° (Figure 2.3D).

The restricted nature of the imidazolium ring reorientation may result from the symmetric low pH across the bilayer in the NMR samples, since the imidazoles may not need to reorient significantly to be reprotonated. When a proton concentration gradient exists, as in the virus membrane, full ring flips may occur to reprotonate the imidazoles. The motion must be much faster than 10^4 s^{-1} to average the Cδ2-Hδ2 coupling. Temperature-dependent Cδ2-Hδ2 couplings from 308 K to 243 K indicated that the imidazolium was frozen by 263 K but fully mobile at 293 K (Figure 2.S8). Using a lower-limit of 50 kHz for the 293-K rate and an

upper-limit of 3 kHz for the 263-K rate, we obtained an energy barrier of > 59 kJ/mol, consistent with the 50-120 kJ/mol reported for imidazole motions in synthetic proton conductors (*26*). M2 proton conductivities differ by 14-fold between 18°C and 37°C at pH 5.7 (*5*), indicating an energy barrier of 104 kJ/mol. Thus, the barrier of imidazolium motion is consistent with the functional data, while the barrier for water-mediated proton hopping (29-42 kJ/mol) is not (*9*), suggesting that His37 ring reorientation is directly involved in proton transport, as in the "shuttle" model. Imidazole motion was also observed at the physiological pH of 6.0 and 5.2 where the channel first opens, and where both charged and neutral histidines were present (Figure 2.S8) (*7, 8*). Thus, His37 motion appears to be an intrinsic property of the spacious conducting channel, although its precise amplitudes and rates may vary with pH.

Water is still necessary for delivering protons to the imidazoles before they can be relayed to the virus interior. Thus water-His37 hydrogen bonding is implied in the shuttle model. We probed hydrogen-bond (H-bond) formation by measuring imidazole N-H and C-H dipolar couplings at 243 K, where the sidechain was frozen. H-bond formation stretches the N-H and C-H bonds from their covalent lengths (1.03 Å and 1.10 Å), thus weakening dipolar couplings (*27*). At pH 8.5, the protonated Nδ1(π) showed a significantly stretched N-H bond of 1.08 Å, indicating hydrogen bonding and explaining the π-tautomer stabilization. Even the unprotonated Nδ1(τ) showed a sizeable coupling of 2.1 kHz, suggesting a nearest-proton distance of 1.8 Å and a weak Nδ1…H-O H-bond. In contrast, the protonated Nε2(τ) exhibited an unstretched bond length of 1.03 Å (11.1 kHz) (Figure 2.4A), despite the presence of a small amount of water in the H37-W41 region based on Nε2(τ)-water cross peaks in 2D ^{15}N-^{1}H spectra (Figure 2.S9). At pH 4.5, the combined Nδ1/Nε2 peak showed a reduced N-H coupling of 8.8 kHz, indicating a stretched bond of 1.11 Å. Given the spaciousness of the low-pH pore, the H-bond acceptors cannot be another imidazolium. Trp41-His37 aromatic interaction is also unlikely to stretch the Nε2-H bond, since the function of Trp41 is to keep His37 neutral under high pH_{out} and low pH_{in} to prevent outward currents (*28*), which implies that Trp41 should interact mainly with neutral His37. Thus the most likely cause for N-H bond elongation at low pH is H-bond with frozen water, which is

more abundant in the low-pH channel than the high-pH channel, as shown by spin diffusion NMR (*29*) and MD simulations (*9*, *30*).

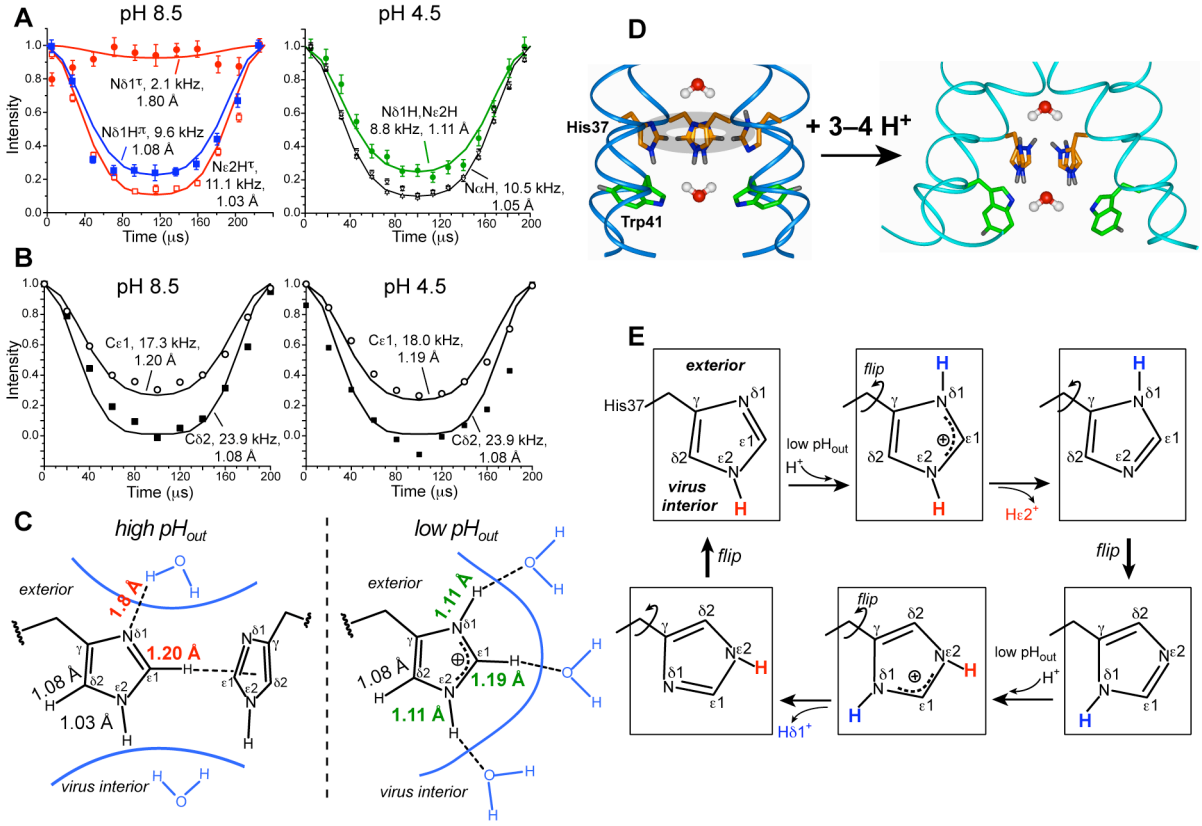

Figure 2.4. Charged His37 hydrogen-bonds with water and undergoes ring flips to relay protons. (A) N-H dipolar couplings at 243 K. At pH 8.5, Nε2(τ) is not hydrogen-bonded while Nδ1(π) is. The unprotonated Nδ1(τ) shows a weak H-bond. At pH 4.5, both nitrogens show weak couplings and bond stretching. (B) C-H dipolar couplings of Cδ2 and Cε1 at 243 K. The Cε1-Hε1 bond is stretched while Cδ2-Hδ2 is not. (C) Imidazole bond lengths and H-bond networks at high and low pH. (D) His37 structure and dynamics and proposed water orientations across the tetrad. Trp41 may interact with His37 at high pH_{out}. (E) Proposed imidazole structural changes in a cycle where multiple ring reorientations mediate the transfer of two protons.

Similar C-H coupling measurements revealed that the Cδ2-Hδ2 bond was unstretched (1.08 Å) at either pH while the Cε1-Hε1 bond was stretched to 1.20 Å at pH 8.5 and 1.19 Å

at pH 4.5 (Figure 2.4B). The latter may be attributed to CH-π interactions at high pH and H-bond with water at low pH. The imidazole Cε1-Hε1 bond is known to be prone to elongation due to its acidic nature (*31*), although the large magnitude of stretching observed here requires further investigation.

These bond lengths reveal an extensive H-bond network that covers three sides of the imidazolium at low pH (Figure 2.4C), creating a continuous hydrogen-bonded chain. Similar to the histidine in the catalytic triad of serine proteases, Cε1 hydrogen bonding may facilitate Nε2 deprotonation by evenly distributing the positive charge and increasing Nε2 electronegativity (*25, 32*). At high pH, the H-bond network is incomplete, excluding Nε2, which we attribute to the opposing water orientation and possible His37-Trp41 interactions (Figure 2.4D).

Taken together, these data suggest the following mechanism for proton gating and conduction by M2 (Figure 2.4D, E). At high pH_{out} the neutral imidazoles form tightly packed electron-rich CH-π stacks, preventing the formation of a hydrogen-bonded water chain. The outward-facing Nδ1(π) hydrogen-bonds with water, while the inward-facing Nε2 does not. Lowering pH_{out} protonates Nδ1, resulting in several imidazoliums per channel, which repel each other and cause backbone conformational changes that widen the pore (*33, 34*). More water permeates this region (*29*), establishing a hydrogen-bonded chain that includes His37. The larger pore frees the imidazoliums to undergo microsecond ring reorientations. We propose a proton conduction mechanism in which imidazolium deprotonation is facilitated by Cε1-Hε1 hydrogen bonding, and where continuous ring flips achieve the dual purpose of properly aligning the charged imidazolium with the C-terminal water molecules to cause proton transfer, and then pointing the unprotonated nitrogen to the low-pH extracellular side to be reprotonated. Our data indicate that the highest energy barrier of this process is the imidazolium motion, which may account for the temperature dependence of M2 proton conductance, possibly in combination with an additional small barrier for proton transfer (*5*). This dynamically assisted proton transfer model is consistent with the observed deuterium isotope effect, whose magnitude also suggested a mixed hydrogen-bonded chain with dissimilar elements (*6*). Thus, the present data strongly suggest that His37 is actively involved in proton conduction by M2. The structural information obtained here is largely

invisible to conventional high-resolution techniques, and demonstrates the ability of solid-state NMR to elucidate functionally important membrane protein dynamics and chemistry.

References and Notes

1. K. A. Mauritz, R. B. Moore, *Chem. Rev.* **104**, 4535 (2004).
2. S. Bureekaew *et al.*, *Nat. Mater.* **8**, 831 (2009).
3. J. F. Nagle, H. J. Morowitz, *Proc. Natl. Acad. Sci. USA* **75**, 298 (1978).
4. S. D. Cady, W. B. Luo, F. Hu, M. Hong, *Biochemistry* **48**, 7356 (2009).
5. T. I. Lin, C. Schroeder, *J. Virol.* **75**, 3647 (2001).
6. J. A. Mould *et al.*, *J. Biol. Chem.* **275**, 8592 (2000).
7. C. Wang, R. A. Lamb, L. H. Pinto, *Biophys. J.* **69**, 1363 (1995).
8. J. Hu *et al.*, *Proc. Natl. Acad. Sci. USA* **103**, 6865 (2006).
9. H. Chen, Y. Wu, G. A. Voth, *Biophys. J.* **93**, 3470 (2007).
10. A. Okada, T. Miura, H. Takeuchi, *Biochemistry* **40**, 6053 (2001).
11. L. H. Pinto *et al.*, *Proc. Natl. Acad. Sci. USA* **94**, 11301 (1997).
12. J. R. Schnell, J. J. Chou, *Nature* **451**, 591 (2008).
13. A. L. Stouffer *et al.*, *Nature* **451**, 596 (2008).
14. W. Luo, S. D. Cady, M. Hong, *Biochemistry* **48**, 6361 (2009).
15. C. Ma *et al.*, *Proc. Natl. Acad. Sci. USA* **106**, 12283 (2009).
16. W. Luo, R. Mani, M. Hong, *J. Phys. Chem.* **111**, 10825 (2007).
17. M. Munowitz, W. W. Bachovchin, J. Herzfeld, C. M. Dobson, R. G. Griffin, *J. Am. Chem. Soc.* **104**, 1192 (1982).
18. B. Henry, P. Tekely, J. J. Delpuech, *J. Am. Chem. Soc.* **124**, 2025 (2002).
19. W. W. Bachovchin, J. D. Roberts, *J. Am. Chem. Soc.* **100**, 8041 (1978).
20. K. Nishimura, S. Kim, L. Zhang, T. A. Cross, *Biochemistry* **41**, 13170 (2002).
21. S. D. Cady *et al.*, *Nature* **463**, 689 (2010).
22. M. L. Waters, *Curr. Opin. Chem. Biol.* **6**, 736 (2002).
23. L. S. Brinen, W. S. Willett, C. S. Craik, R. J. Fletterick, *Biochemistry* **35**, 5999 (1996).
24. C. S. Gandhi *et al.*, *J. Biol. Chem.* **274**, 5474 (1999).

25. E. L. Ash *et al*., *Proc*. *Natl*. *Acad*. *Sci*. *USA* **97**, 10371 (2000).

26. I. Fischbach, H. W. Spiess, K. Saalwachter, G. R. Goward, *J*. *Phys*. *Chem*. **108**, 18500 (2004).

27. X. J. Song, C. M. Rienstra, A. E. McDermott, *Magn*. *Reson*. *Chem*. **39**, S30 (2001).

28. Y. Tang, F. Zaitseva, R. A. Lamb, L. H. Pinto, *J*. *Biol*. *Chem*. **277**, 39880 (2002).

29. W. Luo, M. Hong, *J*. *Am*. *Chem*. *Soc*. **132**, 2378 (2010).

30. M. Yi, T. A. Cross, H. X. Zhou, *J*. *Phys*. *Chem*. *B* **112**, 7977 (2008).

31. S. Scheiner, T. Kar, J. Pattanayak, *J*. *Am*. *Chem*. *Soc*. **124**, 13257 (2002).

32. Z. S. Derewenda, U. Derewenda, P. M. Kobos, *J*. *Mol*. *Biol*. **241**, 83 (1994).

33. E. Khurana *et al*., *Proc*. *Natl*. *Acad*. *Sci*. *USA* **106**, 1069 (2009).

34. M. Yi, T. A. Cross, H. X. Zhou, *Proc*. *Natl*. *Acad*. *Sci*. *USA* **106**, 13311 (2009).

35. We thank Dr. Shenhui Li for discussions. This work was supported by NSF grant MCB-543473 and NIH grant GM088204.

Supporting Information

Materials and Methods

Membrane sample preparation

The transmembrane domain (residues 22-46, SSDPLVVAAS IIGILHLILW ILDRL) of the M2 protein of the influenza A Udorn strain was synthesized by PrimmBiotech (Cambridge, MA) using Fmoc solid-phase peptide synthesis protocols and was purified to >95% purity. The peptide used in this study was ^{13}C, ^{15}N-labeled at Gly34, His37 and Ile42. Fmoc-U-^{13}C, ^{15}N-His-trityl-OH was purchased from Sigma-Aldrich, and Fmoc protection of U-^{13}C, ^{15}N-labeled Gly and Ile were carried out in-house.

All phospholipids and cholesterol were purchased from Avanti Polar Lipids. A virus-envelope-mimetic membrane mixture including DPPC, DPPE, egg sphingomyelin (SPM) and cholesterol (Chol) (*1*) was used to reconstitute M2TM. This membrane mixture resembles the virus-envelope lipid composition, and gives higher-resolution protein spectra than model phosphocholine membranes. More importantly, the virus-mimetic membrane immobilizes the M2TM backbone at ambient temperature, in contrast to model lipid membranes, thus enabling sidechain dynamics to be extracted (*1-3*). To prepare the viral membrane, we dissolved sphingomyelin in a chloroform/methanol (5:1) solution and mixed it with DPPC, DPPE and cholesterol in chloroform at a molar ratio of SPM:DPPC:DPPE:Chol = 28:21:21:30. The solution was dried under a stream of nitrogen gas, suspended in cyclohexane and lyophilized. The dry lipid powder was resuspended in 1 mL buffer solution of defined pH, votexed, and free-thawed eight times to create uniform lipid vesicles. M2TM powder was codissolved with octyl-β-D-glucopyranoside (OG) in 1 mL of the buffer at an OG concentration of 20 mg/mL. The solution was then mixed with 1 mL lipid vesicle solution, votexed for 2 hours and dialyzed with a 3.5-kDa molecular weight cutoff against 1 L buffer at 4°C for 3 days with buffer changes every 8-12 hours to remove the detergent. The protein-lipid precipitate usually appeared after one day. The proteoliposome solution was centrifuged at 150,000g and 6 °C for 4 hours to yield a membrane pellet with a hydration level of ~40 wt%. The final protein : lipid molar ratio was 1 : 15. The pellet was packed into 4 mm MAS rotors for solid-state NMR experiments.

Four membrane samples at different pH were prepared for this study. A pH 8.5 sample was prepared in a Tris buffer containing 10 mM Tris, 1 mM EDTA, and 0.1 mM NaN_3. A pH 6.0 sample was prepared using a Bis-Tris buffer (10 mM Bis-Tris, 1 mM EDTA, and 0.1 mM NaN_3). A pH 4.5 and pH 5.2 sample were prepared using a citrate buffer containing 10 mM citric acid/sodium citrate, 1 mM EDTA, and 0.1 mM NaN_3.

Solid-state NMR experiments

Solid-state NMR experiments were carried out on a Bruker DSX-400 MHz spectrometer at 9.4 Tesla and an AVANCE 600 MHz spectrometer at 14.1 Tesla (Karlsruhe, Germany). Magic-angle-spinning (MAS) probes with 4-mm diameter spinners were used. Typical radiofrequency (rf) pulse lengths were 5 μs for ^{13}C, 6-7 μs for ^{15}N and 3.5-4.0 μs for ^{1}H. ^{13}C chemical shifts were referenced to the α-Gly ^{13}CO signal at 176.49 ppm on the TMS scale, and ^{15}N chemical shifts were referenced to the ^{15}N signal of N-acetyl-valine at 122.0 ppm on the liquid ammonia scale.

^{13}C and ^{15}N chemical shifts were measured from two-dimensional ^{13}C-^{13}C and ^{13}C-^{15}N correlation experiments. The ^{13}C-^{13}C 2D experiments used a ^{1}H-driven ^{13}C spin diffusion pulse sequence with 40-60 ms DARR (*4*) mixing periods. The spectra were measured at 273 K under 7-10 kHz MAS. 2D ^{15}N-^{13}C correlation spectra were measured using a REDOR-based pulse sequence for ^{13}C-^{15}N coherence transfer (*5*). The experiments were conducted at 273 K and 243 K under 7-10 kHz MAS. A typical ^{13}C-^{15}N recoupling time of 0.6 ms was used to obtain one-bond ^{15}N-^{13}C cross peaks.

2D ^{15}N-detected ^{1}H spin diffusion experiments were used to detect His37-water cross peaks. The ^{1}H evolution period did not involve homonuclear decoupling, thus only the ^{1}H signals of mobile species such as water and lipids could survive. A short ^{1}H spin diffusion period of 50 μs followed the evolution time to allow water-His37 polarization transfer. A 1 ms ^{1}H-^{15}N Hartman-Hahn cross-polarization (CP) contact time established the ^{15}N magnetization. The spectra were measured at 303 K under 4.0 and 4.5 kHz MAS.

Two-dimensional ^{15}N-^{1}H and ^{13}C-^{1}H dipolar-chemical-shift (DIPSHIFT) correlation experiments (*6*) were used to measure N-H and C-H bond lengths at low temperature and molecular motion at high temperature. For the bond length measurements, the experiments

were carried out under 4.3 or 5.0 kHz MAS at 243 K, at which both the protein backbone and sidechains were frozen. For the dynamics measurements, the DIPSHIFT experiments were carried out at 308 K and 303 K. The indirect dimension of the 2D experiment used either FSLG (*7*) or MREV-8 (*8*) sequences to decouple the ^{1}H-^{1}H dipolar interaction. The t_1 time-domain data were fitted to obtain the apparent couplings, which were then divided by the scaling factor of the homonuclear decoupling sequence, which was 0.577 for FSLG and 0.47 for MREV-8, to obtain the true couplings. For ^{15}N-^{1}H dipolar couplings, the coupling-doubled version of the DIPSHIFT experiment (*9*) was used to enhance the accuracy of the coupling measurement.

To extract motional order parameters from DIPSHIFT data, both the homonuclear decoupling scaling factor and the rigid-limit coupling value contain uncertainties that may affect the order parameter values. To calibrate these effects, we measured the product of the scaling factor and the rigid-limit coupling using the crystalline model peptide formyl-Met-Leu-Phe (f-MLF) (*10*). Based on the theoretical scaling factors of FSLG and MERV-8, we obtained apparent rigid-limit values of 11.3 kHz for N-H and 22.7 kHz for Cα-Hα dipolar couplings. Using these values gave reasonable backbone order parameters of 0.95-1.00 for f-MLF. Therefore, we used these scaling factors and rigid-limit values in extracting His37 order parameters.

Backbone-sidechain distances that constrain the His37 χ_1 and χ_2 torsion angles were measured using ^{13}C{^{15}N} REDOR experiments that selectively irradiate the spins of interest (*11*). The ^{13}C-detected and ^{15}N-dephased experiment is denoted as ^{13}C{^{15}N}) REDOR. The pulse sequence used a selective Gaussian 180° pulse on both the ^{13}C and ^{15}N channels. The control experiment (S_0) did not have further ^{15}N pulses, while the dephasing experiment (S) contained multiple ^{15}N inversion pulses spaced half a rotor period apart. The ^{15}N inversion pulses used the composite pulse 90°180°90° to reduce the effects of pulse imperfection (*12*). For Cα-Nδ1 and Cδ2-Nα distance measurements, the experiments were carried out at 233 K where all sidechain motions were frozen, and MAS frequencies of 5.3, 7.0 and 8.0 kHz were used. The ^{13}C and ^{15}N Gaussian 180°-pulse lengths ranged from 1.125 to 2.0 ms, and the ^{15}N hard 90° pulse length was 7 μs. To characterize imidazole motion at ambient temperature, the

Cγ-Nδ1 dipolar coupling was measured at 303 K under 7 kHz MAS, with a Gaussian 180°-pulse of 2 ms for ^{13}C and 1.14 ms for ^{15}N.

Data Analysis

Simulations of $^{13}C\{^{15}N\}$ REDOR distances to constrain the His37 rotameric structure

Distance fitting for the Cα to sidechain ^{15}N REDOR data took into account 1) the low amount of lipid natural-abundance ^{13}C intensities that overlapped with the His37 Cα peak, and 2) 10% correction for pulse imperfection at long mixing times (*12*). The percent of lipid intensities at the Cα peak was obtained by measuring the minimum S/S_0 ratio of the Cα peak when dephased by its directly bonded amide ^{15}N. The spectra were shown in Figure 2.S2. The percent of lipid intensities was about 30% at both pH 4.5 and pH 8.5.

Selective irradiation of the Nδ1 peak was required for measuring the Cα-Nδ1 distance. For the pH 8.5 sample, the 250-ppm peak is a superposition of 70% Nδ1 of the τ-tautomer and 30% Nε2 of the π-tautomer. However, the Cα-Nε2 distance is almost invariant (4.4 – 4.6 Å) between different rotamers and also much longer than the Cα-Nδ1 distance (3.2 – 3.9 Å). Thus, the Cα-Nδ1 REDOR data was primarily determined by the 70% Cα-Nδ1(τ) distance. The simulated REDOR curves in Figure 2.2A already took into account the 30% presence of the π-tautomer, which contributed a Cα-Nε2 distance of 4.38 Å for χ_2 = 180°, 4.52 Å for χ_2 = -60°, and 4.59 Å for χ_2 = +60°.

For the pH 4.5 sample, the Nδ1 and Nε2 peaks overlap at ~178 ppm (Figure 2.S1A), thus the Cα signal was simultaneously dephased by Nδ1 and Nε2. The REDOR curve fitting thus required a three-spin geometry, with a fixed 25° angle between the Cα-Nδ1 and Cα-Nε2 vectors. The three-spin simulation was carried out in SIMPSON (*13*). For each χ_2, the relative Cα-Nδ1 and Cα-Nε2 distances are fixed. For χ_2 = 180° (*t*), the Cα-Nδ1 distance is 3.9 Å while the Cα-Nε2 distance is 4.4 Å. For χ_2 = -60° (*m*), the Cα-Nδ1 distance is 3.2 Å while the Cα-Nε2 distance is 4.5 Å. For χ_2=+60° (*p*), the Cα-Nδ1 distance is 3.2 Å while the Cα-Nε2 distance is 4.6 Å.

To fit the Cδ2-Nα REDOR data for extracting χ_1, no lipid natural abundance correction was necessary, since the Cδ2 signal did not overlap with any lipid signals. The His37 Nα signal was also well resolved from all other ^{15}N signals.

Extraction of motionally averaged sidechain $^{13}C\{^{15}N\}$ dipolar couplings

At pH 4.5, the high-temperature Cγ-{Nδ1, Nε2} REDOR data was analyzed in a three-spin geometry similar to the low-temperature distance analysis described above. The data mainly reflects the Cγ-Nδ1 order parameter, because the two-bond Cγ-Nε2 dipolar coupling is much weaker, with a rigid-limit value of only 285 Hz. Moreover the Cγ-Nε2 vector is roughly parallel to the Cβ-Cγ motional axis, thus Cγ-Nε2 coupling is insensitive to χ_2 torsional dynamics. Therefore, we held the Cγ-Nε2 coupling fixed at 285 Hz while varying the Cγ-Nδ1 coupling to fit the REDOR data. The resulting Cγ-Nδ1 coupling was 980 Hz, indicating a motional order parameter of 0.85.

In these Cγ-detected REDOR experiments, the S/S_0 values decreased to ~0.4 instead of 0 due to the presence of natural abundance lipid ^{13}C intensities.

Calculation of order parameters for various two-site jump motions

In the motionally averaged tensor (also called the sum tensor) shown in Figure 2.S7A, the three principal axes (red, Σ_i, I = 1, 2, 3) are oriented as follows: one principal axis is along the bisector of the Z_A and Z_B vectors, a second principal axis is perpendicular to the plane of the Z_A and Z_B vectors, and the third principal axis is perpendicular to the other two principal axes. Designating the directional angles between the three averaged principal axes and either bond as Θ_n, the principal values of the motionally averaged tensor are:

$$\bar{\omega}_n = \frac{1}{2}\delta\left(3\cos^2\Theta_n - 1\right) \qquad (1)$$

Once the principal values are obtained, the motionally averaged anisotropy parameter $\bar{\delta}$ is calculated as the difference from the isotropic value of the principal value that is furthest away from the isotropic value. The ratio between the averaged anisotropy parameter and the rigid-limit δ is the order parameter *S*, $S \equiv \bar{\delta}/\delta$.

The relation between the torsional angle change $\Delta\chi$ around a motional axis and the reorientation angle β of a bond is

$$\sin\frac{\beta}{2} = \sin\frac{\Delta\chi}{2}\cdot\sin\theta, \qquad (2)$$

where θ is the angle between the motional axis and the bond of interest. The directional angles are related to β as: $\Theta_{1,2} = 90^\circ - \beta/2$, $\Theta_{2,1} = \beta/2$, and $\Theta_3 = 90^\circ$.

As an example, we consider 180° flips of the imidazole ring around the Cβ-Cγ bond, $\Delta\chi_2 = 180^\circ$. The reorientation angle is then $\beta = 2\theta$, since $\sin\frac{\beta}{2} = \sin 90^\circ \sin\theta = \sin\theta$. For the Cγ-Nδ1 bond, $\theta = 57^\circ$ with respect to the Cβ-Cγ bond, so $\beta = 114^\circ$. As a result, $\Theta_1 = 33^\circ$, $\Theta_2 = 57^\circ$, and $\Theta_3 = 90^\circ$. The motionally averaged principal values are thus:

$$\begin{aligned}
\bar{\omega}_1 &= \tfrac{1}{2}\delta\left(3\cos^2 33^\circ - 1\right) = 0.56\delta \\
\bar{\omega}_2 &= \tfrac{1}{2}\delta\left(3\cos^2 57^\circ - 1\right) = -0.06\delta, \\
\bar{\omega}_3 &= \tfrac{1}{2}\delta\left(3\cos^2 90^\circ - 1\right) = -0.5\delta
\end{aligned} \qquad (3)$$

The motionally averaged anisotropy parameter is $\bar{\delta} = \bar{\omega}_1 = 0.56\delta$, which gives a Cγ-Nδ1 order parameter of $S_{CN} \equiv \bar{\delta}/\delta = 0.56$ for 180° ring flips.

For 180° χ_1 angle changes around the Cα-Cβ axis while χ_2 is fixed at 180°, since the Cγ-Nδ1 bond is only 8.2° from the Cα-Cβ bond, $\beta = 16^\circ$. Thus the motionally averaged principal values are $\bar{\omega}_1 = 0.97\delta$, $\bar{\omega}_2 = -0.47\delta$, and $\bar{\omega}_3 = -0.5\delta$. This means the Cγ-Nδ1 order parameter is 0.97 for 180° χ_1 changes, which is much higher than the measured order parameter of 0.85. Figure 2.S7 similarly shows that no χ_1 change can satisfy the measured Cδ2-Hδ2 order parameter of 0.80. Therefore, the experimentally measured order parameters rule out χ_1 changes as a possible motional mechanism.

Proposed model of ring-flip assisted proton conduction by M2

Liposome assays (*14*) showed that the M2 proton conductance increased by ~14 fold from 18˚C to 37˚C. This temperature dependence indicates that the total energy barrier for proton conductance is ~104 kJ/mol:

$$\frac{G_{H+,310K}}{G_{H+,291\,K}} = e^{\frac{-E_{a,}}{R}\cdot(\frac{1}{310}-\frac{1}{291})} \approx 14 \quad \Rightarrow E_a \approx 104\ \ kJ/mol\,. \qquad (4)$$

This energy barrier is consistent with the barrier for histidine sidechain motion (> 59 kJ/mol) obtained from NMR dipolar couplings at pH 4.5 to 6. But it does not agree with the calculated energy barrier (29-42 kJ/mol) for proton hopping through the charged His37 tetrad, which is the rate-limiting step in the shutter model. Thus, the similar temperature dependences of proton conductivity and His37 sidechain motion suggest the shuttle model for proton conduction by M2. Specifically, we propose that proton conduction is achieved by His37 ring-flip-mediated proton dissociation and association. Below we qualitatively outline the energetic aspects of this model.

The imidazolium reorientation rate observed by NMR dipolar couplings is on the order of $5\times10^4\ s^{-1}$ (Figure 2.S8). On the other hand, the value of single-channel proton conductance of M2 has significant uncertainty and varies with the experimental method and condition. In two recent authoritative studies, one study concluded a single-channel current of ~0.5 fA at pH 6.2 (*15*), while the other study measured a value of 2.7 aA at 18°C and pH 5.7 (*14*). Based on the unitary current of the first study, a proton dissociation rate constant, k_{H+}, of $\sim1.7\times10^4\ s^{-1}$ was obtained (*15*), which is very close to the imidazolium ring flip rate. Since a basic unit of the proton conduction cycle (Figure 2.4E) includes both ring motions and the proton transfer reaction, the similarity of k_{H+} and the sidechain motional rate means that proton transfer is extremely fast, with a negligible energy barrier.

The second study reported much lower conductance values (*14*), which at 37˚C were about 250 H^+/s per channel (*14*). Since at pH 5.7 the number of imidazoliums per channel is about 3 (*16*), the conductance per imidazolium is $k_{H+} \approx 250/3 = 83/s$. This rate constant is 100-1000 times smaller than the ring-flip rate, which suggests that the proton transfer

reaction may be much slower than in the first estimate above. Based on the Arrhenius equation, the ratio of 100-1000 translates to an energy barrier of 12-18 kJ/mol for proton transfer, which is still much lower than the barrier of imidazolium motion. Thus, even using the lower limit of proton conductance functional data, the highest energy barrier of proton conduction is still the barrier for imidazolium motion.

This ring-motion-assisted proton transfer model is consistent with the observed deuterium isotope effect of M2 (*15*), where H^+ are conducted 1.8 – 2.5 times faster than D^+ by M2. This ratio is significantly larger than if water diffusion is the mechanism (predicted ratio = 1.25), and also larger than if the H^+ and D^+ mobility in the respective solvent (H_2O and D_2O) is the mechanism (predicted ratio = 1.4-1.5) (*17*). Instead, the magnitude of the isotope effect suggests proton dissociation in a mixed hydrogen-bonded chain with dissimilar elements, which supports the current model. The 2-fold difference in H^+ and D^+ conductance may be explained by an increased energy barrier of ~1.7 kJ/mol for D^+ dissociation than H^+ dissociation.

Analysis of Cε1-Hε1 bond length from low-temperature dipolar couplings

To obtain the His37 Cε1-Hε1 bond length at low temperature, we considered the contribution of lipid intensities to the Cε1 peak at 134 ppm. The sphingomyelin C5 peak resonates at 134 ppm and at 243 K cannot be resolved from the Cε1 peak (*18*). Based on the protein/lipid molar ratio and the 1.1% natural abundance of ^{13}C, this SPM C5 intensity is only 6% of the labeled Cε1 peak intensity. Approximating that the SPM C5 peak has comparable C-H dipolar coupling as the main lipid CH_2 peak at 32 ppm, we obtained the CH_2 coupling strength, and used it to simulate the expected SPM C5-H dipolar dephasing curve. We then fitted the total intensities including the lipid effect according to the relative intensities of the two spins. The resulting C-H bond length is 1.20 Å for the pH 8.5 sample and 1.19 Å for the pH 4.5 sample, which are within ±0.02 Å of the values without the lipid natural abundance correction (Figure 2.4B).

These Cε1-Hε1 bond lengths are unusually long (weak dipolar couplings). Due to the high signal/noise ratio, where the error bars are smaller than the data symbols in Figure 2.4B, the random uncertainties were at most ±0.4 kHz in the dipolar couplings or ±0.02 Å in the

distances. There are three possible sources of systematic uncertainty: 1) uncertainty in the ^{1}H homonuclear decoupling scaling factor, 2) residual motion, and 3) the contribution of lipid natural abundance signals (discussed above). The first two sources were internally calibrated and largely excluded by the Cδ2-Hδ2 coupling measured in the same experiment, at the same temperature and under identical homonuclear decoupling. The Cδ2-Hδ2 coupling reached the rigid limit of 23.9 kHz, indicating the absence of motion and an unstretched bond length of 1.08 Å. Thus, the homonuclear decoupling scaling factor did not bias the couplings to smaller values. The possibility of long-range effects from protons in the rest of the imidazole ring can also be ruled out because additional protons can only increase the coupling, not decrease it. Therefore, the weak Cε1-Hε1 coupling at both pH values cannot be attributed to experimental uncertainty, and can only be attributed to bond stretching.

N-H bond lengths in hydrogen-bonded imidazole model compounds have been measured by McDermott and coworkers and found to be stretched from 1.01 Å to as long as 1.07 Å (*19*). For O-H…O systems, much longer O-H bond stretching by as much as 0.3 Å was known. In comparison, C-H bond stretching in hydrogen bonds has been much less explored. The weak coupling may be due to proton hopping or partial occupancy of the proton at Cε1, or due to true stretching of the covalent bond that results from an altered potential well for Hε1. The former scenario is unlikely because we did not observe any temperature dependence of the ^{13}C and ^{15}N chemical shifts, which would be expected for proton hopping. Therefore, the most reasonable interpretation of the weak Cε1-Hε1 dipolar coupling is stretching of the covalent bond by hydrogen bonding. Indeed, a recent *ab initio* study of various types of hydrogen bonding in aromatic amino acids, including Phe, Tyr, Trp and His, found that the Cε1-H bond of imidazole rings experience the strongest C-H…O hydrogen bonding and the largest bond elongation (*20*). This effect was attributed to the acid nature of the Cε1-H group between two nitrogens. Thus, the computation result was qualitatively consistent with the observed bond stretching here. The exact magnitude of the Cε1 bond stretching awaits future investigation and experimental confirmation.

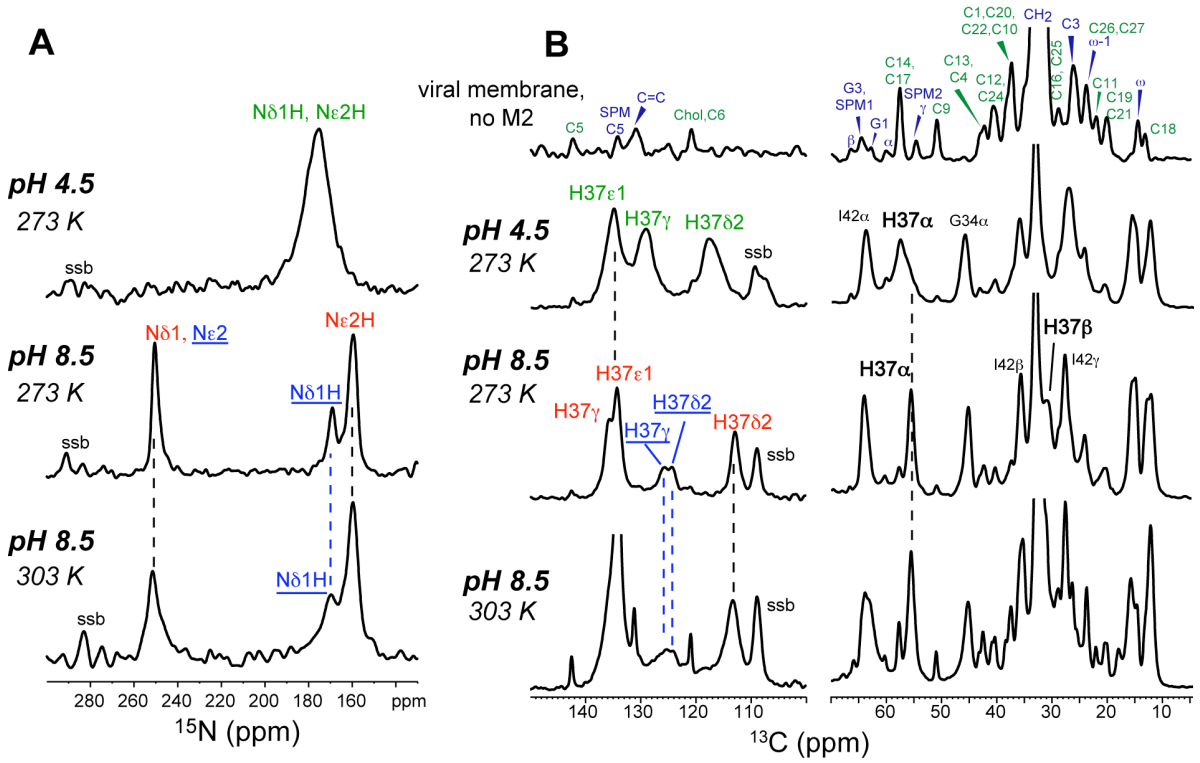

Figure 2.S1. 1D ^{13}C and ^{15}N MAS spectra of His37-labeled M2TM at pH 8.5 and 4.5 at indicated temperatures. (A) ^{15}N CP-MAS spectra. The ^{1}H-^{15}N CP contact time was 3 ms at 273 K and 1.5 ms at 303 K. The CP matching condition was optimized using ^{15}N-tBoc-proline to ensure maximal transfer of the ^{1}H magnetization to unprotonated ^{15}N. Thus, the lack of ~250 ppm ^{15}N peak in the pH 4.5 spectrum indicates virtually no (≤5%) neutral imidazoles at pH 4.5, which translates to a fourth pKa of ~ 4.7 for the His37 tetrad, consistent with previous estimates in model membranes (*16*). At pH 8.5, the π-tautomer signals were resolved from the τ-tautomer signals at both 273 K and 303 K, indicating no exchange between the two tautomers. The imidazole peaks were assigned in red for the neutral τ-tautomer, in blue for the neutral π-tautomer, and in green for the charged histidine. (B) ^{13}C CP-MAS spectra of the virus-mimetic lipid membrane without the protein (top), the membrane-bound M2TM at pH 4.5 at 273 K, and at pH 8.5 at 273 K and 303 K. In the lipid-only spectrum, blue designates sphingomyelin (SPM), DPPC and DPPE peaks, and green denotes cholesterol peaks (*1*). The two neutral tautomers were observed at both temperatures in the pH 8.5 spectra, confirming slow or no exchange.

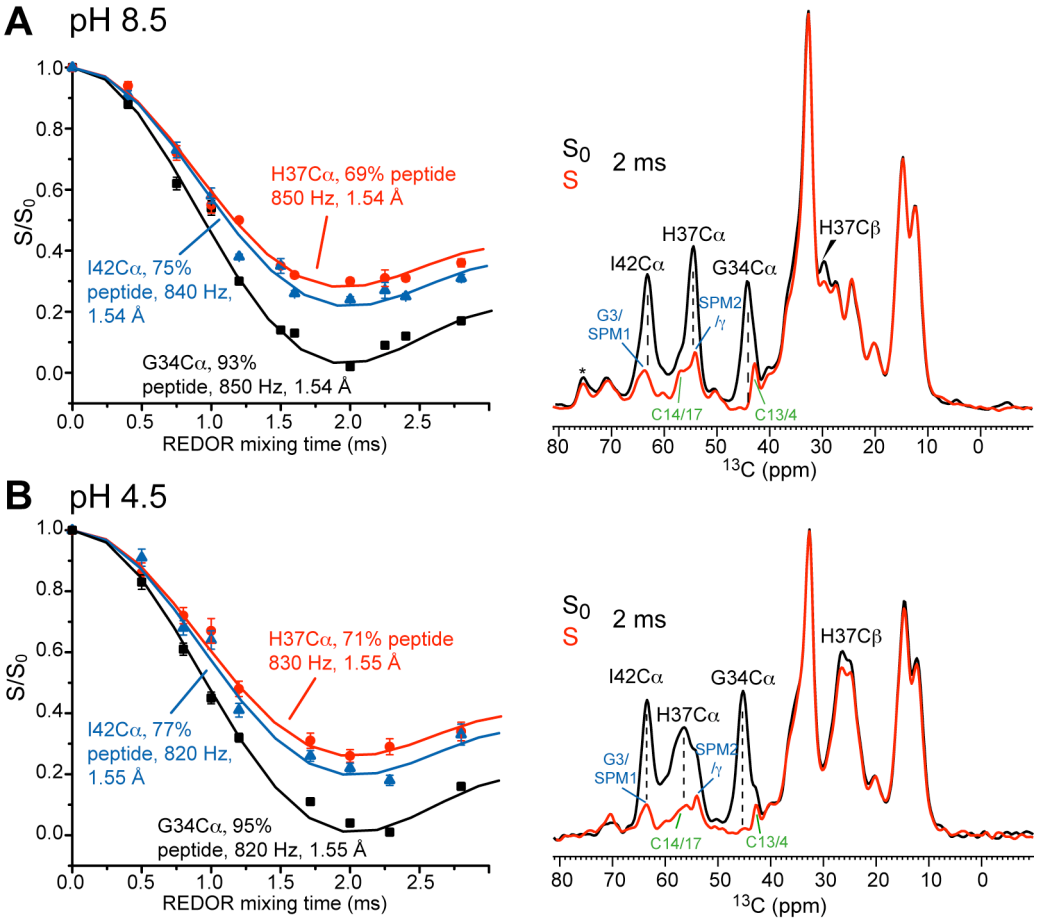

Figure 2.S2. One-bond Cα–Nα REDOR data of M2TM to determine the percentage of lipid ^{13}C intensities that overlaps with the His37 Cα peak. This information was necessary for quantifying the Cα–Nδ1 distance in Figure 2.2 to determine the χ_2 torsion angle. The experiment did not involve frequency-selective ^{15}N irradiation since sidechain nitrogens are too far from Cα to affect the one-bond dipolar coupling. (A) pH 8.5. (B) pH 4.5. All REDOR curves show rigid-limit Cα-Nα dipolar couplings consistent with the bond length, which is expected for the protein at the experimental temperature of 233 K. The minimum S/S_0 value indicates the amount of lipid natural abundance ^{13}C intensities that overlap with the protein Cα peaks. Representative REDOR control (S_0, black) and dephased (S, black) spectra are shown on the right. The lipid peaks are labeled in green for cholesterol and blue for SPM, DPPC and DPPE. The REDOR experiments were carried out at several spinning speeds (5-8 kHz for pH 8.5 and 4-7 kHz for pH 4.5) in order to densely sample the mixing times.

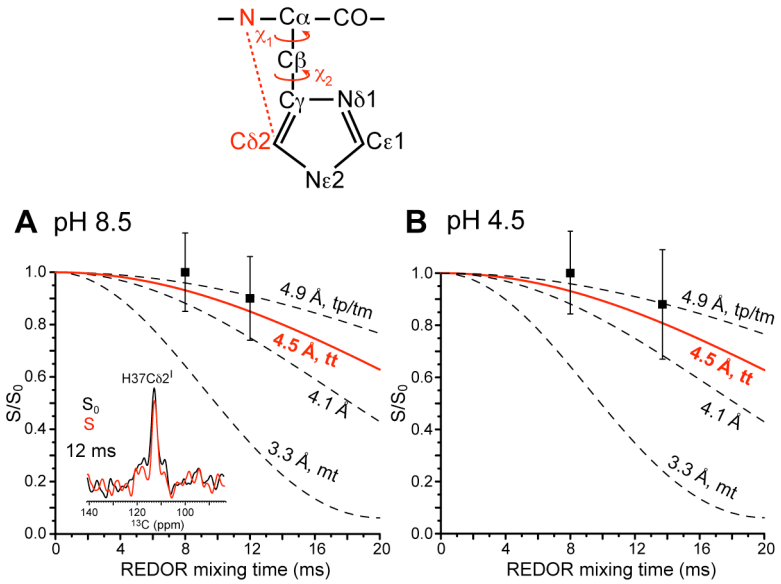

Figure 2.S3. Cδ2-Nα REDOR distance data to constrain the His37 rotameric conformation. Representative $^{13}C\{^{15}N\}$ selective REDOR spectra are shown. S_0: control spectrum (black). S: dephased spectrum (red). (A) pH 8.5. (B) pH 4.5. Both samples exhibit Cδ2-Nα distances of 4.5 – 4.9 Å, indicating that the χ_1 angle is 180° (*t*), given the χ_2 angle of 180° obtained from Cα-Nδ1 distances (Figure 2.2). A χ_1 of -60° combined with a χ_2 of 180° would give a much shorter distance (3.3 Å) that is inconsistent with the data. The χ_1=+60° rotamer is not allowed in α-helices due to steric conflict with the backbone (*21*). Rotamer notations: *t*: 180°, *p*: +60°, and *m*: -60°. The REDOR experiments were carried out at 233 K under 7-8 kHz MAS.

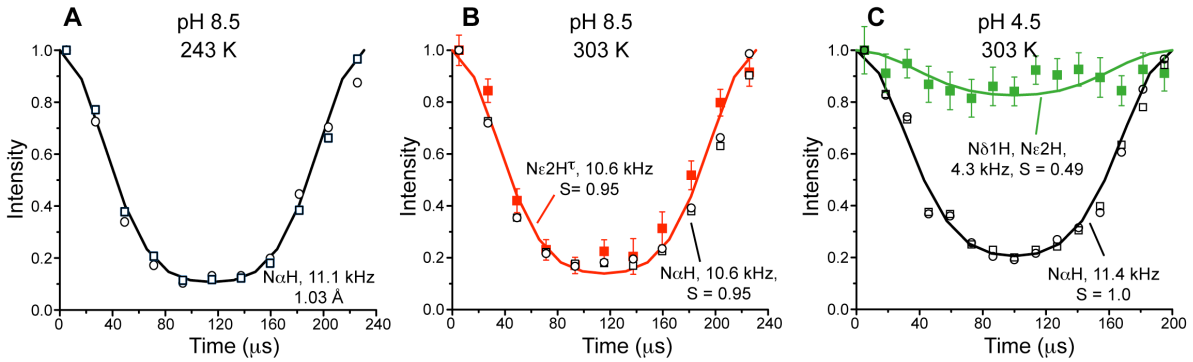

Figure 2.S4. ^{15}N-^{1}H dipolar couplings of His37 in M2TM to determine bond lengths at low temperature and sidechain dynamics at high temperature. (A) 243 K N-H coupling of backbone amide at pH 8.5 corresponds to a bond length of 1.03 Å. (B) 303 K N-H dipolar couplings at pH 8.5. Both the backbone amide and the sidechain Nε2(τ) show close to rigid-limit couplings. The former confirms immobilization of the M2 backbone by the viral membrane at physiological temperature, while the latter indicates the absence of sidechain motion in the closed channel at physiological temperature. (C) 303 K N-H dipolar couplings at pH 4.5. The backbone Nα-Hα coupling remains in the rigid limit, while the sidechain Nδ1 and Nε2 exhibit much weaker N-H couplings, indicating sidechain motion. The order parameter of 0.49 was obtained by dividing the measured coupling with the low-temperature value of 8.8 kHz (Figure 2.4A). This low order parameter results from the combined effect of sidechain motion and hydrogen exchange between NH and water protons. The DIPSHIFT experiments were carried out under 4.3 kHz MAS for the pH 8.5 sample and 5 kHz MAS for the pH 4.5 sample.

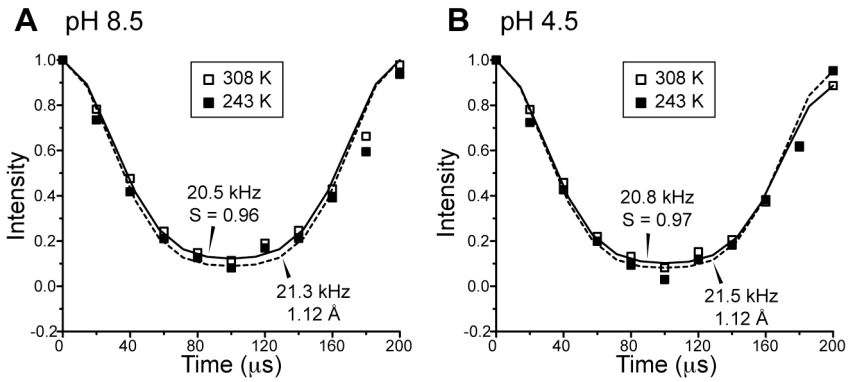

Figure 2.S5. His37 Cα-Hα dipolar couplings at 308 K confirm immobilization of the M2 backbone in the cholesterol-containing viral membrane at physiological temperature. (A) pH 8.5. (B) pH 4.5. The 308 K couplings approach the rigid limit and are close to the low-temperature (243 K) values at both pH. The experiments were carried out under 5 kHz MAS.

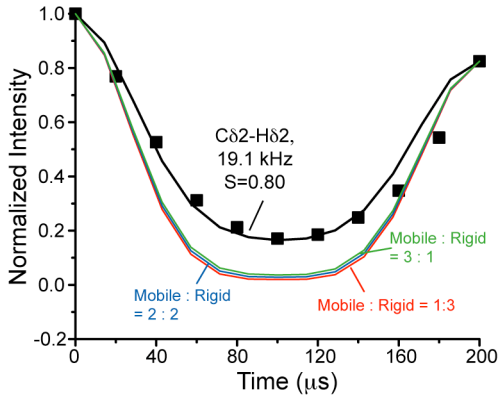

Figure 2.S6. Predicted dipolar couplings and order parameters for heterogeneous His37 sidechain motion. Calculated Cδ2-Hδ2 dipolar couplings are shown for cases where one to three imidazoliums in each channel undergoes 180° ring flips while the others are immobilized. The calculated dephasing curves are all much lower than the experimental data, thus ruling out heterogeneous ring flips. The mobile : immobile ratios are 3:1 for the green curve, 2:2 for the blue curve, and 1:3 for the red curve.

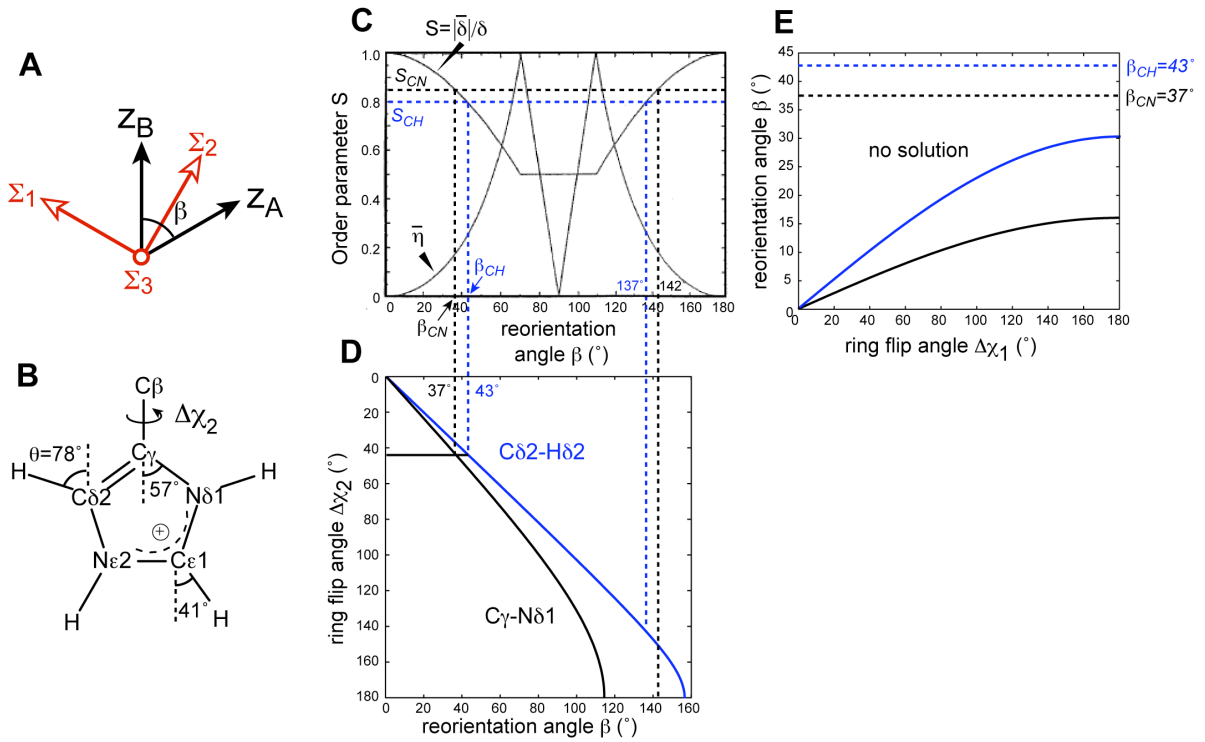

Figure 2.S7. Calculation of order parameters for two-site jumps of imidazolium rings at low pH. (A) General geometry of two-site jumps, where a bond reorients by an angle β between Z_A and Z_B. The orientations of the averaged principal axis system (Σ_1, Σ_2, Σ_3) are indicated in red. (B) Geometry of the imidazolium, where the angles θ between several bonds and the Cβ-Cγ axis are indicated. (C) Dependence of the motional order parameter $S=|\bar{\delta}|/\delta$ on the reorientation angle β for two-site jumps, adapted from (*22*). The measured order parameter values for Cγ-Nδ1 (0.85) and Cδ2-Hδ2 (0.80) bonds are indicated as dashed lines. Two β solutions, centered at 40° and 140°, are found. (D) Relation between the reorientation angle β and the ring flip angle $\Delta\chi_2$. Both Cδ2-Hδ2 and Cγ-Nδ1 order parameters are satisfied only at a single $\Delta\chi_2$ of ~45°. The other β solution of 140° cannot be satisfied because no χ_2 changes can reorient the Cγ-Nδ1 bond by more than 114°. (E) Relation between β and χ_1 changes. No χ_1 changes can satisfy the experimental constraint of β= 40° or 140°, since both Cγ-Nδ1 and Cδ2-Hδ2 bonds are approximately parallel to the Cα-Cβ bond under a trans χ_2 angle. In other words, ring reorientation around the Cα-Cβ bond will cause little changes in the Cγ-Nδ1 and Cδ2-Hδ2 bond orientations, and thus will cause very little reduction of these couplings.

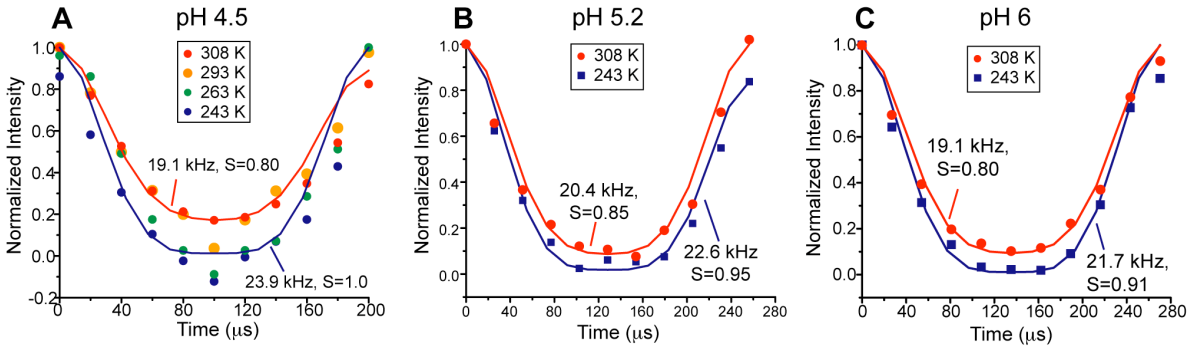

Figure 2.S8. His37 sidechain motion at pH 4.5, pH 5.2 and pH 6.0 at physiological temperature. Cδ2-Hδ2 dipolar coupling was measured at 243 K to confirm the rigid limit and at 308 K to obtain dynamics information. (A) pH 4.5 data at 308 K, 293 K, 263 K, and 243 K. The coupling was scaled by an order parameter of 0.80 at both 308 K and 293 K, indicating that the imidazolium motion was in the fast limit. At 263 K the coupling reached the rigid limit, indicating the ring motion was frozen. At 273 K an intermediate order parameter of 0.92 was found (not shown). (B) pH 5.2 data at 308 K and 243 K, extracted from the charged Cδ2 chemical shift of 117.6 ppm. (C) pH 6.0 data at 308 K and 243 K, extracted from the neutral Cδ2 chemical shift of 113 ppm. For both pH 5.2 and pH 6, the high-temperature order parameters are similar to what is measured at pH 4.5, thus His37 sidechain motion occurs not only at pH 4.5 but also at the physiological pH of the virus. The similar sidechain mobility in the less charged His37 tetrad at pH 6 also suggests that motion is an intrinsic property of a spacious conducting channel, rather than a direct function of the charged state of His37.

For a motional process to cause fast averaging of an interaction, the motional rate has to be significantly larger than the coupling of interest. Likewise, for a slow motion to not induce intermediate-timescale line broadening, the motional rate k must be significantly smaller than the coupling of interest. For an FSLG-scaled ^{13}C-^{1}H rigid-limit coupling of ~13 kHz, we used a factor of 4 for the lower-bound and upper bound, thus giving $R_{flip,293\ K} \geq 52\ kHz$ and $R_{flip,263\ K} \leq 3.3\ kHz$. Thus, at pH 4.5, the lower limit of the activation energy of the motion is:

$$\frac{R_{flip,293\ K}}{R_{flip,263\ K}} = e^{-\frac{E_a}{R}\left(\frac{1}{293}-\frac{1}{263}\right)} \geq 16 \Rightarrow E_a \geq 59\ kJ/mol$$

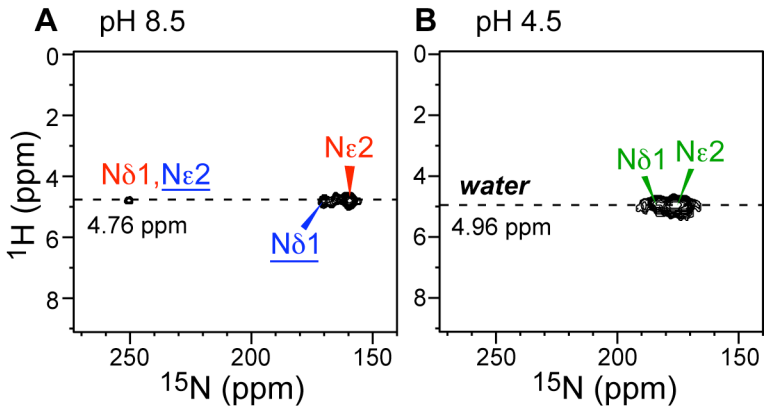

Figure 2.S9. 2D water-His37 ^{1}H-^{15}N correlation spectra of M2TM in viral membranes. (A) pH 8.5. (B) pH 4.5. The spectra were measured at 303 K under 4.5 and 4.0 kHz MAS. A 1 ms ^{1}H-^{15}N HH-CP contact time and a 50 μs ^{1}H spin diffusion mixing time were used to transfer the water polarization to His37. Since the ^{1}H-^{1}H homonuclear dipolar coupling is scaled by -0.5 during HH-CP, the total effective ^{1}H spin diffusion mixing time was 0.55 ms, which was much shorter than the length of 4 ms used to show the near absence of water-G34 cross peak in amantadine-bound and dehydrated M2TM channels (*18*). Thus, the presence of imidazole-water cross peaks at both pH indicates the presence of water near His37. In particular, at high pH, a weak water cross peak with the unprotonated Nδ1 was detected, indicating that the C-terminus of His37 was not completely devoid of water.

Table 2.S1. Full widths at half maximum (ppm) of His37 sidechains at pH 8.5 and pH 4.5, measured at 273 K [a].

Site	pH 8.5	pH 4.5
Cγ	2.5	3.0
Cδ2	2.0	4.0
Nδ1	3.5[b]	8.4
Nε2	5.4[b]	7.0

[a]. The linewidths were obtained from resolved peaks in 1D or 2D spectra, with identical line broadening parameters of LB = -15 and GB = 0.04.

[b]. These linewidths refer to the major τ-tautomer.

Table 2.S2. Bond order parameters for different motional models of the imidazole ring around the Cβ-Cγ bond.

Bonds	S_{exp}	180° ring flip		45° ring flip		Uniaxial rotation	
		β	S	β	S	Cone angle	S
Cγ-Nδ1	0.85	114°	0.56	37°	0.85	57°	-0.06
Cδ2-Hδ2	0.80	156°	0.94	43°	0.80	78°	-0.44
Cε1-Hε1	0.95	82°	0.50	28°	0.91	41°	0.35

References

1. W. Luo, S. D. Cady, M. Hong, *Biochemistry* **48**, 6361 (2009).
2. S. D. Cady, M. Hong, *J. Biomol. NMR* **45**, 185 (2009).
3. S. D. Cady, M. Hong, *Proc. Natl. Acad. Sci. USA* **105**, 1483 (2008).
4. K. Takegoshi, S. Nakamura, T. Terao, *Chem. Phys. Lett.* **344**, 631 (2001).
5. M. Hong, R. G. Griffin, *J. Am. Chem. Soc.* **120**, 7113 (1998).
6. M. G. Munowitz, R. G. Griffin, G. Bodenhausen, T. H. Huang, *J. Am. Chem. Soc.* **103**, 2529 (1981).
7. A. Bielecki, A. C. Kolbert, M. H. Levitt, *Chem. Phys. Lett.* **155**, 341 (1989).
8. W.-K. Rhim, D. D. Elleman, R. W. Vaughan, *J. Chem. Phys.* **59**, 3740 (1973).
9. M. Hong *et al.*, *J. Magn. Reson.* **129**, 85 (1997).
10. C. M. Rienstra *et al.*, *Proc. Natl. Acad. Sci. USA* **99**, 10260 (2002).
11. C. P. Jaroniec, B. A. Tounge, J. Herzfeld, R. G. Griffin, *J. Am. Chem. Soc.* **123**, 3507 (2001).
12. N. Sinha, K. Schmidt-Rohr, M. Hong, *J. Magn. Reson.* **168**, 358 (2004).
13. M. Bak, T. Rasmussen, N. C. Nielsen, *J. Magn. Reson.* **147**, 296 (2000).
14. T. I. Lin, C. Schroeder, *J. Virol.* **75**, 3647 (2001).
15. J. A. Mould *et al.*, *J. Biol. Chem.* **275**, 8592 (2000).
16. J. Hu *et al.*, *Proc. Natl. Acad. Sci. USA* **103**, 6865 (2006).
17. T. E. DeCoursey, V. V. Cherny, *J. Gen. Physiol.* **109**, 415 (1997).
18. W. Luo, M. Hong, *J. Am. Chem. Soc.* **132**, 2378 (2010).
19. X. J. Song, C. M. Rienstra, A. E. McDermott, *Magn. Reson. Chem.* **39**, S30 (2001).
20. S. Scheiner, T. Kar, J. Pattanayak, *J. Am. Chem. Soc.* **124**, 13257 (2002).
21. S. C. Lovell, J. M. Word, J. S. Richardson, D. C. Richardson, *Proteins: Struct., Funct., Genet.* **40**, (2000).
22. K. Schmidt-Rohr, H. W. Spiess, *Multidimensional Solid-State NMR and Polymers*. (Academic Press, San Diego, 1994), pp. 478.

Chapter 3

Conformational Plasticity of the Influenza A M2 Transmembrane Helix in Lipid Bilayers under Varying pH, Drug Binding and Membrane Thickness

A paper published in Biochimica et Biophysica Acta - Biomembranes

2011, vol. 1808 pp. 415-423

Fanghao Hu, Wenbin Luo, Sarah D. Cady and Mei Hong

Abstract

Membrane proteins change their conformations to respond to environmental cues, thus conformational plasticity is important for function. The influenza A M2 protein forms an acid-activated proton channel important for the virus lifecycle. Here we have used solid-state NMR spectroscopy to examine the conformational plasticity of membrane-bound transmembrane domain of M2 (M2TM). ^{13}C and ^{15}N chemical shifts indicate coupled conformational changes of several pore-facing residues due to changes in bilayer thickness, drug binding and pH. The structural changes are attributed to the formation of a well-defined helical kink at G34 in the drug-bound state and in thick lipid bilayers, non-ideal backbone conformation of the secondary-gate residue V27 in the presence of drug, and non-ideal conformation of the proton-sensing residue H37 at high pH. The chemical shifts constrained the (ϕ, ψ) torsion angles for three "basis" states, the equilibrium among which explains the multiple resonances per site in the NMR spectra under different combinations of bilayer thickness, drug binding and pH conditions. Thus, conformational plasticity is important for the proton conduction and inhibition of M2TM. The study illustrates the utility of NMR chemical shifts for probing the structural plasticity and folding of membrane proteins.

Introduction

Membrane proteins carry out their functions by changing their structures under specific environmental cues. They can switch between active and inactive functional states by ion concentration changes [1], ligand binding [2], exposure to hydrophobic lipid bilayers [3-5], and changes in mechanical pressure [6, 7]. Oligomeric membrane proteins are particularly malleable to environmental influences [8], since the monomers are held together

by weak non-covalent interactions that are susceptible not only to chemical changes but also to physical changes such as the membrane fluidity and thickness. An increasing body of literature suggests that oligomeric membrane proteins may be predisposed to conformational changes by significant conformational distributions due to a rough potential energy surface (9, 10).

The M2 protein of influenza A viruses presents a particularly interesting and complex example of how membrane protein conformations depend on the environment. The M2 protein forms a pH-gated tetrameric proton channel in the virus envelope that is important for virus replication [11, 12]. Opened by acidic pH of the endosome that encapsulates the virus after its endocytosis, the M2 protein initiates the release of the viral ribonucleoprotein complex into the host cell. The M2 protein is inhibited by the antiviral drug amantadine at a stoichiometric ratio of one drug per channel [13]. The membrane-spanning helix of the M2 protein contains the pH-sensing [14], gating [15], and amantadine-binding residues [16], and is thus the functional core of the protein [17]. High-resolution structures of the M2 transmembrane domain (M2TM) complexed with amantadine have been determined at low pH using X-ray crystallography [18] and at high pH by solid-state NMR [16]. The structure of a longer construct of the M2 protein containing the transmembrane domain was also reported [19]. While these structures gave rich insights into the inhibition and proton conduction mechanisms of M2, they represent only snapshots of the protein structure under the specific conditions of the experiments and do not fully capture the conformational changes and plasticity of the protein. Indeed, significant variations among the three structures exist: for example, the helix orientations and the sidechain conformations of the essential proton-selective and channel-gating residues differed, suggesting the environmental dependence of M2TM structure.

The conformational plasticity of membrane-bound M2TM under a range of experimental conditions has been documented by Cross and coworkers based on ^{15}N solid-state NMR (SSNMR) experiments on oriented membranes [20]. These static ^{15}N NMR spectra report the peptide orientation relative to the bilayer normal, thus frequency and linewidth changes indicate changes of the helix orientations and orientation distribution. It was found that solvents used to reconstitute M2TM into lipid bilayers, amantadine, and pH

all affected the helix orientation [20]. Complementarily, magic-angle-spinning (MAS) ^{13}C and ^{15}N NMR spectra [21, 22] are sensitive to both the backbone conformation and the helix orientation. MAS spectra of M2TM in unoriented liposomes showed that the helix orientation was influenced by the membrane thickness [23], consistent with EPR results [24]. Moreover, the helical bundle dynamics was found to be extremely sensitive to the membrane composition and fluidity [22]. In addition, the stability of M2TM tetramers in detergent micelles and lipid bilayers have been extensively characterized using analytical ultracentrifugation experiments [25, 26].

The purpose of the present study is two-fold. First, we extend the previous work by a comprehensive investigation of the effects of membrane thickness, drug binding and pH on the backbone conformation of a large number of residues in M2TM. The conformational changes were detected through ^{13}C and ^{15}N isotropic chemical shifts obtained from 2D MAS-NMR correlation spectra. We measured the chemical shifts of the contiguous stretch of residues from L26 to L38, and identified significant chemical shift changes at V27, S31, G34 and H37, which are pore-lining residues essential for drug inhibition and proton conduction [27, 28]. While the chemical shift behavior of V27, S31 and G34 under a subset of these conditions has been reported before [21, 22], they have not been systematically examined and compared. The H37 ^{13}C chemical shifts are entirely new and give information on the pH activation of the channel. These chemical shifts yield several new insights into the nature of the conformational changes of M2TM: 1) the conformational changes are coupled among many residues; 2) different environmental factors may exert the same or opposite effects on the protein structure; and 3) the environmental parameters shift the protein conformational equilibrium among a small number of distinct states, so that more than one conformation usually exists under a certain condition. Based on the NMR chemical shifts, we obtained the backbone torsion angles of M2TM in three "basis" states, which correspond to the drug-bound protein at high pH in thick lipid bilayers, the drug-free protein at high pH in thin lipid bilayers, and the low-pH apo protein in thick lipid bilayers.

Materials and Methods

Membrane sample preparation

M2TM corresponding to the Udorn strain of influenza A virus (residues 22–46, SSDPLVVAASII GILHLILWILDRL) was synthesized using Fmoc chemistry by PrimmBiotech (Cambridge, MA) and purified to >95% purity. Several samples containing uniformly ^{13}C, ^{15}N-labeled residues from Leu26 to Leu38, Ile42 and Asp44 were used.

The lipid membranes used to reconstitute M2TM include DLPC (12:0) bilayers, DMPC (14:0) bilayers, and a mixed membrane that mimics the virus-envelope lipid composition [22]. The mixed membrane includes egg sphingomyelin (SM), DPPC, DPPE and cholesterol (Chol) at a molar ratio of 28% : 21% : 21% : 30%. For the viral membrane mixture, SM was first dissolved in chloroform/methanol (10 : 2) solution, then mixed with the other lipids and cholesterol in chloroform to the desired molar ratio. All membranes were lyophilized and then dissolved in a buffer of suitable pH, vortexed, and freeze-thawed several times to form large unilamellar vesicles. We used a pH 4.5 citrate buffer, a pH 7.5 phosphate buffer, and a pH 8.5 Tris buffer, for the various samples.

M2TM was reconstituted into the lipid membranes by detergent dialysis as described before [22, 29]. The peptide : lipid molar ratios were 1: 15 – 1 : 12. The proteoliposomes were centrifuged at 150,000 g to obtain membrane pellets, which were then packed into 4 mm MAS rotors for NMR experiments. Photometric assay showed >95% binding of the peptide. For drug-bound samples, amantadine hydrochloride or 3-azaspiro[5,5]undecane hydrochloride was dissolved in buffer and directly titrated into the membrane.

Solid-state NMR experiments

Solid-state NMR experiments were carried out on a 400 MHz (9.4 Tesla) and a 600 MHz (14.1 Tesla) Bruker spectrometer using 4 mm MAS probes. Spectra of most viral membrane samples were measured near 303 K, while spectra of DLPC and DMPC-bound protein samples were measured at 243 K to freeze M2TM motion [23, 30]. 2D ^{13}C-^{13}C DARR [31] correlation spectra were measured under 5 and 7 kHz MAS with a spin diffusion mixing time of 20 or 40 ms. 2D ^{15}N-^{13}C correlation spectra were measured under 7 kHz MAS using a REDOR sequence with 0.7 ms of ^{13}C-^{15}N coherence transfer [32]. Typical radio-frequency fields were 50 kHz for ^{13}C and ^{15}N and 60-70 kHz for ^{1}H. ^{13}C and ^{15}N chemical shifts were referenced to the α-Gly CO signal at 176.49 ppm on the TMS scale and the ^{15}N signal of N-

acetyl-valine at 122 ppm on the liquid ammonia scale, respectively. After adjusting the ^{13}C chemical shifts to be referenced with respect to DSS (1.7 ppm larger values than the TMS-referenced chemical shifts [33]), we inputted the measured ^{13}C and ^{15}N isotropic shifts into TALOS+ [34] to obtain the backbone (ϕ, ψ) torsion angles. These torsion angles were used to generate the helix conformational models in Figure 3.6.

Results

Effects of membrane thickness, amantadine, and pH on chemical shifts

To examine how membrane thickness, drug, and pH affect the conformation of individual residues, we measured the ^{13}C and ^{15}N chemical shifts using 2D ^{13}C-^{13}C and ^{15}N-^{13}C correlation experiments. We first compared the M2TM spectra in three lipid bilayers: DLPC with 12 carbons per acyl chain, DMPC with 14 carbons per chain, and a cholesterol- and SM-containing virus-mimetic membrane with 16 or 18 carbons per chain. Figure 3.1A-C shows regions of the 2D ^{13}C-^{13}C and ^{15}N-^{13}C spectra of M2TM at pH 7.5 without amantadine. The DLPC and DMPC samples were measured at low temperature (243 K) to freeze the backbone motion [23, 30] while the viral-membrane samples were measured at 303 K since the backbone is already immobilized at ambient temperature [22]. L26, A29 and A30 exhibited a single set of chemical shifts independent of the membrane thickness. In contrast, two sets of chemical shifts with varying intensity ratios were observed for G34. We denote the set of peaks with larger ^{13}CO and ^{15}N chemical shifts as state 1, and the set of peaks with smaller ^{13}CO and ^{15}N chemical shifts as state 2. Peak area integration showed that the relative amounts of states 1 and 2 differed in the three membranes. In the thinnest membrane, DLPC, the percentage of state 1 was about ~25% of the total intensity. As the membrane thickness increased, the state-1 peak intensities increased. In DMPC membranes, state 1 accounted for ~56% of the total intensities, while in the thickest viral membrane, state 1 represented ~67% of the total population. V27 also showed bimodal conformational distribution, although the relative amounts of the two conformations varied less significantly with membrane thickness.

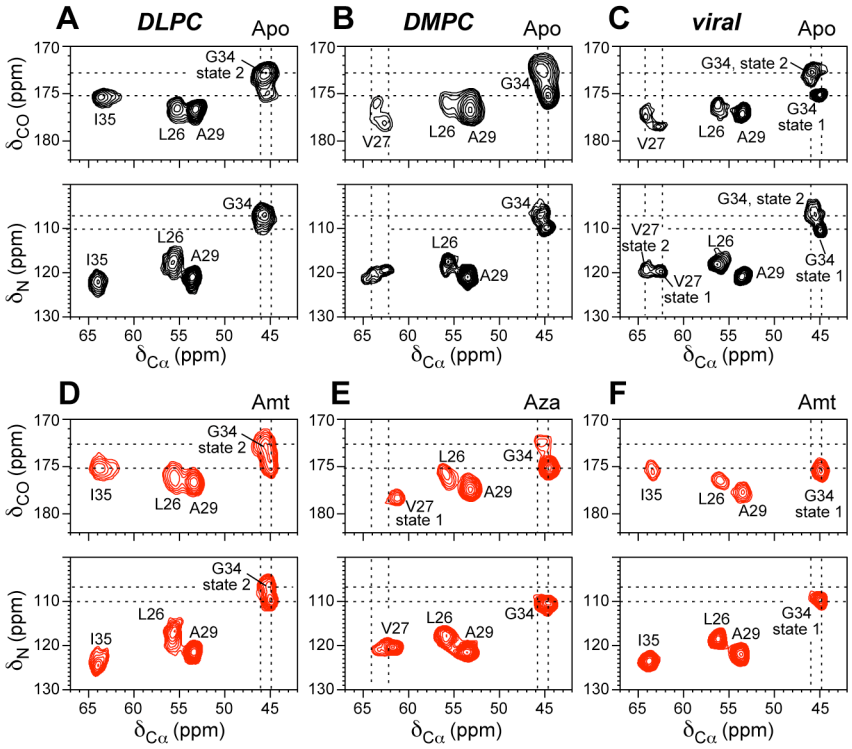

Figure 3.1. M2TM chemical shift changes due to membrane thickness and drug binding from 2D ^{13}C-^{13}C and ^{15}N-^{13}C correlation spectra at pH 7.5. Apo spectra are shown in black and drug-bound spectra in red. A. Apo peptide in DLPC bilayers. B. Apo peptide in DMPC bilayers. C. Apo peptide in virus-mimetic membranes. D. Amantadine-bound peptide in DLPC bilayers. E. M2TM bound to 3-azaspiro[5,5]undecane hydrochloride (Aza) in DMPC bilayers. F. Amantadine-bound peptide in virus-mimetic membranes. The viral membrane spectra (C, F) were measured at 303 K, while the other spectra were measured at 243 K. The 2D ^{15}N-^{13}C spectra of DLPC and viral membrane samples were reproduced from [22].

Upon binding of amantadine and 3-azaspiro [5,5] undecane hydrochloride [35], the 2D spectra showed higher state-1 intensities and lower state-2 intensities compared to the apo state in all three membranes. In the viral membrane, G34 now exhibited only the state-1 signals (Figure 3.1F), while in DMPC bilayers the dominant V27 signals also belonged to state 1 (Figure 3.1E). The other four sites, L26, A29, A30 and I35 displayed the same chemical shifts as the apo samples, indicating that their backbone conformation was insensitive to drug binding.

Table 3.1. Isotropic ^{13}C and ^{15}N chemical shifts (ppm) of M2TM residues with significant chemical shift changes among the three conformational states.

Site	State 1 (high pH, thick bilayers, drug binding)			
	V27	S31	G34	H37
N	119.7	121.4	110.4	118.1
CO[a]	178.6	173.1	175.1	175.1
Cα	62.4	61.3	44.9	55.1
Cβ	30.1	59.8	-	30.6
	State 2 (high pH, thin bilayers, apo)			
	V27	S31	G34	H37
N	120.4	114.7	107.1	118.1
CO	177.8	173.7	173.0	175.1
Cα	63.8	61.2	45.7	55.1
Cβ	29.7	60.8	-	27.9
	State 3 (low pH, thick bilayers)			
	V27	S31	G34	H37
N	119.7	114.1	107.8	117.4
CO	177.0	173.7	173.0	174.2
Cα	64.0	61.3	45.7	57.2
Cβ	29.8	61.5	-	26.2

[a.] All ^{13}C chemical shifts are referenced to TMS and ^{15}N chemical shifts are referenced to liquid ammonia.

The shift of conformational equilibrium from state 2 to state 1 by drug binding gave a decisive clue to the nature of the two distinct backbone conformations. ^{15}N anisotropic chemical shifts of M2TM oriented in DMPC/DMPG bilayers indicated that amantadine binding caused a distinct helical kink at G34: the C-terminal segment became tilted by 20° from the bilayer normal whereas the N-terminal segment was tilted by 31° [36]. This kink was also reproduced in MD simulations of M2TM [37]. We thus assigned state 1, which was

promoted by both drug binding and thick bilayers, to the discrete G34-kinked conformation. The state-2 conformation was promoted by thin bilayers and the absence of drugs. The tilt angle of the M2TM helices in DLPC bilayers in the absence of the drug was previously measured to be 35° using ^{15}N NMR of unoriented membranes [21]. However, these experiments probed only a small number of labeled residues that lie in the N-terminal segment of G34, thus, no information about the C-terminal orientation was known. Oriented-membrane ^{15}N NMR measurements on a larger number of labeled residues found that M2TM adopted a similar tilt angle of 35° in DMPC bilayer in the absence of drug [38]. However, the pH of these oriented samples was uncontrolled, and the membrane samples were deposited onto the glass plates from organic solution [38], making it possible that the peptide orientation was measured under acidic pH. Thus, the orientation of apo M2TM at high pH in thin lipid bilayers, and whether any kink exists at G34 in this state, is not yet known experimentally. We thus only assign state 2 to a conformation with likely larger tilt angles than for state 1, but do not specify the G34 conformation.

The effects of pH on the M2TM conformation are shown in Figure 3.2. The ^{13}C and ^{15}N chemical shifts were measured at pH 7.5 and pH 4.5 in the viral membrane. L26, V28, A29 and I32 exhibited the same chemical shifts at both pH, indicating that their conformation was unaffected by pH. As in Figure 3.1C, V27 and G34 exhibited dual conformations at pH 7.5. Upon lowering the pH to 4.5, V27 and G34 displayed only a single set of chemical shifts, which was designated as state 3. The state-3 V27 had a 1.6 ppm larger Cα chemical shift and a counter-directional 1.6 ppm smaller CO chemical shift (Table 3.1) compared to the high-pH state 1. These low-pH values are similar to the state-2 chemical shifts of V27, which were obtained in thin bilayers at high pH. For G34, the low-pH state 3 chemical shifts are moderately larger for Cα (0.8 ppm) while the CO and ^{15}N chemical shifts are significantly smaller (2.1 ppm and 2.6 ppm, respectively) than the state-1 chemical shifts (Table 3.1), but are similar to the state-2 chemical shifts (Figure 3.1). In addition to these individual chemical shift changes, V27 and G34 peaks broadened significantly at low pH compared to the high-pH state 1: the ^{13}C and ^{15}N linewidths increased by an average of 0.9 ppm and 0.6 ppm, respectively, compared to the apo peptide in the viral membrane. This line broadening indicates that the low-pH state-3 conformational distribution is a single Gaussian

with a large width [39], in contrast to the narrowly peaked conformational distribution of state 1 at high pH.

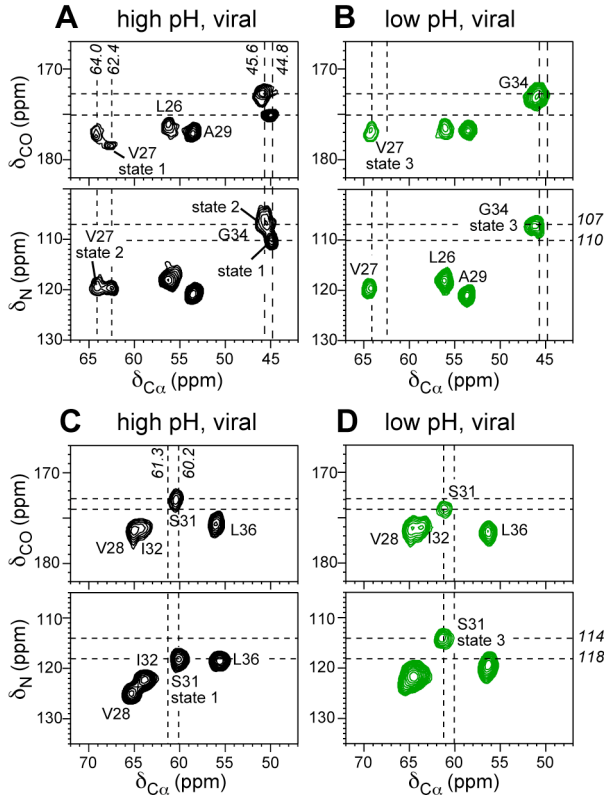

Figure 3.2. 2D ^{13}C-^{13}C and ^{15}N-^{13}C correlation spectra of viral-membrane-bound M2TM at pH 7.5 (black) and pH 4.5 (green). A. V27 and G34-containing M2TM spectra at pH 7.5 at 303 K (same as Figure 3.1C). B. V27 and G34-containing spectra at pH 4.5 at 303 K. C. S31-containing M2TM spectra at pH 7.5. D. S31-containing spectra at pH 4.5. Spectra (C, D) were measured at 273 K for the ^{13}C-^{13}C spectra and 243 K for the ^{15}N-^{13}C spectra.

S31 is the closest residue to amantadine in the drug-complexed peptide [16, 29] and was shown to increase its ^{15}N chemical shift by a striking 7 ppm from the apo state in DLPC bilayers [30]. Interestingly, S31 chemical shifts also exhibited pH sensitivity, as seen in the spectra for viral-membrane samples (Figure 3.2C, D): low pH increased the S31 Cα and CO chemical shifts while decreasing the ^{15}N chemical shift by ~ 4 ppm compared to the apo peptide in the viral membrane at high pH. Based on the secondary-structure dependent

chemical shift trends [40], these changes suggest that the S31 backbone became more ideally helical at low pH.

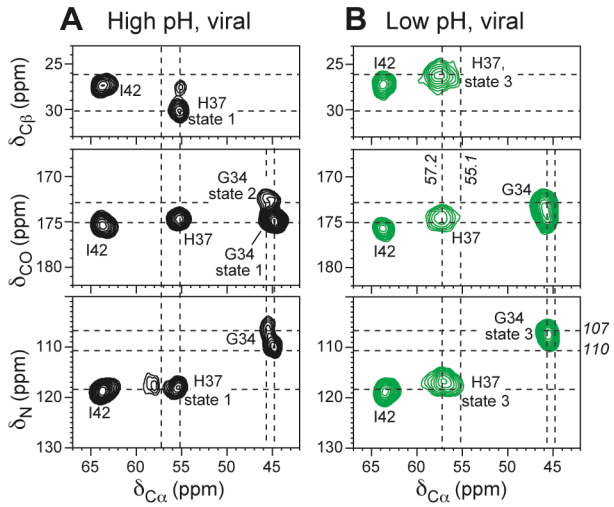

Figure 3.3. His37 and G34 chemical shifts of viral-membrane-bound M2TM at pH 8.5 (A) and pH 4.5 (B), measured at 273 K. From top to bottom, the $^{13}C\alpha$-$^{13}C\beta$ region, the ^{13}CO-$^{13}C\alpha$ region, and ^{15}N-$^{13}C\alpha$ region of 2D spectra are plotted.

Histidine 37 is the proton-gating residue of the M2 channel [14] and is thus expected to have large conformational dependence on pH. Figure 3.3 compares the spectra of G34, H37 and I42 labeled M2TM at pH 8.5 and pH 4.5 in the viral membrane. Similar to V27 and G34, H37 exhibited two well-defined conformations at high pH and only a single, but broadly distributed, conformation at low pH. The two high-pH conformations differ by 2.7 ppm in the Cβ chemical shift. We did not measure the spectra of amantadine-bound H37. However, since all other pore-lining residues show the dominant conformation in the viral membrane to be identical to the amantadine-induced conformation, we tentatively attribute the main Cβ chemical shift of 30.6 ppm (Table 3.1) to the state caused by amantadine, which is state 1. The minor peak at 27.9 ppm is attributed to state 2, which is expected to be present at higher amounts in thin membranes in the absence of the drug.

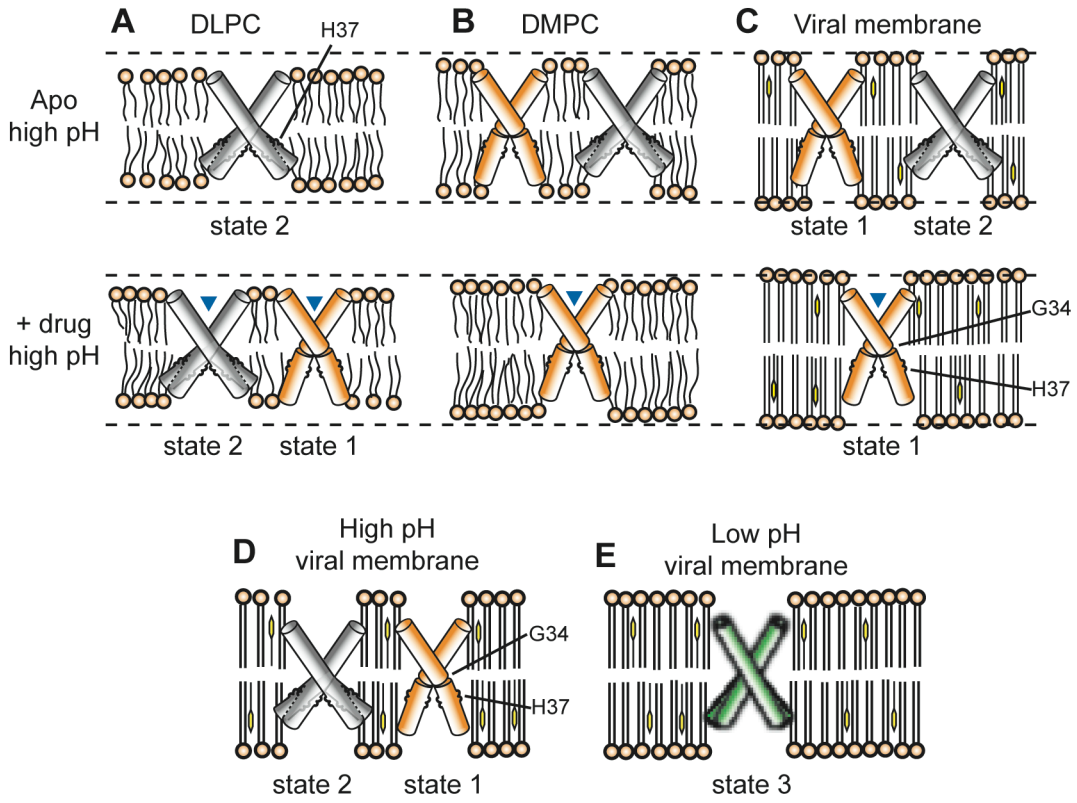

Figure 3.4. Schematic of the effects of membrane thickness, drug binding and pH on M2TM conformation. For clarity only two of the four helices are drawn. A. DLPC bilayers. B. DMPC bilayers. C. Virus-mimetic bilayers. Top row: Without drug. Bottom row: With amantadine or 3-azaspiro[5,5]undecane hydrochloride. Dashed lines guide the eye for the bilayer thickness. Thicker membranes and drug binding promote a conformation with a well-defined G34 kink, which is shown as a break in the helical rod. Thin membranes and the absence of drug promote a broadly distributed conformation at G34, which is illustrated as two orientations of the helix C-terminal to G34. Non-ideal helical conformation at H37 is represented as small wiggles in the rods. D. High-pH conformation of M2TM in viral membranes. E. Low pH conformation of M2TM in viral membranes. Low pH promotes a more ideal helical conformation at H37 and increases the conformational distributions of the protein.

Compared to the dominant chemical shifts at pH 8.5, lowering the pH changed the H37 pH 4.5 Cα and Cβ chemical shifts counter-directionally: the Cα chemical shift

increased by 2.1 ppm while the Cβ chemical shift decreased by a large 4.4 ppm (Table 3.1). These changes indicate a more ideal α-helical conformation for H37 at low pH. Smaller changes of CO and ^{15}N chemical shifts were also observed. In addition to the H37 chemical shift changes, the pH 8.5 spectra also showed a higher fraction of G34 in state 1 compared to its fraction at pH 7.5 (Figure 3.1), suggesting that the effect of pH on the protein conformation equilibrium is incremental: the higher the pH, the larger amount of state-1 conformation.

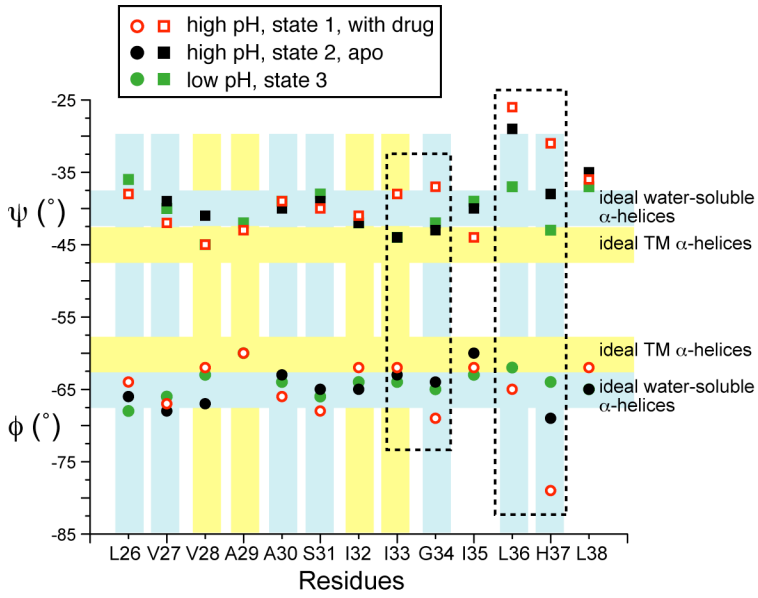

Figure 3.5. (ϕ, ψ) torsion angles of three states of M2(22-46) constrained by isotropic ^{13}C and ^{15}N chemical shifts using TALOS+ [34]. The largest torsion angle changes are observed at G34 and H37. Yellow bars indicate torsion angles of ideal transmembrane helices (horizontal) and residues that fall into this category (vertical), which are predominantly lipid-facing residues in M2TM. Blue bars indicate the torsion angles of ideal water-soluble helices (horizontal) and residues that fall into this category (vertical), which are mostly pore-lining residues.

The chemical shift changes of V27, G34 and H37 shown in Figures 3.1-3.3 are coupled, in the sense that the signals of multiple residues in the same state change collectively with the environment. Moreover, the chemical shifts under a certain combination of conditions are the superposition of the three basis conformations identified here. The

effects of multiple external parameters on the protein conformation are additive. For example, when thick bilayers, high pH and drug binding are combined, M2TM is almost exclusively in state 1 (Figure 3.1C). The corollary of this statement is that counter-acting external parameters cause a mixture of conformations. For example, the drug-complexed M2TM in thin bilayers at high pH (Figure 3.1D) shows a roughly equimolar mixture of state-1 and state-2 conformations.

Table 3.1 lists the chemical shifts of the three basis states for the four environment-sensitive pore-lining residues: V27, S31, G34 and H37. Because Table 3.1 lists only basis-state chemical shifts, not all chemical shifts observed in the spectra are included. For example, the apo-peptide chemical shifts in the viral membrane at high pH (Figure 3.2C) are intermediate between the state 1 and state 2 values, and are not represented in Table 3.1. Inspection of the chemical shifts confirms that state 2 and state 3 are similar for the first three residues, while H37 shows distinct chemical shifts between the high-pH state 2 and the low-pH state 3.

Figure 3.4 depicts the effects of membrane thickness, drug binding, and pH on the M2TM conformation. In DLPC bilayers at high pH, the apo M2TM mainly adopts the state-2 conformation, which is characterized by non-ideal helical conformation at H37 and likely a large average tilt angle (Figure 3.4A). Several lines of evidence suggest that the G34 conformation in state 2 is heterogeneous, containing both highly kinked and relatively straight conformations. First, the state-2 G34 peaks are always broader than in state 1 (Figure 3.1). Second, MD simulations of the apo peptide found the presence of both large and no kink angles at G34 [37]. Third, TALOS torsion angles derived from the measured isotropic chemical shifts (see below) resulted in a state-2 α-helix with an average kink of 10° at G34, which is larger than the kink found in state 1. As the bilayer thickness increases, the state-1 conformation becomes dominant (Figure 3.4B,C). This state has a well-defined G34 kink and similarly non-ideal H37 torsion angles, and the helix may be less tilted than in DLPC bilayers to better match the hydrophobic thickness of the membrane. In Figure 3.4, we represent the well-defined G34 kink in the drug-bound state 1 as a break in the helical rod, while denoting the distribution of G34 conformation in state 2 as two C-terminal helical rods with different orientations with respect the N-terminal segment. We depict and the non-ideal conformation

of H37 at high pH as small wiggles in the helical rod. Drug binding, similar to thick bilayers, shifts the conformational equilibrium to state 1, and when the drug binds to the protein in the thick virus-mimetic membrane, state-1 conformation is the only one observed. In comparison, the drug-free M2TM in the thick membrane adopts both state-1 and state-2 conformations (Figure 3.4D). Upon lowering of pH, M2TM adopts more ideal helical conformation at H37 (Figure 3.4E). Although state 3 shows only a single averaged structure, the larger spectral linewidths suggest that small conformational fluctuations abound, which is represented here by a blurred helical rod. These conformational fluctuations may support proton conduction by providing the conformational flexibility necessary to conduct protons.

M2TM torsion angles and helix conformations in three basis states

To obtain more quantitative information about the helical structure of M2TM in various states, we inputted the conformation-dependent Cα, Cβ, CO and ^{15}N chemical shifts into the TALOS+ program [34] to calculate the average (ϕ, ψ) torsion angles. Figure 3.5 and Table 3.2 give the torsion angles for residues 26 – 43 in the three conformational states. No chemical shifts were available for the segment from I39 to W41, thus we used the (ϕ, ψ) angles obtained from orientation and distance constraints [16, 36] for all three basis states. We found that state 2, which is promoted by thin lipid bilayers and no drug, shows similar torsion angles as the low-pH state 3. State 1, promoted by thick membranes and drug binding, differ significantly from the other two states at S31, G34 and I35. The L36-H37 segment shows the largest (ϕ, ψ) angle differences among the three states: the low-pH state 3 exhibits the most ideal (ϕ, ψ) angles of (-64°, -43°), while the drug-bound high-pH state 1 has (ϕ, ψ) angles of (-79°, -31°). This result is interesting, as it indicates that amantadine binding at S31 perturbs the conformation of the pH-activation residue two helical turns away. This drug-induced conformational change is qualitatively consistent with the measured perturbation of the H37 pKa by amantadine [41]. At low pH, electrostatic repulsion pushes the four helices apart, relieving steric hindrance and allowing the H37 tetrad to adopt more ideal torsion angles. At high pH, drug binding favors a kink at G34, which reduces the distance among the four neutral imidazoles, allowing them to interact strongly with each other [42].

Table 3.2. M2TM (ϕ, ψ) torsion angles predicted from the SSNMR isotropic chemical shifts using TALOS+ [34].

Residue	Set 1		Set 2		Set 3	
	ϕ	ψ	ϕ	ψ	ϕ	ψ
L26	-64±3	-38±9	-66±2	-38±8	-68±3	-36±9
V27	-67±8	-42±7	-68±9	-39±13	-66±7	-40±9
V28	*-62±4*	*-45±5*	*-67±11*	*-41±10*	*-63±5*	*-45±9*
A29[b]	*-60±5*	*-43±6*	*-60±5*	*-43±6*	*-60±5*	*-42±8*
A30	-66±4	-39±6	-63±6	-40±7	-64±7	-39±7
S31	-68±8	-40±7	-65±9	-39±6	-66±9	-38±7
I32	-62±5	-41±9	-65±4	-42±9	-64±4	-42±9
I33[b]	*-62±4*	*-38±7*	*-63±3*	*-44±10*	*-64±4*	*-44±9*
G34[c]	-69±15	-37±14	-64±4	-43±7	-65±4	-42±7
I35	-62±5	-44±4	-60±4	-40±5	-63±4	-39±6
L36[c]	-65±6	-26±14	-65±7	-29±14	-62±4	-37±9
H37[c]	-79±17	-31±19	-69±7	-38±8	-64±4	-43±5
L38	-62±5	-36±10	-65±6	-35±9	-65±5	-37±8
I39[a]	-63	-45	-63	-45	-63	-45
L40[a]	-62	-43	-62	-43	-62	-43
W41[a]	-66	-44	-66	-44	-66	-44
I42[a]	-67	-43	-67	-43	-67	-43
L43	-60±3	-40±7	-63±8	-39±7	-63±8	-39±7
Standard deviation	5.1	4.9	2.5	4.0	2.0	2.5

[a] Torsion angles taken from the PDB structure 2KQT [16], which were constrained by N-H bond orientations [36, 38] and several distance constraints [61].

[b.] Residues whose conformation most approaches the predicted ideal α-helices in hydrophobic environments [57].

[c.] Residues exhibiting large conformational changes among different states or large (ϕ, ψ) uncertainties.

Figure 3.6 shows the helical conformations of the three basis states obtained from the chemical-shift constrained (ϕ, ψ) angles. The three monomers are oriented to reflect the approximate tilt angle in lipid bilayers, and the channel axis is approximately the vertical axis away from the H37 imidazole rings. Using the average N-H vector orientations for residues 27-33 and residues 36-42, we found that the kink angle at G34 was 6.6° for state 1, 10.1° for state 2, and 9.4° for state 3. Thus, the low-pH state 3 and the high-pH thin-membrane state 2 actually contain slightly larger kinks at G34. However, the kink occurs in different directions from the drug-complexed state-1 conformation (Figure 3.6). Aligning the N-terminal segments for all three states, we found that the C-terminal helix orientations are 11° apart between states 1 and 2, and similarly 11° apart between states 1 and 3, but only 2° different between state 2 and state 3. Superposition of the helices shows the deviation of the C-terminal orientation between state 1 and the other two states.

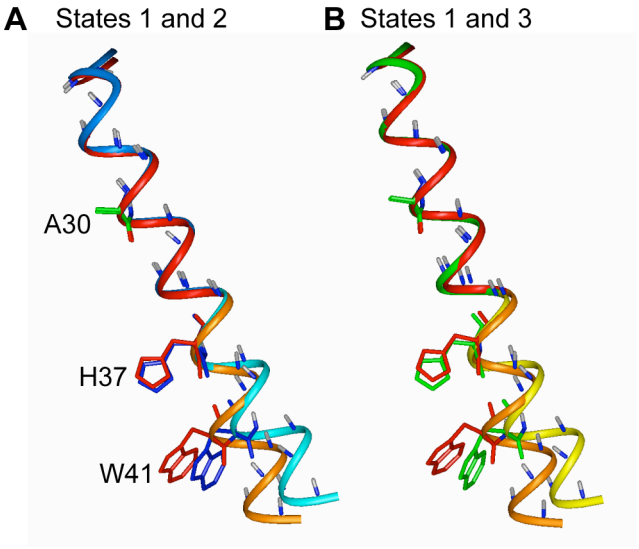

Figure 3.6. Comparison of M2TM helical conformations in the three basis states. The helix conformations were constructed using chemical-shift-derived TALOS+ torsion angles (Table 3.2). A. State 1 (red and orange) is favored by amantadine binding and thicker membranes. State 2 (blue and cyan) is promoted by thin membranes and no drug. B. State 1 superimposed with state 3 (green and yellow), which is favored by low pH.

Discussion

Helix kink at G34

The conformational plasticity of M2TM has been noted before in various experiments. Uniaxially aligned M2TM on glass plates showed that the membrane reconstitution protocol, amantadine, and pH can all affect the peak positions and linewidths of the ^{15}N anisotropic spectra [20]. Amantadine binding caused a well-defined kink at G34 [36], whereas decreasing the pH mainly increased the protein conformational distribution. The low-pH induced increase of the conformational distribution was also reported for DHPC micelle-bound M2(18-60) studied by solution NMR [19].

The MAS spectra obtained here provide further insights into the nature of the M2TM conformational plasticity. The isotropic chemical shifts directly indicate the backbone (ϕ, ψ) angles, thus they probe the degree of helix ideality under various environmental conditions. The spectra in Figure 3.1 showed that the V27, S31, and G34 underwent coupled conformational changes with drug binding and membrane thickness. Increasing the membrane thickness produced similar effects as drug binding. The state 1 that is favored by drug binding is characterized by less ideal helical torsion angles for G34. This G34 non-ideality is consistent with the oriented ^{15}N NMR result [36], but our data further reveals that the kinked G34 conformation is already present in the apo state, since state-1 signals are already manifested in the apo membrane spectra in Figure 3.1A-C.

The helical kink at G34 was recently examined in more detail by MD simulations that reproduced the oriented solid-state NMR ^{15}N spectra [37]. It was found that in DMPC bilayers at high pH, apo M2TM exhibited two populations of conformations: ~35% of the peptide showed large kink angles of 25-50° at G34, while ~65% major fraction exhibited a straight helix with no kink. In comparison, the amantadine-bound peptide exhibited a uniform kink angle of ~10° at G34. Thus, these simulations predicted three G34 conformations, an ideal helix with no kink (0°), a narrowly distributed and small kink of 10°, and a broadly distributed kink at much larger angles. Our apo-peptide spectra show two distinct sets of G34 peaks, where the set with narrower linewidths is identical to the drug-bound peaks. We attribute the set of broader peaks (state 2) to the combination of straight and significantly kinked conformations seen in the MD simulations, since the larger linewidths are consistent with the broad distribution of kink angles.

It is generally known that membrane peptides adapt their orientations in lipid membranes to minimize the hydrophobic mismatch with the lipid bilayer [43, 44], so that a thicker bilayer might be expected to promote straight helices with small tilt angles. Thus, the presence of a distinct kink in M2TM bound to the thick viral membrane may appear at first surprising. However, the kink needs not contradict a smaller tilt angle or a larger hydrophobic length along the bilayer normal. In the amantadine-bound M2TM structure, the C-terminal segment is much less tilted (20°) than the average tilt angle of 35° for the apo peptide [36]. If we assume that the same conformation is applicable to the thick membrane, as suggested by the similar chemical shifts between the two states, then the direction of the G34 kink actually increases the hydrophobic length of the peptide in the thick membrane, thus reducing the hydrophobic mismatch with the bilayer. Therefore, whether helical kinks are favorable for reducing hydrophobic mismatch depend on whether the kinks cause part of the helices to adopt larger or smaller tilt angles. For the same reason, the TALOS-predicted kink angle of 10° for state 2, found in thin lipid bilayers, is not surprising, because the kink has an opposite direction to that of state 1 such that it should cause a larger tilt angle for the C-terminal segment and thus decrease the hydrophobic thickness of the peptide.

Interestingly, a kink in the transmembrane helix of the HIV virus Vpu protein, observed in oriented ^{15}N NMR spectra [45] was present in DOPC bilayers (18:1 chains) but absent in thinner bilayers. Moreover, the kinked residue, I17, also lies in the middle of the helix, similar to the position of G34 in M2TM. At present we do not fully understand the origin of kink formation in the middle of transmembrane helices. Elucidation of this phenomenon will likely require consideration of multiple factors, such as the type and position of the anchoring residues [46], lateral pressure and viscosity distributions within the bilayer [30], and the amino acid sequence of the protein. The last aspect is relevant because the structure of oligomeric ion channels is not only influenced by protein-lipid interactions but also by protein-protein interactions that are required to maintain function.

V27 and S31 conformations

State 1 exhibits less ideal helical chemical shifts for V27 (Table 3.2), which is most likely due to the interaction of V27 sidechains with amantadine, as shown by recent distance

measurements between amantadine and V27 [16]. This less ideal V27 conformation is consistent with an MD simulation that suggested V27 to act as a secondary gate for amantadine, forming an extended blockage of the water wire in the channel pore in the presence of the drug [47].

Decreasing the membrane thickness and removing amantadine shifted the conformational equilibrium to state 2, which has more ideal helical conformations for V27. Interestingly, state 2 was not found by itself under any of the experimental conditions used here, but always coexisted with state 1, while the discretely kinked state-1 conformation can be isolated by using thick lipid bilayers and adding amantadine. Thiol-disulfide exchange experiments showed that the M2TM tetramers are significantly stabilized in thicker bilayers containing cholesterol [48], indicating that the discretely kinked state 1 corresponds to the thermodynamically more stable conformation. Since cholesterol and palmitoyl-chain lipids are also the main ingredients of virus envelope membranes [22], while 12-carbon lipid chains are uncommon, the state-1 conformation is also likely the more functional structure than state 2 at high pH.

The S31 Cβ chemical shift in various states is noteworthy: it is similar to Cα chemical shift in states 2 and 3, but 1.5 ppm upfield from Cα in the drug-bound state 1 (Table 3.1). Although the similar S31 Cα and Cβ chemical shifts make the signals more difficult to resolve than other residues in 2D spectra, spectral editing experiments that suppressed the CH signals while selectively detecting the CH_2 signals confirmed these Cβ chemical shift values [29, 49]. The slightly upfield Cβ chemical shift in state 1 deviates from the database average, which shows the Cβ chemical shift to be larger than Cα in both α-helical and β-sheet conformations [50, 51]. Since the Cβ chemical shift is significantly influenced by the hydroxyl oxygen in addition to (ϕ, ψ) angles, we attribute the upfield Cβ shift in state 1 to perturbations of the hydroxyl environment by drug binding. ^{1}H spin diffusion experiments from water to the protein [52] clearly indicate that amantadine, which binds at S31 [16], significantly dehydrates the channel, which should remove H-bonding between the hydroxyl and water molecules. The increased electron density at the OH should increase the shielding of Cβ, thus causing a smaller chemical shift. Among the three states, the Cβ chemical shift is closest to the ideal α-helical value in the state 3. This is consistent

with the better hydration of the channel at low pH, which should allow extensive hydroxyl-water H-bonding [18, 52, 53], thus causing a deshielding effect on Cβ. Thus, the Cβ chemical shift variation among the three states, while subtle, is consistent with the expected structural changes of the channel at this important residue.

H37 conformation and the influence of pH

H37 backbone conformation showed significant non-ideality at high pH (Figure 3.3). The predicted (ϕ, ψ) angles were (-79°, -31°) for state 1 and (-69°, -38°) for state 2. The average (ϕ, ψ) angles of α-helices in water-soluble proteins are (-65°, -40°) [54], while the "ideal" torsion angles of transmembrane α-helices were predicted to be (-60°, -45°) [55, 56]. The 5° counter-directional change in the (ϕ, ψ) torsion angles has been proposed to have a significant effect on the electrostatic surface of α-helices [57], by better shielding the polar carbonyl groups from the hydrophobic environment of the membrane. The high-pH torsion angles of H37 are 15-20° different from the ideal torsion angles for transmembrane α-helices, and are closer to the values for water-soluble helices. The neighboring residues L36 and L38, influenced by H37, also exhibited non-ideal (ϕ, ψ) angles, although not as strongly as H37. For all three residues, the strongly negative ϕ angles and the less negative ψ angles translate to larger angles between adjacent peptide planes [57] and suggest that the carbonyl oxygens are less well hydrogen-bonded to their intra-helical partners but more exposed to the solvent. Based on this observation, we hypothesize that the deviation of the high-pH H37 conformation from an ideal transmembrane α-helix may result from either intermolecular H-bonding of the H37 carbonyl with water molecules, or aromatic interactions among the four histidines due to tight inter-helical packing at high pH [58].

Lowering the pH moved the H37 Cα chemical shift downfield and the Cβ chemical shift upfield (Table 3.1), indicating a more ideal helical conformation (Figure 3.5). This more ideal backbone is consistent with opening of the channel at this position due to the electrostatic repulsion of the positively charged imidazolium at low pH [58]. Indeed, X-ray crystal structures of M2TM as a function of pH [18, 53] showed that the C-terminal helices increasingly move apart from each other at lower pH, facilitating proton conduction into the cell.

At low pH, MD simulations found that the large-kink population at G34 became more populated, which was interpreted as facilitating proton conduction by creating a wider pore at the H37-W41 juncture. Our chemical shift data show that the low-pH G34 chemical shifts (state 3) are nearly the same as the apo G34 chemical shifts at high pH (state 2), thus supporting this prediction.

Conformational difference between lipid-facing and pore-lining residues

The chemical-shift-constrained (ϕ, ψ) torsion angles in Figure 3.5 and Table 3.2 reveal the interesting trend that lipid-facing residues V28, A29, I32 and I33 adopt (ϕ, ψ) angles expected for transmembrane α-helices, with less negative ϕ angles and more negative ψ angles. The average state-1 (ϕ, ψ) angles for the lipid-facing residues are (-62°, -42°), whereas the pore-facing residues V27, A30, S31, G34 and H37 have average (ϕ, ψ) angles of (-70°, -38°) in state 1, closer to the values for water-soluble helices. This difference suggests the sensitivity of isotropic chemical shifts to ~5° changes in the torsion angles, due to changes in the local dielectric environment faced by the residues in this TM helical bundle.

This study shows the sensitivity of NMR chemical shifts to membrane protein conformations. With the availability of increasingly sophisticated structure prediction methodologies [59], it will be worthwhile to investigate the folding and conformational transitions of oligomeric membrane proteins at higher resolution using chemical shifts as the main input [60]. The general difficulties of measuring intermolecular and intramolecular distances in homo-oligomeric membrane proteins provide further incentives to using chemical shifts as the main experimental input for mapping out conformational changes under a wide range of conditions.

Acknowledgements

This work was funded by an NSF grant MCB-0543473 and an NIH grant GM088204.

References

[1] S.B. Long, X. Tao, E.B. Campbell, R. MacKinnon, Atomic structure of a voltage-dependent K+ channel in a lipid membrane-like environment, Nature 450 (2007) 376-383.

[2] K. Brejc, W.J. van Dijk, R.V. Klaassen, M. Schuurmans, J. van Der Oost, A.B. Smit, T.K. Sixma, Crystal structure of an ACh-binding protein reveals the ligand-binding domain of nicotinic receptors, Nature 411 (2001) 269-276.

[3] D.M. Engelman, Crossing the hydrophobic barrier: insertion of membrane proteins, Science 274 (1996) 1850-1851.

[4] S.L. Slatin, X. Qiu, K.S. Jakes, A. Finkelstein, Identification of a translocated protein segment in a voltage-dependent channel, Nature 371 (1994) 158-161.

[5] M.W. Parker, F. Pattus, A.D. Tucker, D. Tsernoglou, Structure of the membrane-pore-forming fragment of colicin A, Nature 337 (1989) 93-96.

[6] V. Vásquez, M. Sotomayor, J. Cordero-Morales, K. Schulten, E. Perozo, A structural mechanism for MscS gating in lipid bilayers, Science 321 (2008) 1210-1214.

[7] R.B. Bass, P. Strop, M. Barclay, D.C. Rees, Crystal structure of Escherichia coli MscS, a voltage-modulated and mechanosensitive channel, Science 298 (2002) 1582-1587.

[8] R.H. Spencer, D.C. Rees, The alpha-helix and the organization and gating of channels, Annu. Rev. Biophys. Biomol. Struct. 31 (2002) 207-233.

[9] A. Mitra, R. Tascione, A. Auerbach, S. Licht, Plasticity of acetylcholine receptor gating motions via rate-energy relationships, Biophys J. 89 (2005) 3071-3078.

[10] K.A. Dill, H.S. Chan, From Levinthal to pathways to funnels, Nat. Struct. Biol. 4 (1997) 10-19.

[11] L.H. Pinto, R.A. Lamb, Controlling influenza virus replication by inhibiting its proton flow, Mol. BioSyst. 3 (2007) 18-23.

[12] L.H. Pinto, L.J. Holsinger, R.A. Lamb, Influenza virus M2 protein has ion channel activity, Cell 69 (1992) 517-528.

[13] C. Wang, K. Takeuchi, L.H. Pinto, R.A. Lamb, Ion channel activity of influenza A virus M2 protein: characterization of the amantadine block, J. Virol. 67 (1993) 5585-5594.

[14] C. Wang, R.A. Lamb, L.H. Pinto, Activation of the M2 ion channel of influenza virus: a role for the transmembrane domain histidine residue, Biophys. J. 69 (1995) 1363-1371.

[15] Y. Tang, F. Zaitseva, R.A. Lamb, L.H. Pinto, The gate of the influenza virus M2 proton channel is formed by a single tryptophan residue, J. Biol. Chem. 277 (2002) 39880-39886.

[16] S.D. Cady, K. Schmidt-Rohr, J. Wang, C.S. Soto, W.F. DeGrado, M. Hong, Structure of the amantadine binding site of influenza M2 proton channels in lipid bilayers, Nature 463 (2010) 689-692.

[17] C. Ma, A.L. Polishchuk, Y. Ohigashi, A.L. Stouffer, A. Scho¨n, E. Magavern, X. Jing, J.D. Lear, E. Freire, R.A. Lamb, W.F. DeGrado, L.H. Pinto, Identification of the functional core of the influenza A virus A/M2 proton-selective ion channel, Proc. Natl. Acad. Sci. USA 106 (2009) 12283-12288.

[18] A.L. Stouffer, R. Acharya, D. Salom, A.S. Levine, L. Di Costanzo, C.S. Soto, V. Tereshko, V. Nanda, S. Stayrook, W.F. DeGrado, Structural basis for the function and inhibition of an influenza virus proton channel, Nature 451 (2008) 596-599.

[19] J.R. Schnell, J.J. Chou, Structure and mechanism of the M2 proton channel of influenza A virus, Nature 451 (2008) 591-595.

[20] C. Li, H. Qin, F.P. Gao, T.A. Cross, Solid-state NMR characterization of conformational plasticity within the transmembrane domain of the influenza A M2 proton channel, Biochim. Biophys. Acta 1768 (2007) 3162-3170.

[21] S.D. Cady, M. Hong, Amantadine-induced conformational and dynamical changes of the influenza M2 transmembrane proton channel, Proc. Natl. Acad. Sci. USA 105 (2008) 1483-1488.

[22] W. Luo, S.D. Cady, M. Hong, Immobilization of the influenza A M2 transmembrane peptide in virus-envelope mimetic lipid membranes: a solid-state NMR investigation, Biochemistry 48 (2009) 6361-6368.

[23] S.D. Cady, C. Goodman, C.Tatko, W.F. DeGrado, M. Hong, Determining the orientation of uniaxially rotating membrane proteins using unoriented samples: a 2H,

13C, and 15N solid-state NMR investigation of the dynamics and orientation of a transmembrane helical bundle, J. Am. Chem. Soc. 129 (2007) 5719-5729.

[24] K.C. Duong-Ly, V. Nanda, W.F. DeGrado, K.P. Howard, The conformation of the pore region of the M2 proton channel depends on lipid bilayer environment, Protein Sci. 14 (2005) 856-861.

[25] A.L. Stouffer, C. Ma, L. Cristian, Y. Ohigashi, R.A. Lamb, J.D. Lear, L.H. Pinto, W.F. DeGrado, The interplay of functional tuning, drug resistance, and thermodynamic stability in the evolution of the M2 proton channel from the influenza A virus, Structure (2008) 1067-1076.

[26] K.P. Howard, J.D. Lear, W.F. DeGrado, Sequence determinants of the energetics of folding of a transmembrane four-helix-bundle protein., Proc. Natl. Acad. Sci. USA 99 (2002) 8568-8572.

[27] V. Balannik, V. Carnevale, G. Fiorin, B.G. Levine, R.A. Lamb, M.L. Klein, W.F. Degrado, L.H. Pinto, Functional studies and modeling of pore-lining residue mutants of the influenza a virus M2 ion channel, Biochemistry 49 (2010) 696-708.

[28] S.D. Cady, W.B. Luo, F. Hu, M. Hong, Structure and function of the influenza M2 proton channel, Biochemistry 48 (2009) 7356-7364.

[29] S.D. Cady, T.V. Mishanina, M. Hong, Structure of amantadine-bound M2 transmembrane peptide of influenza A in lipid bilayers from magic-angle-spinning solid-state NMR: the role of Ser31 in amantadine binding, J. Mol. Biol. 385 (2009) 1127-1141.

[30] S.D. Cady, M. Hong, Effects of amantadine binding on the dynamics of bilayer-bound influenza A M2 transmembrane peptide studied by NMR relaxation, J. Biomol. NMR 45 (2009) 185-196.

[31] K. Takegoshi, S. Nakamura, T. Terao, C-13-H-1 dipolar-assisted rotational resonance in magic-angle spinning NMR, Chem. Phys. Lett. 344 (2001) 631-637.

[32] M. Hong, R.G. Griffin, Resonance assignments for solid peptides by dipolar-mediated C-13/N-15 correlation solid-state NMR, J. Am. Chem. Soc. 120 (1998) 7113-7114.

[33] D.S. Wishart, C.G. Bigam, A. Holm, R.S. Hodges, B.D. Sykes, 1H, 13C and 15N random coil NMR chemical shifts of the common amino acids. I. Investigations of nearest neighbor effects., J. Biomol. NMR 5 (1995) 67-81.

[34] Y. Shen, F. Delaglio, G. Cornilescu, A. Bax, TALOS+: a hybrid method for predicting protein backbone torsion angles from NMR chemical shifts, J. Biomol. NMR 44 (2009) 213-223.

[35] J. Wang, S.D. Cady, V. Balannik, L.H. Pinto, W.F. DeGrado, M. Hong, Discovery of spiro-piperidine inhibitors and their modulation of the dynamics of the M2 proton channel from influenza A virus, J. Am. Chem. Soc. 131 (2009) 8066-8076.

[36] J. Hu, T. Asbury, S. Achuthan, C. Li, R. Bertram, J.R. Quine, R. Fu, T.A. Cross, Backbone structure of the amantadine-blocked trans-membrane domain M2 proton channel from Influenza A virus, Biophys. J. 92 (2007) 4335-4343.

[37] M. Yi, T.A. Cross, H.X. Zhou, Conformational heterogeneity of the M2 proton channel and a structural model for channel activation, Proc. Natl. Acad. Sci. USA 106 (2009) 13311-13316.

[38] J. Wang, S. Kim, F. Kovacs, T.A. Cross, Structure of the transmembrane region of the M2 protein H+ channel., Protein Sci. 10 (2001) 2241-2250.

[39] X.L. Yao, M. Hong, Structural distribution in an elastin-mimetic peptide (VPGVG)3 investigated by solid–state NMR, J. Am. Chem. Soc. 126 (2004) 4199-4210.

[40] D.S. Wishart, B.D. Sykes, F.M. Richards, Relationship between nuclear magnetic resonance chemical shift and protein secondary structure, J. Mol. Biol. 222 (1991) 311-333.

[41] J. Hu, R. Fu, T.A. Cross, The chemical and dynamical influence of the anti-viral drug amantadine on the M2 proton channel transmembrane domain, Biophys. J. 93 (2007) 276-283.

[42] J. Hu, R. Fu, K. Nishimura, L. Zhang, H.-X. Zhou, D.D. Busath, V. Vijayvergiya, T.A. Cross, Histidines, heart of the hydrogen ion channel from influenza A virus: Toward an understanding of conductance and proton selectivity, Proc. Natl. Acad. Sci. USA 103 (2006) 6865-6870.

[43] J.A. Killian, Hydrophobic mismatch between proteins and lipids in membranes, Biochim. Biophys. Acta 1376 (1998) 401-415.

[44] M.R. de Planque, J.W. Boots, D.T. Rijkers, R.M. Liskamp, D.V. Greathouse, J.A. Killian, The effects of hydrophobic mismatch between phosphatidylcholine bilayers and transmembrane alpha-helical peptides depend on the nature of interfacially exposed aromatic and charged residues, Biochemistry 41 (2002) 8396-8404.

[45] S.H. Park, S.J. Opella, Tilt angle of a trans-membrane helix is determined by hydrophobic mismatch, J. Mol. Biol. 350 (2005) 310-318.

[46] M.R. de Planque, B.B. Bonev, J.A. Demmers, D.V. Greathouse, R.E.n. Koeppe, F. Separovic, A. Watts, J.A. Killian, Interfacial anchor properties of tryptophan residues in transmembrane peptides can dominate over hydrophobic matching effects in peptide-lipid interactions, Biochemistry 42 (2003) 5341-5348.

[47] M. Yi, T.A. Cross, H.X. Zhou, A secondary gate as a mechanism for inhibition of the M2 proton channel by amantadine, J. Phys. Chem. B 112 (2008) 7977-7979.

[48] L. Cristian, J.D. Lear, W.F. DeGrado, Use of thiol-disulfide equilibria to measure the energetics of assembly of transmembrane helices in phospholipid bilayers., Proc. Natl. Acad. Sci. USA 100 (2003) 14772-14777.

[49] J.D. Mao, K. Schmidt-Rohr, Methylene spectral editing in solid-state C-13 NMR by three-spin coherence selection, J. Magn. Reson. 176 (2005) 1-6.

[50] Y. Wang, O. Jardetzky, Probability-based protein secondary structure identification using combined NMR chemical-shift data., Protein Sci. 11 (2002) 852-861.

[51] H. Zhang, S. Neal, D.S. Wishart, RefDB: A database of uniformly referenced protein chemical shifts, J. Biomol. NMR 25 (2003) 173-195.

[52] W. Luo, M. Hong, Conformational changes of an ion channel membrane protein detected through water-protein interactions using solid-state NMR spectroscopy, J. Am. Chem. Soc. 132 (2010) 2378-2384.

[53] A. Acharya, V. Carnevale, G. Fiorin, B.G. Levine, A. Polishchuk, V. Balannick, I. Samish, R.A. Lamb, L.H. Pinto, W.F. DeGrado, M.L. Klein, Structural mechanism of proton transport through the influenza A M2 protein, Proc. Natl. Acad. Sci. USA 107 (2010) 15075-15080.

[54] L.J. Smith, K.A. Bolin, H. Schwalbe, M.W. MacArthur, J.M. Thornton, C.M. Dobson, Analysis of main chain torsion angles in proteins: prediction of NMR coupling constants for native and random coil conformations, J. Mol. Biol. 255 (1996) 494-506.

[55] T. Blundell, D. Barlow, N. Borkakoti, J. Thornton, Solvent-induced distortions and the curvature of alpha-helices, Nature 306 (1983) 281-283.

[56] S. Kim, T.A. Cross, Uniformity, ideality, and hydrogen bonds in transmembrane alpha-helices, Biophys. J. 83 (2002) 2084-2095.

[57] R.C. Page, S. Kim, T.A. Cross, Transmembrane helix uniformity examined by spectral mapping of torsion angles, Structure 16 (2008) 787-797.

[58] F. Hu, W. Luo, M. Hong, Mechanisms of proton conduction and gating by influenza M2 proton channels from solid-state NMR, Science 330 (2010) 505-508.

[59] S. Raman, O.F. Lange, P. Rossi, M. Tyka, X. Wang, J. Aramini, G. Liu, T.A. Ramelot, A. Eletsky, T. Szyperski, M.A. Kennedy, J. Prestegard, G.T. Montelione, D. Baker, NMR structure determination for larger proteins using backbone-only data, Science 327 (2010) 1014-1018.

[60] R.H. Havlin, R. Tycko, Probing site-specific conformational distributions in protein folding with solid-state NMR, Proc. Natl. Acad. Sci. USA 102 (2005) 3284-3289.

[61] W. Luo, R. Mani, M. Hong, Sidechain conformation and gating of the M2 transmembrane peptide proton channel of influenza A virus from solid-state NMR, J. Phys. Chem. 111 (2007) 10825-10832.

Chapter 4

pH-Dependent Histidine-Water Proton Exchange Reveals the Conduction Mechanism of a Transmembrane Proton Channel

An article in preparation

Fanghao Hu and Mei Hong

Abstract

The atomic mechanism of proton conduction across biological membrane is complex and only beginning to be revealed by high-resolution structural methods. The acid-activated proton channel formed by the influenza M2 protein serves as a model system for larger voltage-gated proton channels. A single histidine, His37, in the M2 transmembrane (TM) domain is responsible for channel activation. Recent reports led to three competing models for how His37 mediates proton transport: a shuttle mechanism involving imidazole reorientation, a hydrogen-bonded imidazole-imidazolium dimer model, and a transporter model involving large protein conformational changes in synchrony with proton transport. Using ^{15}N solid-state NMR, we find that at physiological temperature, pH, and membrane composition, imidazole nitrogens exchange between protonated and unprotonated states at the functional rate of ~3000 s^{-1}. The slow timescale and strong temperature dependence of the exchange, and the lack of close contact between neutral and cationic histidines, rule out inter-histidine low-barrier hydrogen bonds and support water-imidazole proton transfer. Quantification of neutral and cationic histidine concentrations in the virus-mimetic membrane yielded four pK_a's that differ from model membrane results, suggesting the influence of the membrane environment on the protonation equilibria. These pK_a's provided semi-quantitative estimates of the relative conductivities of the different charged states. At physiological acidic pH, M2 exhibits two backbone conformations, which do not exchange on the sub-10 ms timescale in the virus-mimetic membrane. Binding of the antiviral drug, amantadine, stopped proton exchange and imidazole reorientation, proving that the ring-motion-facilitated imidazole-water proton exchange is the fundamental mechanism of proton conduction.

Introduction

The M2 protein of the influenza virus forms a proton-selective ion channel that mediates virus entry and prevents premature conformational changes of hemagglutinin by maintaining the high pH of the *trans*-Golgi network (1, 2). M2 also mediates membrane scission and virus budding from the host cell (3, 4). During virus entry, M2 is activated by the low pH of the endosome and conducts 10-10,000 protons per second into the virion (5, 6), which causes uncoating of the ribonucleoprotein and its transport into the host cell nucleus. A single histidine, His37, in the TM domain of the protein is responsible for pH activation and proton selectivity of the channel (7, 8). The channel is irreversibly inhibited by amantadine (Amt) and rimantadine (9), which bind specifically to the TM pore (10-13).

Several recent high-resolution structures of the M2 protein and the His37 residue led to three different models of how His37 mediates proton transport. A 1.65 Å-resolution crystal structure of the M2 transmembrane domain (M2TM) at pH 6.5 (14) revealed water clusters near the His37 tetrad. Comparison of the protein structures solved at different pH's (11, 15, 16) showed pH-dependent changes of the tilt angles of the N- and C-terminal halves of the TM helix, which were reproduced in MD simulations (17, 18). These observations led to a transporter model in which M2TM undergoes backbone conformational changes in synchrony with proton transport (19), and protons diffusing through the channel are delocalized over all four histidines and their associated water clusters. In a second study, MD simulations of His37 structure and interaction with Trp41 (16) suggested a low-barrier H-bond between Nδ1 of a neutral histidine (His) and Nε2H of a cationic His in a +2 tetrad. The third protonation event, which occurs at about pH 6.3 based on ^{15}N NMR spectra of M2TM bound to DMPC/DMPG bilayers (20), is envisioned to disrupt this imidazole-imidazolium dimer and establish cation-π interactions between His37 and Trp41. Subsequent conformational fluctuations may occasionally break this cation-π interaction, thus exposing Nε2H to the C-terminal water, causing proton transfer (16). In a third study, the protonation state, tautomeric structure, H-bonding, and sidechain dynamics of His37 were measured at pH 8.5 and 4.5 in a virus-mimetic membrane using solid-state NMR (21). At pH 8.5, neutral His37 sidechains pack in a CH-π fashion that severely restricts the pore. At pH 4.5, the cationic imidazoliums pack more loosely due to the different backbone conformation, and the

rings reorient at a rate >50,000 s^{-1} with an energy barrier > 60 kJ/mol (21), consistent with the ~100 kJ/mol barrier for proton conduction (5). In comparison, the energy barrier for water-mediated proton conduction was calculated to be at most 40 kJ/mol (22), suggesting that proton transport is not solely mediated by water (23). These data suggested that His37 shuttles protons into the virion through imidazole protonation and deprotonation, facilitated by microsecond ring reorientations.

Evaluation of these models to elucidate the true proton conduction mechanism of M2 is important not only for influenza virology but also for understanding larger and more complex ion channels such as voltage-gated proton channels (24), since the fundamental process of proton transport through a H-bonded chain of water molecules and titratable residues is common to all proton channels. In this study, we use solid-state NMR to investigate proton exchange of His37 imidazole nitrogens at physiologically relevant pH, temperature and membrane composition. ^{15}N chemical shift lineshapes provide definitive evidence for His37 proton exchange with water at functional rates without forming imidazole-imidazolium dimers. Four proton-dissociation equilibrium constants were obtained in the virus-mimetic membrane (25), which allow estimates of the relative conductivities of the differently charged channels. Amt binding suppressed both proton exchange and imidazole reorientation, confirming the centrality of dynamically assisted imidazole-water proton transfer for M2's channel activity.

Results

pH-dependent His37 ^{15}N spectra indicate imidazole protonation and deprotonation on the functional timescale

We measured ^{15}N and ^{13}C MAS spectra (Figure 4.1, 4.S1) of His37-labeled M2TM in the mildly acidic pH range of 7 – 5 and compared them with spectra at the limiting pH of 8.5 and 4.5 (21). ^{15}N chemical shifts are highly sensitive to the protonation state of imidazoles: unprotonated Nδ1(τ) and Nε2(π) in neutral His resonate at ~250 ppm while protonated ^{15}N's in cationic and neutral histidines resonate at 160-190 ppm (26). The Nε2H (176 ppm) and Nδ1H (180 ppm) of cationic His are readily distinguished from the Nε2H(τ) and Nδ1H(π) of neutral His at 159 and 170 ppm based on 2D correlation spectra (Figure 4.2) (21). The 243 K

spectra in Figure 4.1 show the expected trend of higher cationic His intensity and lower neutral His intensity as the pH decreased. Moreover, at physiological temperature, the spectra reveal rich chemical exchange phenomena of the imidazole nitrogens between pH 5.2 and 7.0. At pH 5.2, the unprotonated 250-ppm peak present at 243 K disappeared above 273 K and a new peak at ~213 ppm appeared (Figure 4.1b). This chemical shift is half way between the unprotonated (250 ppm) and charged (178 ppm) ^{15}N frequencies, suggesting that it results from equal-population exchange between the two types of nitrogens with $[N]/[NH] \approx 1$. At 308 K, the equilibrium exchange rate is faster than the ^{15}N chemical shift difference of ~70 ppm or ~3000 s^{-1}, but only moderately so because of the broad intrinsic linewidth of the peak (see below). The nature of this N-NH exchange can be understood from its temperature dependence and rate regime: the presence of the unprotonated 250-ppm peak at 243 K but its disappearance at 308 K, and the μs-ms exchange rate at 308 K, argue against a strong N-H…N hydrogen-bond (see below). Instead, the 213-ppm peak can be assigned to water-mediated dynamic protonation and deprotonation of Nδ1 (Figure 4.3a). It is less likely for Nε2 to undergo this equal-population exchange, because Nε2 has high proton affinities: it is the main protonated nitrogen in neutral His (Figure 4.1e) and it preserves the 159-ppm chemical shift from pH 8.5 to 6 before shifting to larger chemical shifts at lower pH. The Nε2-H bond was also found to be very short (1.03 Å) at pH 8.5 (21), further supporting its high proton affinity.

Not all Nδ1 and Nε2 participate in the dynamic protonation-deprotonation exchange, since the 308 K spectrum at pH 5.2 show residual protonated peaks at 173 ppm and 185 ppm, indicating that some nitrogens retain their protons most of the time. We assign the 173-ppm peak to unexchanged Nε2H and attribute the 185-ppm peak to unexchanged Nδ1H in cationic His.

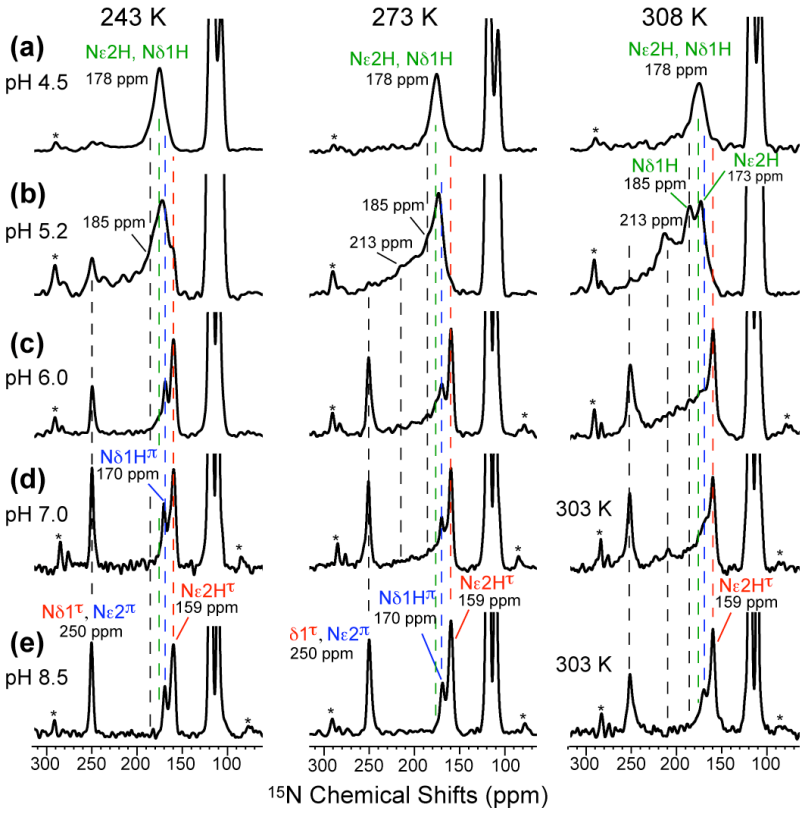

Figure 4.1. 1D ^{15}N CP-MAS spectra of His37-labeled M2TM as a function of pH and temperature. Peak assignments were shown in red for the Nε2-protonated τ tautomer, blue for the Nδ1-protonated π tautomer, and green for cationic histidine. (a) pH 4.5. (b) pH 5.2. (c) pH 6.0. (d) pH 7.0. (e) pH 8.5. Spectra were measured at 243 K, 273 K, and 308 or 303 K. Note the broad intensity distribution and 213 ppm peak at pH 5.2 and 6.0 above 273 K. Asterisks indicate spinning sidebands.

In addition to the 213-ppm exchange peak, a broad slope from 190 to ~220 ppm is also observed from pH 7 to pH 5.2 at high temperature. This peak may be inhomogeneously broadened by a distribution of $[N]/[NH]$ or homogeneously broadened by chemical exchange on the timescale of the inverse of the ^{15}N chemical shift difference. To distinguish these two possibilities, we measured ^{15}N T_2 relaxation times (Figure 4.S2), which reflect the homogeneous linewidth of the spectra. At pH 5.2, the broad peak has a T_2 of 1.7 ms, which is only moderately shorter than the 2.2-2.8 ms T_2's of the other imidazole nitrogens (Table 4.S1). This T_2 value corresponds to a homogeneous linewidth of 4.7 ppm, which is much

smaller than the 30-ppm span of the broad peak. Thus, much of the line broadening is inhomogeneous in nature. The center of mass of this broad peak is closer to the protonated than the unprotonated peaks. These observations suggest that the broad peak results from imidazole nitrogens that exchange between NH and N with a higher population for the NH state and with an exchange rate slower than that of the 213-ppm peak. The most likely site responsible for this exchange is Nε2 (Figure 4.3b), whose strong proton affinity can account for the unequal population as well as the slower exchange rate. Thus, at mildly acidic pH, both Nδ1 and Nε2 undergo exchange, but with different equilibrium constants and rates.

The exchange intensities in the ^{15}N spectra cannot be attributed to strong His-His H-bonding (16, 20), because a low-barrier H-bond, by virtue of its low-lying transition state (27), should induce ultrafast proton exchange between the two nitrogens with weak temperature dependencies, and should give rise to one sharp peak at the average chemical shift for $[N]/[NH]=1$ or two equal-intensity peaks if $[N]/[NH]$ deviates from 1 (26, 28). Variable-temperature ^{15}N NMR spectra of H-bonded imidazole-imidazolium salts confirmed that proton transfer between pK_a-matched bridging nitrogens was fast ($>>10^5$ s^{-1}) at all temperatures above 200 K, and gave rise to a pair of sharp averaged ^{15}N peaks (26). In contrast, membrane-bound M2TM shows ^{15}N exchange peaks with significant homogeneous linewidths of 100-400 Hz, well above the intrinsic linewidths of 30–50 Hz (Table 4.S1). The exchange rate depends sensitively on temperature between 308 K and 243 K (Figure 4.1b), suggesting a high barrier. Moreover, the ^{15}N spectra of DMPC/DMPG-bound M2TM (20) showed neither an exchange peak at the middle of the two limiting frequencies nor a pair of equal-intensity peaks expected for an unequal-population H-bonded pair of nitrogen, contradicting the dimer model.

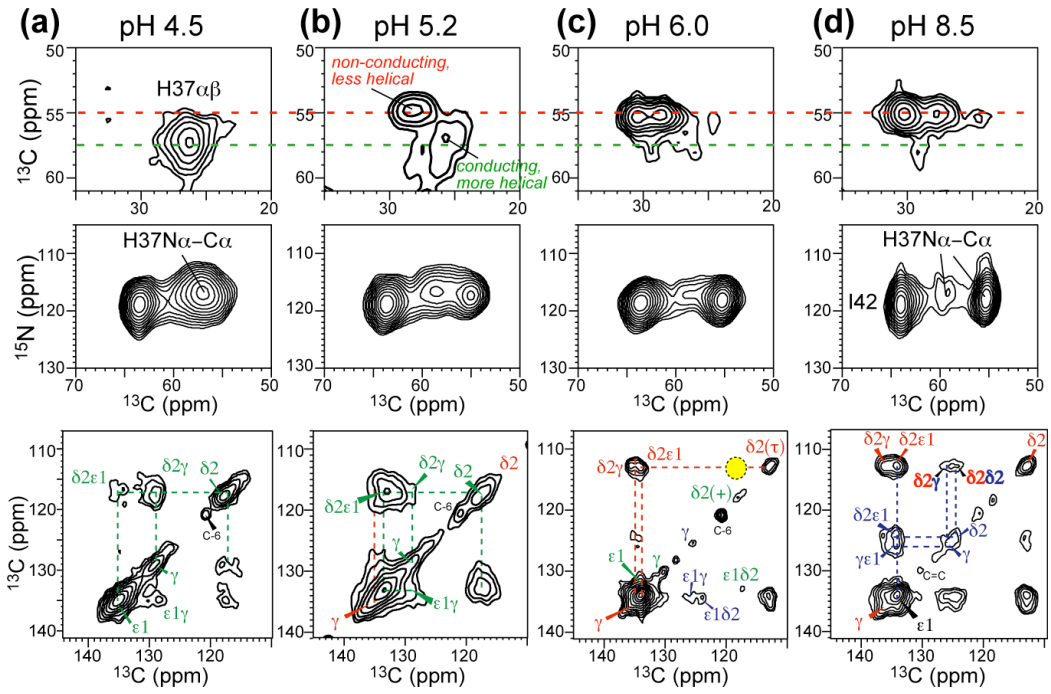

Figure 4.2. 2D ^{13}C-^{13}C and ^{15}N-^{13}C correlation spectra of His37 at 273 K or 243 K as a function of pH. (a) pH 4.5. (b) pH 5.2. (c) pH 6. (d) pH 8.5. From top to bottom, the Cα-Cβ region, N-Cα region and aromatic ^{13}C region. ^{13}C-^{13}C 2D spectra were measured with a 40-60 ms mixing time. No imidazole-imidazolium Cδ2(τ)-Cδ2(+) cross peak was observed (yellow shade) at pH 6.0 where both neutral and cationic rings exist. A 300 ms 2D ^{13}C-^{13}C spectrum (Figure 4.S3) confirmed the lack of imidazole-imidazolium cross peak.

To further test the dimer model, we measured 2D ^{13}C-^{13}C correlation spectra at pH 6, where neutral and cationic His peaks coexist. If H-bonded imidazole-imidazolium dimers are present, cross peaks between the two sidechains are expected. The Cδ2 peak is well resolved between the neutral τ tautomer (112 ppm) and the cationic His (118 ppm) and is thus a nice probe of intermolecular contacts. The His37 dimer model (16) predicts a Cδ2(τ) – Cδ2(+) distance of 5.9 Å, which is within the distance reach of ^{13}C spin diffusion. Figure 4.2c shows no such cross peak within a mixing time of 40 ms. Extending the mixing time to 300 ms confirmed the lack of neutral-cationic Cδ2 cross peak (Figure 4.S3). In comparison, cross peaks between τ and π tautomers were detected at pH 8.5 within 40 ms (Figure 4.2d), confirming that ^{13}C spin diffusion can detect tight intermolecular contacts within the tetrad.

Taken together, the ^{15}N lineshapes and 2D ^{13}C spectra exclude the H-bonded dimer model for proton conduction (16).

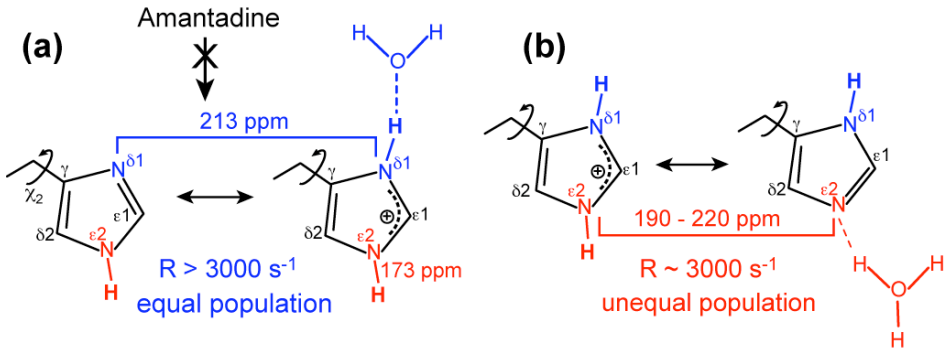

Figure 4.3. Model of His37 Nδ1 and Nε2 protonation and deprotonation to explain the observed ^{15}N exchange peaks. (a) Equal-population Nδ1-Nδ1H exchange. (b) Unequal-population Nε2H-Nε2 exchange. Amt binding suppressed the Nδ1 exchange.

Proton dissociation constants of the His37 tetrad in the virus-mimetic membrane

To understand the protonation equilibria of the His37 tetrad in the virus-mimetic membrane, we integrated the unprotonated and protonated ^{15}N peaks at 243 K. From the I_{NH}/I_N ratios (Figure 4.4a, 4.S4) we obtained the concentration ratio of neutral to cationic His as a function of pH. By simultaneously considering the four protonation equilibria, we determined the four pK_a's as 7.6, 6.8, 4.9, and 4.2 (Figure 4.4b, Table 4.S3). Interestingly, these pK_a's are 0.5-1.5 units lower than the reported values for DMPC/DMPG-bound M2TM, which are 8.2, 8.2, 6.3 and <5 (20). Thus, in the cholesterol-rich virus-mimetic membrane, the four histidines protonate at lower pH than in model membranes, and the first two protonation steps are separate instead of cooperative. The methods for extracting pK_a's differ between the two studies (20). We obtained $[His]/[HisH^+]$ ratios from low-temperature spectra where protein motions are mostly suppressed and where the unprotonated and protonated ^{15}N peaks are well resolved (by more than 70 ppm). We used a model compound to calibrate the intensity scaling factor between N and NH signals to account for their different ^{1}H-^{15}N cross polarization (CP) efficiencies, thus giving accurate ratios of neutral to cationic histidines. In comparison, the previous study obtained $[His]/[HisH^+]$ ratios by

deconvolution of the protonated ^{15}N peak into multiple components. This procedure has large uncertainties due to significant exchange broadening of the spectra and hence severe peak overlap at the temperature of the experiments. Apart from experimental uncertainties, the pK_a differences may also reflect real differences in the protonation equilibria in the two different membranes. The cholesterol-rich virus-mimetic membrane makes it more difficult for the protein backbone to undergo conformational changes than in the model membrane (25), and such motions are likely required for His37 protonation. Moreover, the anionic DMPG lipids used in the previous study may increase the local concentration of protons on the membrane surface, thus increasing the apparent pK_a's.

To relate the viral-membrane pK_a's with electrophysiological data, we plotted the total fractions of +2 to +4 channels and +3 and +4 channels as a function of pH, which amounted to assuming equal currents for these charged states while the other states do not contribute currents. Comparing these curves with the normalized proton currents of the Udorn strain of M2 from pH 8.2 to 4.5 (red solid line) (7, 8), we find that the functional curve falls between the two charged-state distribution curves, suggesting that the +2 to +3 transition activates the channel, consistent with the previous report (20). Fitting these data to the Hill equation yielded a pK_a of 6.8 for the +2 to +4 channels and 5.0 for the +3 and +4 channels, compared to the functional pK_a of 5.8 (Figure 4.4c). To estimate the relative conductivities of the different charged channels, we fit the proton current data by weighting the pK_a-derived populations of the various charged states by the associated current of each state (Supporting Information). Figure 4.4d shows the best fit (black solid line), obtained using weighting factors of 0.33±0.05, 1.6±0.2 and 0.3±0.5 for the +2, +3 and +4 channels, respectively, and 0 for the neutral and +1 channels. The large uncertainty of the +4 conductivity is due to the lack of current data below pH 4.5 (7). When an alternative set of functional data from pH 7.5 to pH 4 was used (29), we obtained similar relative currents for the +2 and +3 states (0.47±0.07 and 1.41±0.24) while the +4 current increased to 0.70±0.25, as expected when the current plateaus at lower pH (Figure 4.S5). Taken together, these data indicate that the +3 channel has the highest conductivity, which is 3-5 fold larger than that of the +2 channel. This finding provides a quantitative basis for the conclusion that the third protonation event activates the channel (20).

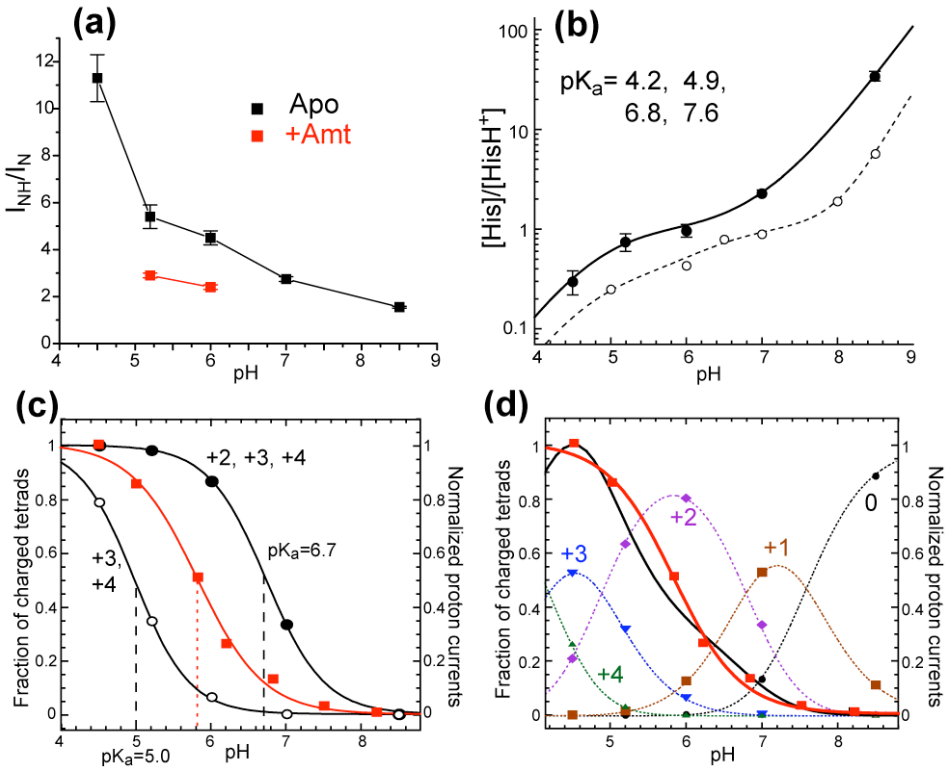

Figure 4.4. pK_a analysis of the His37 tetrad in the viral membrane. (a) I_{NH}/I_N ratios without drug (black) and with drug bound (red), obtained from integrated ^{15}N intensities at 243 K. (b) $[His]/[HisH^+]$ ratios (filled symbols) as a function of pH and the best-fit curve with pK_a's of 4.2, 4.9, 6.8, and 7.6. The $[His]/[HisH^+]$ ratios reported for DMPC/DMPG-bound M2TM (open circles) are shown for comparison (20), where the best fit (dashed line) gave pK_a's of < 5, 6.3, 8.2 and 8.2. (c) Fraction of charged states as a function of pH based on the measured pK_a's. Filled circles: sum of +2, +3 and +4 channels. Open circles: sum of +3 and +4 channels. Best-fit curves (Supporting Information) gave pK_a's of 6.7 and 5.0. The normalized proton currents as a function of pH (red symbols) (7) are shown for comparison, with a best-fit pK_a of 5.8. (d) Fraction of all five charged states as a function of pH (symbols and dotted lines), compared to the proton current (red squares and red solid line). Best-fit of the functional data is shown as a black solid line, with relative currents of 0.33 : 1.6 : 0.3 for the +2, +3 and +4 channels and zero for neutral and +1 channels.

pH-dependent backbone conformational changes

2D ^{13}C-^{13}C and ^{15}N-^{13}C correlation spectra (Figure 4.2) not only gave information on the His37 sidechain structure but also showed systematic backbone conformation changes as a function of pH. The His37 Cα chemical shift increased while the Cβ chemical shift decreased with lowering pH, indicating that His37 backbone becomes more ideally helical at low pH. This trend is consistent with chemical-shift derived (ϕ, ψ) torsion angles (30). The chemical shift change is not continuous but discrete between two states, with the population of the more helical conformation increasing with decreasing pH. The low-pH peaks are broader than the peaks of the less-ideal helix at higher pH. The ^{15}N homogeneous linewidth is also larger for the more helical backbone (Table 4.S1). Thus, the ideal helical conformation at low pH undergoes small-amplitude fluctuations on the microsecond to millisecond timescale around the averaged structure. When both the ideal and distorted helices coexist at pH 5.2, no exchange between them is observed, since both signals are present at their limiting chemical shifts from 273 K (Figure 4.2b) to 308 K (Figure 4.S6). Given the ^{13}C chemical shift differences of ~3 ppm (300 Hz), any exchange between the two conformations must be slower than 300 s^{-1} in the viral membrane. Thus, two types of channels exist at physiological pH, whose backbone conformations are distinguished by the helix ideality at His37 and Gly34 (30). The conducting channels have relatively ideal helical conformations at both sites, indicating straight helices, whereas the non-conducting channels have helical kinks at Gly34 (31) and His37. The former is consistent with the splayed-open C-terminal conformation in the low-pH crystal structure (11), suggesting that this structure is largely the result of charge repulsion of cationic histidines rather than detergent artifact (32). The latter is consistent with the bent M2 conformation at high pH observed by NMR (10, 16, 31). The pH-induced dual conformations at mildly acidic pH support one aspect of the transporter model, but with the difference that no large-scale exchange between the two structures occurs on the sub-10 ms timescale in the virus-mimetic membrane. Instead, the conducting channel undergoes small-amplitude fluctuations around a single ideal helical conformation.

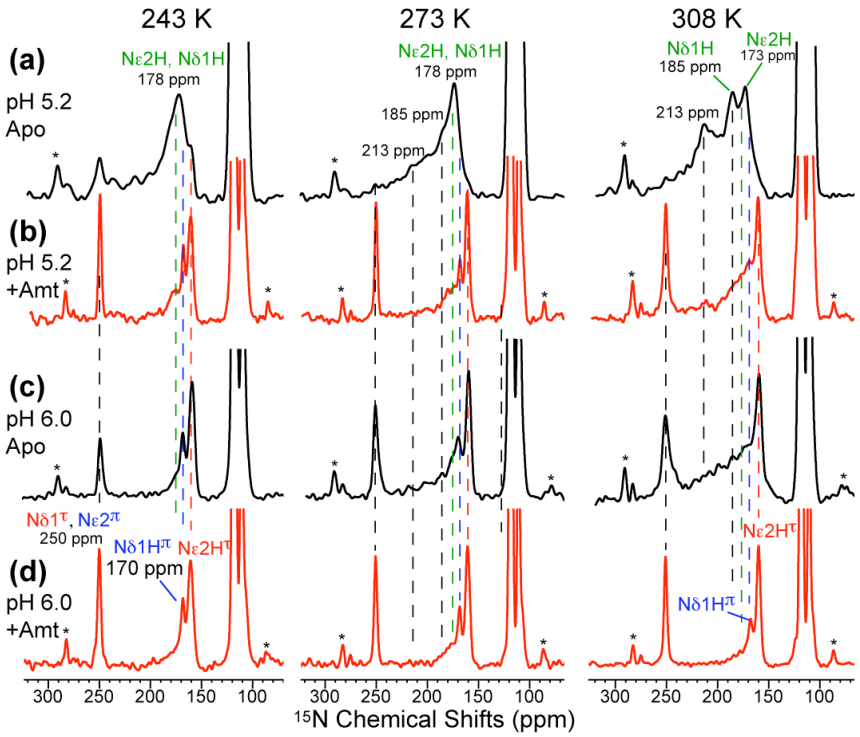

Figure 4.5. ^{15}N CP-MAS spectra of His37 in apo (a, c) and Amt-bound (b, d) M2TM. (a, b) pH 5.2. (c, d) pH 6.0. Spectra were measured at 243 K, 273K and 308 K. Amt binding increased the unprotonated ^{15}N intensity and weakened exchange intensities at 308 K.

Effects of Amt binding on imidazole proton exchange and motion

If imidazole-water proton transfer is essential for proton conduction, then Amt binding should suppress N–NH exchange and reestablish the intensities of the unprotonated and protonated peaks. Indeed, ^{15}N spectra of Amt-bound M2TM at pH 6.0 and pH 5.2 (Figure 4.5) show that Amt significantly increased the 250-ppm peak, suppressed the 213-ppm exchange peak, and reduced the intensity of the 190-220 ppm peak. The drug-bound pH 5.2 spectra resemble the drug-free spectra at higher pH (Figure 4.1, 4.S7). These data indicate that Amt binding, which occurs at Ser31 away from His37 (10), inhibits Nδ1 protonation by dehydrating the N-terminus pore (33) and preventing water access (Figure 4.3a). In comparison, the effect of Amt on the Nε2H–Nε2 exchange is weaker, since the 190-220 ppm intensity is partially retained (Figure 4.5b). The retention of Nε2 exchange is consistent with the presence of water molecules C-terminal to His37 in an intermediate charged channel.

When Nε2 adopts the unprotonated form, Nδ1 must exist in the protonated state, giving a transient π tautomer. Indeed, the 170-ppm π tautomer peak is stronger in the Amt-bound spectra than in the apo spectra (Figure 4.5c, d). The higher 250-ppm peak intensity, which reflects a pK_a drop (Figure 4.4a), is consistent with previous results of DMPC/DMPG-bound M2TM (34). In addition to His37, Amt binding at pH 5.2 also perturbed Gly34 conformation by shifting its equilibrium to a less helical state, indicating that the drug-complexed peptide at low pH adopts a conformation similar to the kinked helix at high pH (30).

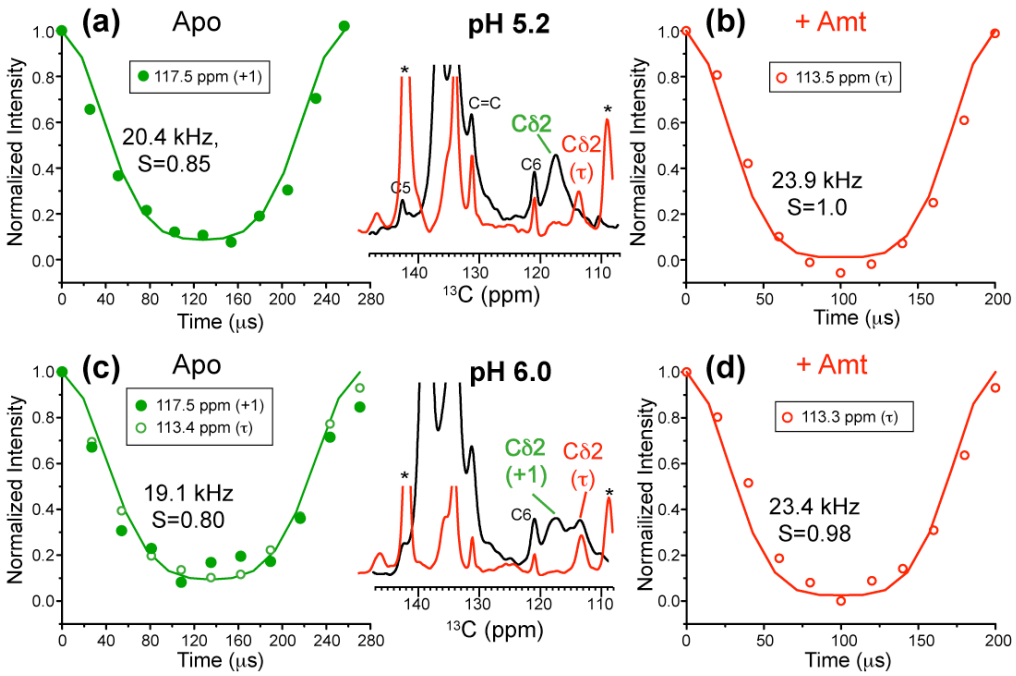

Figure 4.6. His37 sidechain dynamics at 308 K from Cδ2-H dipolar couplings. (a) Apo peptide at pH 5.2. (b) Amt-bound peptide at pH 5.2. (c) Apo peptide at pH 6. (d) Amt-bound peptide at pH 6. The spectra were measured under 3.9 and 3.7 kHz MAS with MREV-8 decoupling for (a, c) and under 5 kHz MAS using FSLG decoupling for (b, d). Drug binding at these acidic pH immobilized the His37 sidechain.

In the low-pH apo channel, His37 sidechains undergo fast reorientations (21) that were proposed to orient the imidazole nitrogens to water molecules for proton transfer. To test this model, we measured imidazole dynamics in the presence of Amt at pH 5.2 and 6.0. If imidazole motion is essential for proton transport, then the Amt-complexed channel should

exhibit no motion. Indeed, the Cδ2-H dipolar coupling reached rigid limit at pH 6 and 5.2 at 308 K in the Amt-bound samples (Figure 4.6b, d), in contrast to the apo samples at the same pH (Figure 4.6a, c). Thus, ring motion is necessary for the conducting channel at acidic pH.

Discussion

The ^{15}N NMR data shown here for M2TM at physiological temperature, pH and membrane composition provide rich insights into the nature of proton exchange of the pH-activating His37. Both Nδ1 and Nε2 are found to undergo protonation and deprotonation at mildly acidic pH at about 3000 times per second (Figure 4.1), in excellent agreement with the proton conductivity of the channel (5, 6). The Nδ1-Nδ1H exchange has equal populations between the protonated and unprotonated states, giving an averaged chemical shift of 213 ppm, while the Nε2H-Nε2 equilibrium is moderately shifted to the protonated state, consistent with the higher proton affinity of Nε2. These NH-N exchange events require H-bonding with water, since Amt binding in the N-terminal pore, which is known to dehydrate the channel (33), completely suppressed the 213-ppm exchange peak (Figure 4.5b). In comparison, Nε2 deprotonation and protonation are partly retained in the presence of drug, consistent with the availability of water C-terminal to His37 (21). The water-imidazole proton transfer is in excellent agreement with the observed water clusters above and below the His37 tetrad in the pH 6.5 crystal structure (14), and supports the proposal of proton delocalization to reduce electrostatic repulsion in the multiply charged channel. The ~3000 s^{-1} proton transfer is accompanied by ring reorientations at ~50,000 s^{-1}, which is reasonable because only a fraction of imidazole orientations can be well aligned to transfer protons to and from water.

The μs-ms timescale of proton transfer, the strong temperature dependence of the ^{15}N spectra (Figure 4.1), and the lack of neutral-cationic His cross peaks in the 2D spectra (Figure 4.2d), rule out the existence of a strong H-bond between neutral and charged histidines at mildly acidic pH (16). The His dimer model (16) also requires the His37 χ_2 torsion angle to be 90°, which contradicts the measured value of 180° in the bilayer (21) and in the crystal (14, 35). The trans χ_2 angle points the unprotonated Nδ1 towards the N-terminus rather than to another His, further supporting H-bonding with water (14).

The four pK_a's obtained for the viral-membrane-bound M2TM quantified the populations of the four charged states at each pH. Based on these populations and the reported proton currents (7, 8), we estimated the relative conductivities of the differently charged channels (Figure 4.4d). The +3 channel has the highest conductivity and is thus chiefly responsible for the proton-channel activity. Although the +2 channel has lower specific activity, its population is the largest over the physiological pH range (Figure 4.4d), suggesting that the +2 state may be important for storing protons before full channel activation (14). The +4 channel conducts fewer protons than the +3 channel, as expected due to the severe charge repulsion between the +4 tetrad and the proton. This pK_a-based extraction of relative conductivities assumes a constant membrane potential and a constant pH_{in}, (8). Some differences may also arise from the fact that the NMR pK_a values were measured under equilibrium conditions whereas actual proton conduction may occur at non-equilibrium conditions. Despite these approximations, the qualitative trend of the relative activities of the different charged states is robust, consistently indicating the +3 channel to be the most conducting state (22).

In the cholesterol-rich virus-mimetic membrane, we did not detect large backbone conformational changes on timescales shorter than 10 ms at low pH (Figure 4.2). However, we do not rule out the possibility of such motion in more fluid lipid membranes. The membrane mixture used in the current study contains 30 mol% cholesterol, which mimics the average composition of the virus envelope but not necessarily the immediate lipid environment of M2 in real viruses. M2 is known to partition into the periphery of the raft and non-raft domains of the virus envelope (3, 36), thus the exact microenvironment of the M2 protein in vivo may be less ordered than the membrane mixture used here, making large-scale conformational fluctuations still possible. Regardless of the presence or absence of such large-scale motions, the broadened ^{15}N linewidths at low pH in both virus-mimetic and model membranes (30, 37) indicate that small-amplitude conformational fluctuations exist on the microsecond timescale and are likely relevant for proton transport.

In summary, these ^{15}N solid-state NMR data allow direct "visualization" of proton transfer between His and water on the functional timescale at physiologically relevant pH. The ^{15}N lineshapes and their changes by drug binding provide definitive evidence for the

shuttle mechanism of proton transport, where ring reorientation facilitates imidazole-water proton transfer. In the conducting state, the protein backbone undergoes local conformational fluctuations around an ideal helical structure with a large water-accessible surface (33), which enable the delivery of water molecules to His37 from both sides. This study underscores the power of solid-state NMR for revealing atomic details of proton transport across biological membranes.

Methods

Membrane samples and solid-state NMR spectroscopy

M2TM (residues 22-46) of the Udorn strain of the influenza A virus was synthesized and uniformly ^{13}C, ^{15}N-labeled at Gly34, His37 and Ile39 or Ile42. The peptide was reconstituted by detergent dialysis into a virus-envelope-mimetic lipid membrane that includes sphingomyelin and cholesterol in addition to phospholipids (25). This membrane mixture enhances the NMR spectral resolution and immobilizes the rotational diffusion of the M2TM helical bundle, thus enabling detection of sidechain motions (25, 38, 39). The protein : lipid molar ratio was 1 : 15. Membrane samples were prepared at five pH values: pH 8.5, 7.0, 6.0, 5.2 and 4.5. Two Amt-bound M2TM samples were prepared at pH 6.0 and pH 5.2 by directly titrating Amt-containing buffer into the NMR rotor to reach a final drug : tetramer ratio of 4 : 1.

Solid-state NMR experiments were carried out at ^{1}H Larmor frequencies of 400 MHz and 600 MHz (Bruker) using triple-resonance 4 mm MAS probes. Additional details are given in the Supporting Information.

Extraction of proton dissociation constants

The four proton dissociation constants are extracted using a modified approach from that of (20). The equilibrium reactions are (20):

$$\begin{aligned} His_4H_4^{4+} &\overset{K_{a1}}{\Leftrightarrow} His_4H_3^{3+} + H^+, \\ His_4H_3^{3+} &\overset{K_{a2}}{\Leftrightarrow} His_4H_2^{2+} + H^+ \\ His_4H_2^{2+} &\overset{K_{a3}}{\Leftrightarrow} His_4H_1^{+} + H^+ \\ His_4H_1^{+} &\overset{K_{a4}}{\Leftrightarrow} His_4 + H^+ \end{aligned}, \tag{1}$$

where the four acid dissociation constants are defined as:

$$K_{a1} = \frac{\left[His_4H_3^{3+}\right]\left[H^+\right]}{\left[His_4H_4^{4+}\right]},\ K_{a2} = \frac{\left[His_4H_2^{2+}\right]\left[H^+\right]}{\left[His_4H_3^{3+}\right]},\ K_{a3} = \frac{\left[His_4H_1^{+}\right]\left[H^+\right]}{\left[His_4H_2^{2+}\right]},\ K_{a4} = \frac{\left[His_4\right]\left[H^+\right]}{\left[His_4H_1^{+}\right]} \tag{2}$$

The products of these equilibrium constants are:

$$\begin{aligned} K_{a1}K_{a2} &= \frac{\left[His_4H_2^{2+}\right]\left[H^+\right]^2}{\left[His_4H_4^{4+}\right]},\ K_{a1}K_{a2}K_{a3} = \frac{\left[His_4H_1^{+}\right]\left[H^+\right]^3}{\left[His_4H_4^{4+}\right]}, \\ K_{a1}K_{a2}K_{a3}K_{a4} &= \frac{\left[His_4\right]\left[H^+\right]^4}{\left[His_4H_4^{4+}\right]} \end{aligned} \tag{3}$$

By integrating the unprotonated ^{15}N signal at ~250 ppm and the protonated ^{15}N signals at ~170 ppm, we obtain the ratio of neutral to cationic histidines as:

$$\frac{\left[His\right]}{\left[HisH^+\right]} = \frac{I_N \cdot \kappa}{\left(I_{NH} - I_N \cdot \kappa\right)/2} = \frac{2}{\left(I_{NH}/I_N\right)/\kappa - 1} \tag{4}$$

In equation (4) κ is a scaling factor to account for the different CP efficiencies between the unprotonated and protonated nitrogens. This factor was measured to be 1.46 using amino acid histidine (Supporting Information).

Based on equations (1-3), the $\left[His\right]/\left[HisH^+\right]$ ratio depends on pH according to:

$$\frac{[His]}{[HisH^+]} = \frac{1\cdot[His_4H_3^{3+}] + 2\cdot[His_4H_2^{2+}] + 3\cdot[His_4H_1^{+}] + 4\cdot[His_4]}{4\cdot[His_4H_4^{4+}] + 3\cdot[His_4H_3^{3+}] + 2\cdot[His_4H_2^{2+}] + 1\cdot[His_4H_1^{+}]}$$
$$= \frac{1\cdot\frac{K_{a1}}{10^{-pH}} + 2\cdot\frac{K_{a1}\cdot K_{a2}}{10^{-2\,pH}} + 3\cdot\frac{K_{a1}\cdot K_{a2}\cdot K_{a3}}{10^{-3\,pH}} + 4\cdot\frac{K_{a1}\cdot K_{a2}\cdot K_{a3}\cdot K_{a4}}{10^{-4\,pH}}}{4 + 3\cdot\frac{K_{a1}}{10^{-pH}} + 2\cdot\frac{K_{a1}\cdot K_{a2}}{10^{-2\,pH}} + 1\cdot\frac{K_{a1}\cdot K_{a2}\cdot K_{a3}}{10^{-3\,pH}}} \quad (5)$$

Fitting the measured $[His]/[HisH^+]$ as a function of pH using equation (5) yielded the four pK_a's.

Acknowledgements

This work was funded by NSF grant MCB-0543473 and NIH grant GM088204. The authors thank Professor Schmidt-Rohr for stimulating discussions.

References

1. Cady SD, Luo WB, Hu F, & Hong M (2009) Structure and function of the influenza M2 proton channel. *Biochemistry* 48:7356-7364.
2. Pinto LH & Lamb RA (2006) The M2 proton channels of influenza A and B viruses. *J. Biol. Chem.* 281:8997-9000.
3. Rossman JS, Jing X, Leser GP, & Lamb RA (2010) Influenza virus M2 protein mediates ESCRT-independent membrane scission. *Cell* 142:902-913.
4. Schroeder C, Heider H, Möncke-Buchner E, & Lin TI (2005) The influenza virus ion channel and maturation cofactor M2 is a cholesterol-binding protein. *Eur. Biophys. J.* 34:52-66.
5. Lin TI & Schroeder C (2001) Definitive assignment of proton selectivity and attoampere unitary current to the M2 ion channel protein of influenza A virus. *J. Virol.* 75:3647-3656.
6. Mould JA, *et al.* (2000) Mechanism for proton conduction of the M(2) ion channel of influenza A virus. *J. Biol. Chem.* 275:8592-8599.

7. Wang C, Lamb RA, & Pinto LH (1995) Activation of the M2 ion channel of influenza virus: a role for the transmembrane domain histidine residue. *Biophys. J.* 69:1363-1371.
8. Balannik V, *et al.* (2010) Functional studies and modeling of pore-lining residue mutants of the influenza a virus M2 ion channel. *Biochemistry* 49:696-708.
9. Wang C, Takeuchi K, Pinto LH, & Lamb RA (1993) Ion channel activity of influenza A virus M2 protein: characterization of the amantadine block. *J. Virol.* 67:5585-5594.
10. Cady SD, *et al.* (2010) Structure of the amantadine binding site of influenza M2 proton channels in lipid bilayers. *Nature* 463:689-692.
11. Stouffer AL, *et al.* (2008) Structural basis for the function and inhibition of an influenza virus proton channel. *Nature* 451:596-599.
12. Jing X, *et al.* (2008) Functional studies indicate amantadine binds to the pore of the influenza A virus M2 proton-selective ion channel. *Proc. Natl. Acad. Sci. USA* 105:10967-10972.
13. Rosenberg MR & Casarotto MG (2010) Coexistence of two adamantane binding sites in the influenza A M2 ion channel. *Proc. Natl. Acad. Sci. USA* 107:13866-13871.
14. Acharya A, *et al.* (2010) Structural mechanism of proton transport through the influenza A M2 protein. *Proc. Natl. Acad. Sci. USA* 107:15075-15080.
15. Schnell JR & Chou JJ (2008) Structure and mechanism of the M2 proton channel of influenza A virus. *Nature* 451:591-595.
16. Sharma M, *et al.* (2010) Atomistic mechanism of the influenza A proton channel from a structure solved in a lipid bilayer. *Science* 330:509-512.
17. Khurana E, *et al.* (2009) Molecular dynamics calculations suggest a conduction mechanism for the M2 proton channel from influenza A virus. *Proc. Natl. Acad. Sci. USA* 106:1069-1074.
18. Yi M, Cross TA, & Zhou HX (2009) Conformational heterogeneity of the M2 proton channel and a structural model for channel activation. *Proc. Natl. Acad. Sci. USA* 106:13311-13316.
19. Polishchuk AL, *et al.* (2010) A pH-dependent conformational ensemble mediates proton transport through the influenza A/M2 protein. *Biochemistry* 49:10061-10071.

20. Hu J, *et al*. (2006) Histidines, heart of the hydrogen ion channel from influenza A virus: toward an understanding of conductance and proton selectivity. *Proc*. *Natl*. *Acad*. *Sci*. *USA* 103:6865-6870.

21. Hu F, Luo W, & Hong M (2010) Mechanisms of proton conduction and gating by influenza M2 proton channels from solid-state NMR. *Science* 330:505-508.

22. Chen H, Wu Y, & Voth GA (2007) Proton transport behavior through the influenza A M2 channel: insights from molecular simulation. *Biophys*. *J*. 93:3470-3479.

23. Agmon N (1995) The Grotthuss mechanism. *Chem*. *Phys*. *Lett*. 244:456-462.

24. Decoursey TE (2003) Voltage-gated proton channels and other proton transfer pathways. *Physiol*. *Rev*. 83:475-579.

25. Luo W, Cady SD, & Hong M (2009) Immobilization of the influenza A M2 transmembrane peptide in virus-envelope mimetic lipid membranes: a solid-state NMR investigation. *Biochemistry* 48:6361-6368.

26. Song XJ & McDermott AE (2001) Proton transfer dynamics and N-H bond lengthening in N-H...N model systems: a solid-state NMR study *Magn*. *Reson*. *Chem*. 39:S37-S43.

27. Cleland WW & Kreevoy MM (1994) Low-barrier hydrogen bonds and enzymic catalysis. *Science* 264:1887-1890.

28. Wehrle B, Zimmermann H, & Limbach HH (1988) A solid-state 15N CPMAS NMR study of dye tautomerism in glassy polystyrene - site dependence of double minimum potentials and their motional averaging. *J*. *Am*. *Chem*. *Soc*. 110:7014-7024.

29. Chizhmakov IV, *et al*. (1996) Selective proton permeability and pH regulation of the influenza virus M2 channel expressed in mouse erythroleukaemia cells. *J*. *Physiol*. 494:329-336.

30. Hu F, Luo W, Cady SD, & Hong M (2011) Conformational plasticity of the influenza A M2 transmembrane peptide in lipid bilayers under varying pH, drug binding and membrane thickness. *Biochim*. *Biophys*. *Acta* 1808:415-423.

31. Hu J, *et al*. (2007) Backbone structure of the amantadine-blocked trans-membrane domain M2 proton channel from Influenza A virus. *Biophys*. *J*. 92:4335-4343.

32. Cross TA, Sharma M, Yi M, & Zhou HX (2010) Influence of solubilizing environments on membrane protein structures. *Trends Biochem. Sci*. Epub ahead of print.

33. Luo W & Hong M (2010) Conformational changes of an ion channel detected through water-protein interactions using solid-state NMR spectroscopy. *J. Am. Chem. Soc*. 132:2378-2384.

34. Hu J, Riqiang F, & Cross TA (2007) The chemical and dynamical influence of the anti-viral drug amantadine on the M2 proton channel transmembrane domain. *Biophys. J*. 93:276-283.

35. Fiorin G, Carnevale V, & DeGrado WF (2010) Structural biology. The flu's proton escort. *Science* 330:456-458.

36. Leser GP & Lamb RA (2005) Influenza virus assembly and budding in raft-derived microdomains: a quantitative analysis of the surface distribution of HA, NA and M2 proteins. *Virology* 342:215-227.

37. Li C, Qin H, Gao FP, & Cross TA (2007) Solid-state NMR characterization of conformational plasticity within the transmembrane domain of the influenza A M2 proton channel. *Biochim. Biophys. Acta* 1768:3162-3170.

38. Cady SD & Hong M (2008) Amantadine-induced conformational and dynamical changes of the influenza M2 transmembrane proton channel. *Proc. Natl. Acad. Sci. USA* 105:1483-1488.

39. Cady SD & Hong M (2009) Effects of amantadine binding on the dynamics of membrane-bound influenza A M2 transmembrane peptide studied by NMR relaxation. *J. Biomol. NMR* 45:185-196.

Supporting Information

Materials and Methods

Membrane sample preparation

The TM domain of M2 spanning residues 22-46 of the Udorn strain of the influenza A virus (SSDPLVVAASIIGILHLILWILDRL) was synthesized (PrimmBiotech, Cambridge, MA) using Fmoc solid-phase peptide synthesis protocols and purified to >95% purity. The peptide was uniformly ^{13}C, ^{15}N-labeled at Gly34, His37 and Ile39 or Ile42.

A virus-envelope-mimetic membrane mixture containing 1,2-dipalmitoyl-sn-glycero-3-phosphocholine (DPPC), 2-dipalmitoyl-sn-glycero-3-phosphoethanolamine (DPPE), egg sphingomyelin (SPM) and cholesterol (Chol) was prepared at a SPM : DPPC : DPPE : Chol molar ratio of 28:21:21:30 (1). This membrane mixture closely resembles the virus-envelope lipid composition, and enhances the spectral resolution of M2TM compared to peptides incorporated into model phosphocholine membranes. Importantly, the virus-mimetic mixture immobilized the backbone of the M2TM four-helix bundle, thus enabling detection of sidechain motions (1-3). Sphingomyelin was first dissolved in chloroform/methanol (5:1) solution, then mixed with DPPC, DPPE and cholesterol in chloroform. The solution was dried with a stream of nitrogen gas, suspended in cyclohexane and lyophilized. The dry lipid powder was resuspended in 1 mL buffer solution of defined pH, votexed, and freeze-thawed eight times to create uniform lipid vesicles. M2TM powder was codissolved with the detergent octyl-β-D-glucopyranoside (OG) in 1 mL of the same buffer solution at an OG concentration of 20 mg/mL. The pH of the M2TM/OG solution was adjusted with ~100 μL diluted HCl or NaOH solution to the desired pH. The solution was then mixed with 1 mL lipid vesicle solution, votexed for 2 hours and dialyzed with a 3.5-kDa molecular weight cutoff against 1 L buffer at 4°C for 3 days to remove the detergent. The protein-lipid precipitate usually appeared after one day. The proteoliposome solution was centrifuged at 150,000 g and 6°C for 4 hours to yield a membrane pellet with a hydration level of ~40 wt%. The final protein : lipid molar ratio was 1 : 15. The pellet was packed into 4 mm MAS rotors for solid-state NMR experiments.

Membrane samples were prepared at five pH values from 8.5 to 4.5. A pH 8.5 sample was prepared using a Tris buffer (10 mM Tris, 1 mM EDTA, and 0.01 mM NaN_3). A pH 7.0

sample was prepared using a phosphate buffer (10 mM NaH_2PO_4/Na_2HPO_4, 1 mM EDTA, and 0.01 mM NaN_3). A pH 6.0 sample was prepared using a Bis-Tris buffer (10 mM Bis-Tris, 1 mM EDTA, and 0.01 mM NaN_3). A pH 5.2 and a pH 4.5 sample were prepared using a citrate buffer (10 mM citric acid/sodium citrate, 1 mM EDTA, and 0.01 mM NaN_3). We also prepared two Amt-bound M2TM samples at pH 6.0 and pH 5.2, by directly titrating 5-7 μL of Amt-containing solution into the NMR rotor to achieve a final drug : tetramer ratio of 4 : 1.

Solid-state NMR spectroscopy

Solid-state NMR experiments were carried out on a Bruker DSX-400 MHz spectrometer (at 9.4 Tesla) and an AVANCE 600 MHz (at 14.1 Tesla) spectrometer (Karlsruhe, Germany) using 4 mm triple-resonance MAS probes. Typical radiofrequency (rf) pulse lengths were 5 μs for ^{13}C, 6-7 μs for ^{15}N and 3.5-4 μs for ^{1}H. ^{13}C chemical shifts were referenced to the α-Gly CO signal at 176.49 ppm on the TMS scale, and ^{15}N chemical shifts were referenced to the ^{15}N signal of N-acetyl-valine at 122.0 ppm on the liquid ammonia scale.

One-dimensional ^{15}N spectra were measured using standard ^{1}H-^{15}N CP experiments. Unprotonated nitrogens, whose concentrations at different pH values are important for understanding the protonation equilibria of His37, generally have lower CP efficiencies than the protonated nitrogens due to their weak ^{1}H-^{15}N dipolar couplings. To maximize the unprotonated ^{15}N signal, we used a relatively long CP contact time of 3 ms and optimized the Hartman-Hahn condition by using the model compound N-t-Boc-proline, which contains an unprotonated ^{15}N. While the optimal CP contact time for maximizing the unprotonated ^{15}N signal is likely longer than 3 ms, longer contact times will reduce the protonated ^{15}N intensity due to ^{1}H $T_{1\rho}$ relaxation. Thus, 3 ms is a reasonable compromise. For the pK_a analysis, where quantitative intensity ratios of NH and N peaks were required, we used neutral histidine as the model compound to calibrate the scaling factor κ (equation 4) between the NH and N intensities.

Two-dimensional (2D) ^{1}H-driven ^{13}C spin diffusion experiments with 40-60 ms DARR (4) mixing periods were conducted at 273 K under 7-10 kHz MAS. 2D ^{15}N-^{13}C

correlation spectra were measured using a REDOR-based pulse sequence for ^{13}C-^{15}N coherence transfer. The experiments were conducted at 273 K or 243 K under 7-10 kHz MAS. A typical ^{13}C-^{15}N recoupling time of 0.6 ms was used to obtain one-bond ^{15}N-^{13}C cross peaks. ^{15}N T_2 relaxation times were measured at 308 K under 7 kHz MAS using a Hahn-echo sequence with a 12 μs 180° pulse. The ^{1}H decoupling field strength was fixed at 62.5 kHz during the echo delays for all samples to ensure that the motion is probed on the same timescale (5). 2D ^{13}C-^{1}H dipolar-chemical-shift (DIPSHIFT) correlation experiments (6) were carried out under 3.7, 3.9 and 5 kHz MAS at 308 K. ^{1}H homonuclear decoupling in the indirect dimension was achieved using the MREV-8 (7) or FSLG sequence (8), during which the ^{1}H pulse length was 4 μs. The t_1 time-domain data were fit to obtain the apparent ^{13}C-^{1}H dipolar couplings, which were then divided by the scaling factor of the homonuclear decoupling sequence (0.47 for MREV-8 and 0.577 for FSLG) to obtain the true couplings.

To measure dipolar order parameters, both the homonuclear decoupling scaling factor and the rigid-limit coupling have uncertainties that can affect the order parameter values. We thus measured the product of these two factors using the crystalline model peptide formyl-Met-Leu-Phe (f-MLF). Using the theoretical scaling factors for MERV-8 and FSLG, we obtained apparent rigid-limit values of 22.7 kHz for the Cα-Hα coupling and high order parameters of 0.95-1.0 for the f-MLF backbone. Thus, we used these scaling factors and rigid-limit couplings to extract the His37 order parameters.

pKa determination

We extracted the four pK_a's of the His37 tetrad using the integrated intensities of protonated and unprotonated ^{15}N peaks in the 243 K ^{15}N spectra. For the unprotonated ^{15}N, the centerband (~250 ppm) and sideband intensities were added. For the protonated ^{15}N, intensities in the 150 - 200 ppm range were integrated. All spectra were measured under the same magnetic field strength (9.4 Tesla) and the MAS spinning rate to ensure comparable experimental efficiencies for the different pH samples. To determine the κ factor in equation 4, which accounts for the different ^{1}H-^{15}N CP efficiencies for unprotonated and protonated nitrogens, we measured the ^{15}N spectrum of neutral histidine using the same conditions as for the membrane samples. With a CP contact time of 3 ms, after maximizing the unprotonated

^{15}N peak, the unprotonated ^{15}N intensity is 1.464 times lower than the protonated peak intensity. Thus, κ = 1.464 was used to multiply the unprotonated ^{15}N intensities of all M2TM spectra to obtain the correct I_{NH}/I_N ratio. Intensity error bars were estimated based on the signal-to-noise ratio of the spectra and propagated to the error bars for the $[His]/[HisH^+]$ ratios.

Correlation to electrophysiological measurements

To fit the pH-dependent fractions of charged tetrads and the proton current (Figure 4.4c), we used the Hill equation $y = a/\left(1+10^{h(x-pK_a)}\right)$, where h is the Hill coefficient, x is pH, and y is the charge fraction or proton current. The total fraction of the +2, +3 and +4 tetrads was best fit to a pK_a of 6.8 and h = 1.1. The total fraction of the +3 and +4 tetrads was fit to a pK_a of 5.0 and h = 1.2. The proton current curve (9) gave a best-fit pK_a of 5.8 and h = 0.98.

The expressions for the percentages p_i of each charged states as a function of pH (Figure 4.4d) were obtained by rearranging equation (2):

$$\begin{aligned} p_{+4} &= [H^+]^4/\Sigma, \\ p_{+3} &= [H^+]^3 K_1/\Sigma, \\ p_{+2} &= [H^+]^2 K_1K_2/\Sigma, \\ p_{+1} &= [H^+]K_1K_2K_3/\Sigma, \\ p_0 &= K_1K_2K_3K_4/\Sigma, \end{aligned} \qquad (1)$$

where $\Sigma = [H^+]^4 + [H^+]^3 K_1 + [H^+]^2 K_1K_2 + [H^+]K_1K_2K_3 + K_1K_2K_3K_4$

The total current is the product of the charged-state population and the current associated with each state,

$$I_{total} = \sum_{i=0}^{+4} p_i I_i \,. \qquad (2)$$

The I_i values were varied to obtain the best fit to the measured proton currents (9, 10) for wild-type M2.

Table 4.S1. M2TM ^{15}N T_2 (ms) and intrinsic linewidths (Hz) at 308 K as a function of pH.

^{15}N sites	δ_N (ppm)	^{15}N T_2 (ms) $\Delta\nu_{1/2}$ (Hz)			
		pH 8.5	pH 6	pH 5.2	pH 4.5
Gly34 Nα	110, 107	8.0 ms 40 Hz	6.8 ms 47 Hz	6.9 ms 46 Hz	7.0 ms 45 Hz
His37 and Ile39/42 Nα	118	12 ms 27 Hz	9.5 ms 34 Hz	9.3 ms 34 Hz	7.6 ms 42 Hz
Nε2	159, 173	1.2 ms 265 Hz	1.3 ms 250 Hz	2.2 ms 145 Hz	2.1 ms 152 Hz
Nδ1	250, 185	1.8 ms 177 Hz	1.1 ms 290 Hz	2.2 ms 145 Hz	2.1 ms 152 Hz
Exchange peak	213	-	0.75 ms 420 Hz	2.8 ms 114 Hz	-
Broad peak	190-220	-	0.8 ms 400 Hz	1.7 ms 187 Hz	-

Table 4.S2. ^{15}N intensities and the neutral to charged histidine ratios as a function of pH.

pH	I_{NH}/I_N	Error bar	$[His]/[HisH^+]$	Error bar
4.5	11.3	1.0	0.30	0.08
5.2	5.4	0.5	0.74	0.15
6.0	4.5	0.3	0.96	0.14
7.0	2.75	0.1	2.28	0.17
8.5	1.55	0.04	34.1	3.8

Table 4.S3. His37 pK_a's and the associated uncertainties in the virus-mimetic lipid membrane.

pK_a	Uncertainty
4.2	0.6
4.9	0.3
6.8	0.1
7.59	0.01

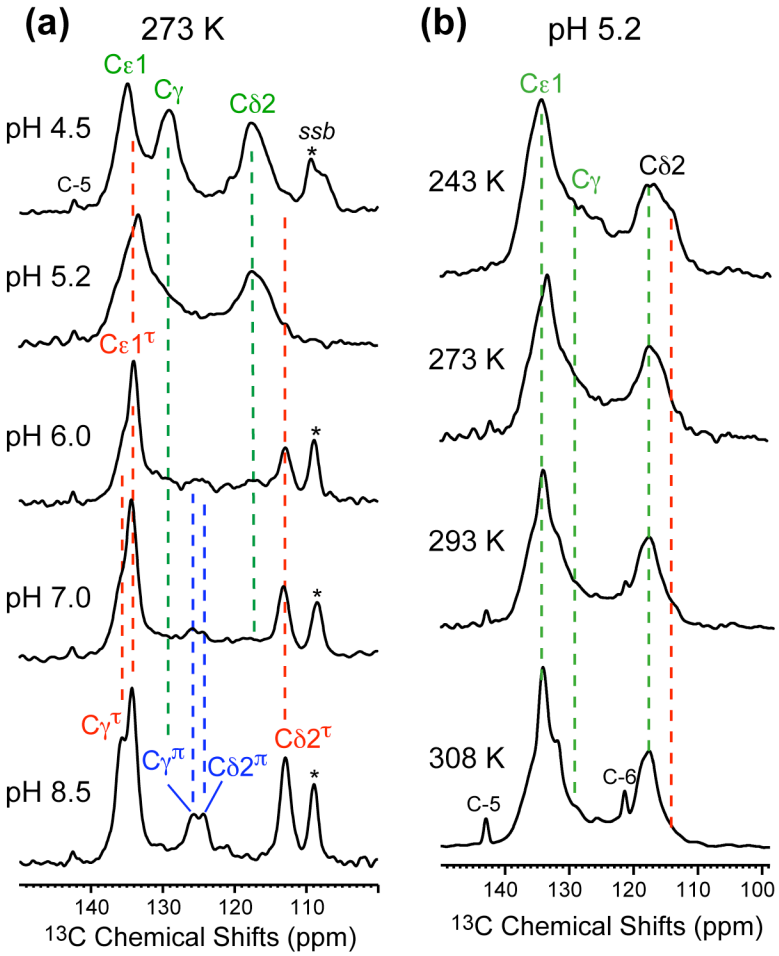

Figure 4.S1. ^{13}C CP-MAS spectra of His37-labeled M2TM. (a) Spectra as a function of pH at 273 K. (b) Spectra of the pH 5.2 sample as a function of temperature. Asterisks denote spinning sidebands. The sidechain Cδ2 and Cγ peaks are good indicators of the histidine charged state. The Cδ2 peak shifts downfield from 113.1 to 117.6 ppm upon Nδ1 protonation, while the Cγ peak shifts upfield from 135.5 to 128.8 ppm. As the pH decreases, the cationic Cδ2 and Cγ intensities increase while the neutral Cδ2 intensity decreases.

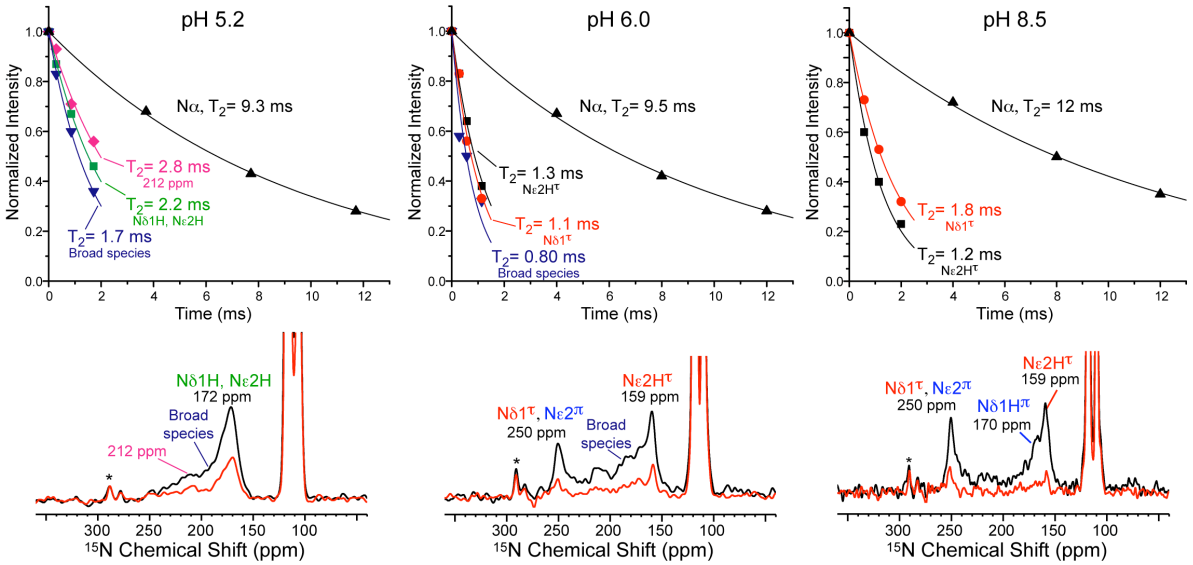

Figure 4.S2. ^{15}N T_2 relaxation times of M2TM at 308 K as a function of pH. (a) pH 5.2. (b) pH 6.0. (c) pH 8.5. The data were obtained using a Hahn-echo experiment at a ^{1}H decoupling field of 62.5 kHz. The broad peak between 190 and 220 ppm has moderately shorter T_2 than the other sidechain signals, while the backbone amides have much longer T_2's than the sidechain nitrogens.

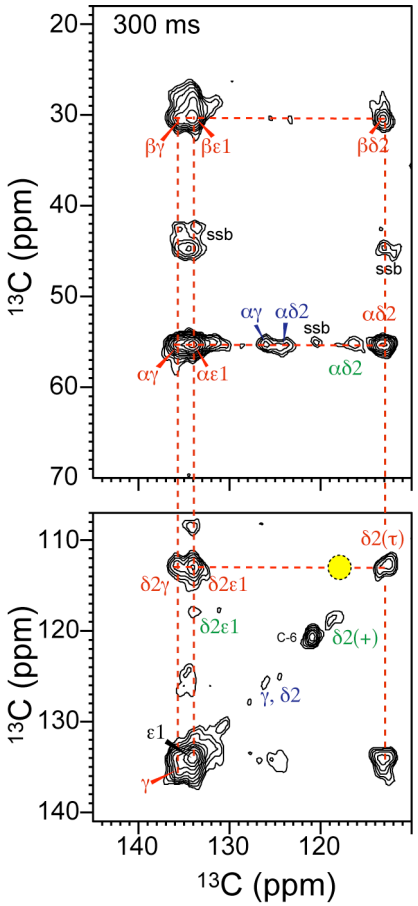

Figure 4.S3. Aromatic region of the 2D ^{13}C-^{13}C correlation spectrum of M2TM at pH 6 with a 300 ms mixing time at 273 K. No neutral-cationic Cδ2(τ) – Cδ2(+) cross peak was observed (yellow shade), even though both species exist at this pH. Thus, the data rule out the existence of H-bonded imidazole-imidazolium dimers.

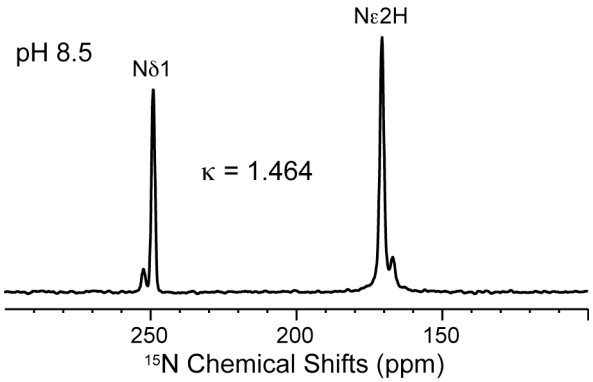

Figure 4.S4. ^{15}N CP-MAS spectrum of U-^{13}C, ^{15}N labeled neutral histidine (pH 8.5) to determine the CP scaling factor κ between unprotonated and protonated ^{15}N. The ^{1}H-^{15}N CP contact time was 3 ms and the CP conditions were optimized in the same way as for membrane-bound M2TM. The integrated intensity of the unprotonated Nδ1 is 1.464 less than the Nε2H intensity, even though the two nitrogens are equimolar. This scaling factor was applied in calculating the neutral to cationic histidine ratio in M2TM.

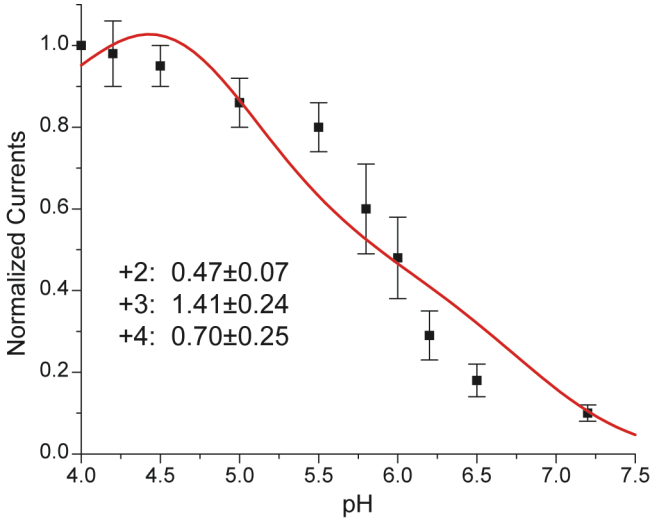

Figure 4.S5. Best-fit of the proton currents reported by Chizhmakov et al (11) using the four His37 pK_a's determined in the virus-mimetic membrane. The current was measured on the Weybridge strain of M2 at a membrane potential of -60 mV. For comparison, the data in (9) (Figure 4.4d) was measured on the Udorn strain of M2 at a membrane potential of -120 mV. The relative currents for the +2, +3 and +4 channels are 0.47±0.07, 1.41±0.24, and 0.70±0.25. Thus, the availability of proton current data down to pH 4 resulted in a higher +4 channel conductivity, which is, however, still smaller than the conductivity of the +3 channel.

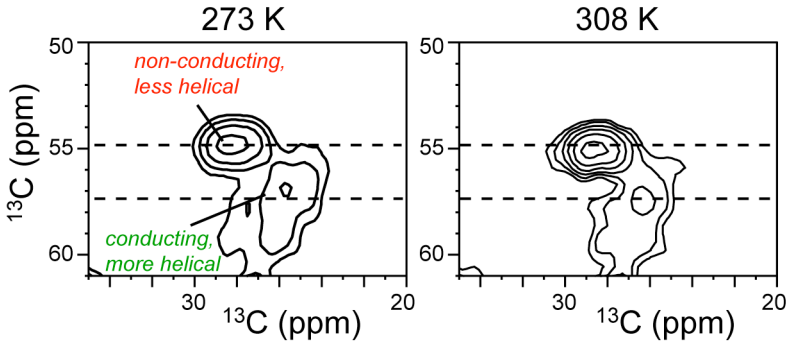

Figure 4.S6. His37 backbone region of the 2D ^{13}C-^{13}C correlation spectrum of the pH 5.2 sample at 273 K and 308 K. No chemical shift averaging is present at high temperature, indicating the lack of exchange between the kinked and straight helical conformations.

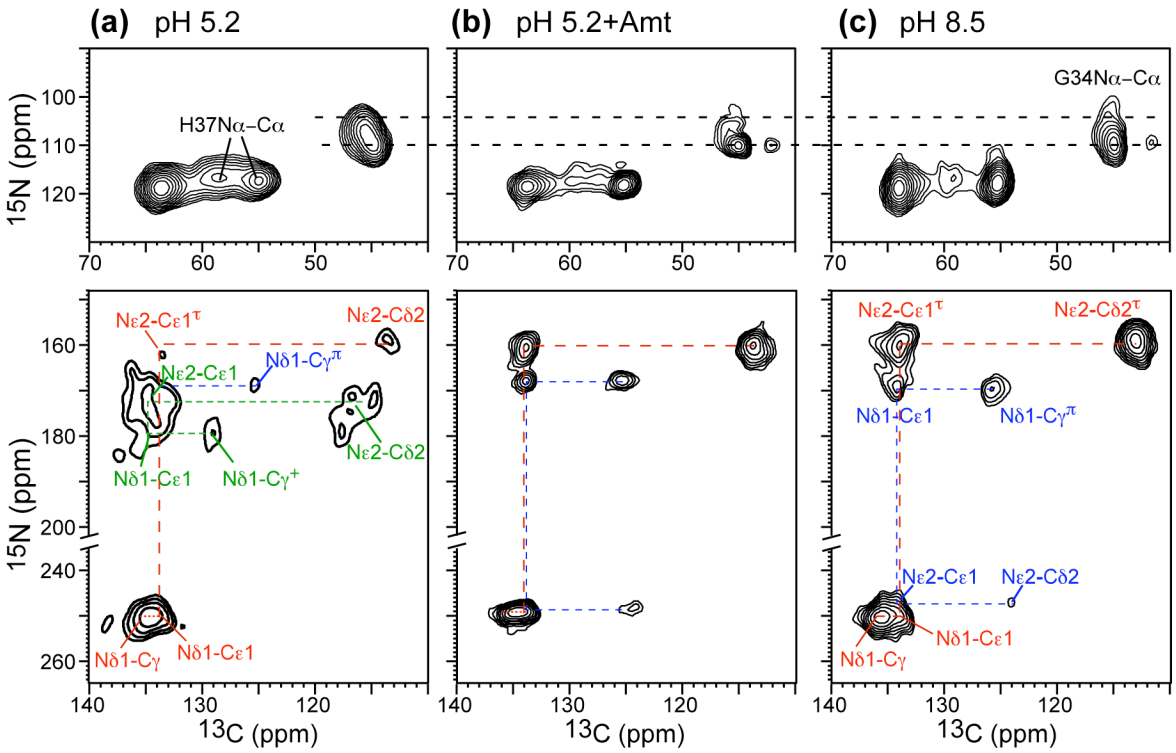

Figure 4.S7. 2D ^{15}N-^{13}C correlation spectra of His37 without and with Amt at 243 K. (a) pH 5.2 without Amt. (b) pH 5.2 with bound Amt. (b) pH 8.5 without Amt. Top row: backbone N-Cα region. Bottom row: imidazole sidechain region.

References

1. Luo W, Cady SD, & Hong M (2009) Immobilization of the influenza A M2 transmembrane peptide in virus-envelope mimetic lipid membranes: a solid-state NMR investigation. *Biochemistry* 48:6361-6368.
2. Cady SD & Hong M (2008) Amantadine-induced conformational and dynamical changes of the influenza M2 transmembrane proton channel. *Proc. Natl. Acad. Sci. USA* 105:1483-1488.
3. Cady SD & Hong M (2009) Effects of amantadine binding on the dynamics of membrane-bound influenza A M2 transmembrane peptide studied by NMR relaxation. *J. Biomol. NMR* 45:185-196.
4. Takegoshi K, Nakamura S, & Terao T (2001) C-13-H-1 dipolar-assisted rotational resonance in magic-angle spinning NMR. *Chem. Phys. Lett.* 344:631-637.
5. Rothwell WP & Waugh JS (1981) Tranverse relaxation of dipolar coupled spin systems under rf irradiation: detecting motions in solids. *J. Chem. Phys.* 74:2721-2732.
6. Munowitz MG, Griffin RG, Bodenhausen G, & Huang TH (1981) Two-dimensional rotational spin-echo NMR in solids: correlation of chemical shift and dipolar interactions. *J. Am. Chem. Soc.* 103:2529-2533.
7. Rhim W-K, Elleman DD, & Vaughan RW (1973) Analysis of multiple-pulse NMR in solids. *J. Chem. Phys.* 59:3740-3749.
8. Bielecki A, Kolbert AC, & Levitt MH (1989) Frequency-switched pulse sequences: homonuclear decoupling and dilute spin NMR in solids. *Chem. Phys. Lett.* 155:341-346.
9. Wang C, Lamb RA, & Pinto LH (1995) Activation of the M2 ion channel of influenza virus: a role for the transmembrane domain histidine residue. *Biophys. J.* 69:1363-1371.
10. Balannik V, *et al.* (2010) Functional studies and modeling of pore-lining residue mutants of the influenza a virus M2 ion channel. *Biochemistry* 49:696-708.

11. Chizhmakov IV, *et al*. (1996) Selective proton permeability and pH regulation of the influenza virus M2 channel expressed in mouse erythroleukaemia cells. *J. Physiol*. 494:329-336.

Appendix

Sample Preparation

Fmoc-protection of Amino Acids

The following synthesis procedure is summarized based on literature (*1*) and previous experience in our lab (*2*).

In a 250 ml flask, 2 mmol amino acid is dissolved in 30 ml water. Sodium bicarbonate (2 e.q.) is then added and dissolved with magnetic stirring. The solution is cooled to 5 °C. 1.1 e.q. Fmoc-OSu dissolved in 30 ml dioxane (also cooled to 5 °C) is added drop-wise. The mixture is kept stirring for 1 hour in the water-ice bath (0 °C). The bath is then removed and the solution is allowed to warm up to room temperature and reacts overnight while stirring. Water is then added to double the volume of the solution and the residual Fmoc-OSu is extracted with ethyl acetate for 2 times (2 × 40 ml). The organic layer is back extracted twice with saturated sodium bicarbonate solution (2 × 30 ml). The aqueous layers are combined and 0.2 M HCl solution is added to pH≈2 as tested by the pH paper. White precipitates (Fmoc-amino acid product) appear immediately. The solution is then extracted with ethyl acetate for three times (3 × 50 ml). The organic layers (~150 ml) are combined and dried with anhydrous sodium sulfate. The solution is filtered and the ethyl acetate solvent is removed using rotor evaporation. The product is lyophilized overnight to remove any residual solvents. The final product is white or slightly yellow powder. The purity is checked with ^{1}H solution NMR (dissolved in d6-DMSO or $CDCl_3$). Fmoc-amino acids (Gly, Ala, Val, Ile, Leu and Trp) have been synthesized with the yield and purity to be about 90%.

Peptide and Lipids

The influenza AM2 TM (22-46) peptide (SSDPLVVAASIIGILHLILWILDRL) is synthesized using standard Fmoc solid-phase peptide synthesis protocol and is purified to >95% purity by PrimmBiotech (Cambridge, MA). All lipids and cholesterol, including 1,2-dipalmitoyl-sn-glycero-3-phosphocholine (DPPC), 2-dipalmitoyl-sn-glycero-3-phosphoethanolamine (DPPE), egg sphingomyelin (SPM) and cholesterol (Chol) are purchased from Avanti Polar Lipids (Alabaster, AL).

Proteoliposome Sample Preparation

The following protocol is adapted from procedures described by our group (*3, 4*). Virus-envelope-mimetic membrane is used for studies in this thesis.

DPPC and Chol are dissolved in the chloroform and SPM is dissolved in the chloroform/methanol (5:1) solution. They are mixed with DPPE at a molar ratio SPM:DPPC:DPPE:Chol = 28:21:21:30. The mixture is dried under nitrogen gas and lyophilized in cyclohexane overnight. The dry lipid powder is then suspended in 1 mL 10 mM buffer solution of defined pH (including 1 mM EDTA and 0.01 mM NaN_3), vortexed for 30 minutes, and free-thawed eight times with liquid N_2 to create uniform vesicles. M2TM peptide is dissolved with ~20 mg octyl-β-D-glucopyranoside (OG) in 1 mL of the same buffer. The 1 mL lipid vesicle solution is added into the clear M2TM/OG solution at a protein:lipid molar ratio 1:15. The mixture is shaken for 2 hours at room temperature and transferred into a dialysis bag with a 3.5-kDa molecular weight cutoff. The total solution volume is around 3 ml at this time. The mixture is then dialyzed against 1 L buffer of the same pH at 4°C for 3 days. The buffer is changed every 8-12 hours to remove the detergent and to facilitate the reconstitution of peptide into the liposome. After the 3-day dialysis, the proteoliposome mixture is transferred to a 4 ml ultracentrifuge tube and spun down at 55,000 rpm and 6 °C for 4 hours. The supernatant is separated from the pellet at the bottom and stored in a glass vial for pH and UV-Vis absorbance check. The pellet is weighed and lyophilized to achieve a ~40% hydration level. The final pellet was packed using a spatula into 4 mm MAS rotors for solid-state NMR experiments.

References

(1) Myers, A. G., Gleason, J. L., Yoon, T., and Kung, D. W. (1997) Highly practical methodology for the synthesis of D- and L-α-amino acids, N-protected α-amino acids, and N-methyl-α-amino acids. *J. Am. Chem. Soc. 119*, 656-673.

(2) Tang, M. (2008) Ph.D. thesis in *Chemistry* pp 169, Iowa State University, Ames.

(3) Luo, W., Cady, S. D., and Hong, M. (2009) Immobilization of the influenza A M2 transmembrane peptide in virus-envelope mimetic lipid membranes: a solid-state NMR investigation. *Biochemistry 48*, 6361-6368.

(4) Cady, S. D., and Hong, M. (2008) Amantadine-induced conformational and dynamical changes of the influenza M2 transmembrane proton channel. *Proc. Natl. Acad. Sci. USA 105*, 1483-1488.